UNIVERSIDADE FEDERAL DE PERNAMBUCO
CENTRO DE CIÊNCIAS EXATAS E DA NATUREZA
PROGRAMA DE PÓS-GRADUAÇÃO EM ESTATÍSTICA

ROSA JANETH ALPALA

ENTROPY-BASED TEST STATISTICS FOR HETEROGENEITY DETECTION IN SAR DATA

Recife

2025

ROSA JANETH ALPALA

ENTROPY-BASED TEST STATISTICS FOR HETEROGENEITY DETECTION IN SAR DATA

Tese apresentada ao Programa de Pós-Graduação em Estatística do Centro de Ciências Exatas e da Natureza da Universidade Federal de Pernambuco, como requisito parcial à obtenção do título de Doutora em Estatística.

Área de Concentração: Estatística Aplicada

Orientador: Dr. Alejandro César Frery Orgambide
Co-Orientador: Dr. Abraão David Costa do Nascimento

Recife
2025

.Catalogação de Publicação na Fonte. UFPE - Biblioteca Central

Alpala, Rosa Janeth.
   Entropy-based test statistics for heterogeneity detection in SAR data / Rosa Janeth Alpala. - Recife, 2025.
   89f.: il.

   Tese (Doutorado)- Universidade Federal de Pernambuco, Centro de Ciências Exatas e da Natureza, Programa de Pós-Graduação em Estatística, 2025.
   Orientação: Alejandro César Frery Orgambide.
   Coorientação: Abraão David Costa do Nascimento.

   1. Entropia; 2. Heterogeneidade; 3. Distribuição gama; 4. Teste de hipótese. I. Orgambide, Alejandro César Frery. II. Nascimento, Abraão David Costa do. III. Título.

UFPE-Biblioteca Central

ROSA JANETH ALPALA

ENTROPY-BASED TEST STATISTICS FOR HETEROGENEITY DETECTION IN SAR DATA

Tese apresentada ao Programa de Pós-Graduação em Estatística da Universidade Federal de Pernambuco, como requisito parcial para a obtenção do título de Doutora em Estatística.

Aprovada em: 28 de julho de 2025.

BANCA EXAMINADORA

Prof. Dr. Alejandro Cesar Frery Orgambide
Presidente (Orientador), Victoria University of Wellington

Prof. Dr. Saeid Homayouni
Examinador Externo, Institut National de la Recherche Scientifique, Centre Eau Terre Environnement

Prof. Dr. Paolo Ettore Gamba
Examinador Externo, Univesrità degli Studi di Pavia

Profa. Dra. Fátima Nelsizeuma Sombra de Medeiros
Examinadora Externo, UFC

Prof. Dr. Anderson Adaime de Borba
Examinador Externo, Universidade Presbiteriana Mackenzie

ACKNOWLEDGEMENTS

Firstly, I would like to thank my supervisors, Prof. Alejandro Frery and Prof. Abraão do Nascimento, for their guidance and support throughout these years. Working with you has been an incredibly valuable learning experience. I truly appreciate the attention and dedication you give to your students.

I am also thankful to the Universidade Federal de Pernambuco and the Programa de Pós-Graduação em Estatística for their support during my academic journey. Special thanks to Prof. Pablo Rodriguez for all his help with administrative matters and for his patience.

I acknowledge the financial support from the Coordenação de Aperfeiçoamento de Pessoal de Nível Superior – Brasil (CAPES) – Finance Code 001, the Programa de Doutorado-Sanduíche no Exterior (PDSE), and the Fundação de Amparo à Ciência e Tecnologia do Estado de Pernambuco (FACEPE), which made this work possible.

I would like to express my gratitude to the members of my examination committee, Prof. Saeid Homayouni, Prof. Paolo Gamba, Prof. Anderson de Borba, and Prof. Fátima Sombra, for agreeing to be part of the defense of my thesis and for their valuable comments and suggestions.

This journey would not have been the same without all the amazing people I met in Brazil and New Zealand. To everyone, thank you for your friendship and support, which made this experience unforgettable.

Finally, I am especially grateful to my family, who have always supported and encouraged me along the way.

ABSTRACT

This work presents a statistical approach to detect heterogeneity in synthetic aperture radar (SAR) intensity data using entropy-based methods. In SAR data analysis, an accurate interpretation of the terrain fundamentally depends on the distinction between two main regimes: homogeneous regions, in which speckle is fully developed and SAR returns are represented by the Gamma distribution, and heterogeneous areas, which require more flexible distributions to describe complex scattering, generally represented by the $\mathcal{G}_I^0$ distribution. Although this discrimination is essential for remote sensing applications, classical parametric tests are generally not suitable for this task due to analytical and numerical limitations. To overcome these challenges, we propose three test statistics to detect heterogeneity in SAR images based on Shannon, Rényi, and Tsallis entropies. The associated tests employ nonparametric entropy estimators constructed from sample spacings, avoiding explicit assumptions about the underlying distribution. To increase the accuracy of the tests, especially for small samples, we incorporate a bootstrap-based bias correction procedure that improves the stability of the estimators, reduces bias, and decreases the mean squared error. The proposed tests are evaluated through Monte Carlo simulations, using test size and power under different speckle and texture conditions as performance criteria. The results show that the tests based on Rényi and Tsallis entropies outperform the version based on Shannon entropy, detecting subtler texture variations and maintaining higher reliability in identifying truly homogeneous regions. Finally, the methodology is applied to both simulated and real SAR data. The analysis is performed using sliding windows, generating maps of p-values that allow for visual and quantitative assessment of spatial heterogeneity. The Rényi-based test consistently identifies fine-scale roughness patterns, while the Tsallis-based test performs better in detecting homogeneous regions. Together, these entropy-based tools provide a robust, interpretable, and unsupervised framework for detecting heterogeneity in SAR data.

Keywords: entropy; heterogeneity; gamma distribution; hypothesis testing; bootstrap.

RESUMO

Este trabalho apresenta uma abordagem estatística para detectar heterogeneidade em dados de intensidade de radar de abertura sintética (SAR), utilizando métodos baseados em entropia. Na análise de dados SAR, uma interpretação precisa do terreno depende fundamentalmente da distinção entre dois regimes principais: regiões homogêneas, em que o speckle está totalmente desenvolvido, os retornos SAR são representados pela distribuição Gamma, e áreas heterogêneas requerem distribuições mais flexíveis para descrever o espalhamento complexo, geralmente representado pela distribuição $\mathcal{G}_I^0$. Embora essa discriminação seja essencial para aplicações de sensoriamento remoto, testes paramétricos clássicos geralmente não são adequados para essa tarefa devido a limitações analíticas e numéricas. Para superar esses desafios, propomos três estatísticas de teste para detectar heterogeneidade em imagens SAR, com base nas entropias de Shannon, Rényi e Tsallis. Os testes associados utilizam estimadores não paramétricos de entropia construídos a partir de espaçamentos amostrais, evitando suposições explícitas sobre a distribuição subjacente. Para aumentar a precisão dos testes, especialmente em amostras pequenas, incorporamos um procedimento de correção de viés via bootstrap, que melhora a estabilidade dos estimadores, reduz o viés e o erro quadrático médio. Os testes propostos são avaliados por meio de simulações de Monte Carlo, tendo como critério de avaliação seu tamanho e poder sob diferentes condições de speckle e textura. Os resultados mostram que os testes baseados nas entropias de Rényi e Tsallis superam a versão baseada na entropia de Shannon, detectando variações de textura mais sutis e mantendo maior confiabilidade na identificação de regiões verdadeiramente homogêneas. Por fim, a metodologia é aplicada tanto a dados simulados como a dados SAR reais. A análise é realizada com janelas deslizantes, gerando mapas de valores-p que permitem a avaliação visual e quantitativa da heterogeneidade espacial. O teste baseado na entropia de Rényi mostra desempenho superior na identificação de padrões de rugosidade em pequena escala, enquanto o teste baseado em Tsallis é melhor na detecção de regiões homogêneas. Em conjunto, essas ferramentas baseadas em entropia oferecem uma estrutura robusta, interpretável e não supervisionada para a detecção de heterogeneidade em dados SAR.

Palavras-chave: entropia; heterogeneidade; distribuição gama; teste de hipótese; bootstrap.

LIST OF FIGURES

LIST OF TABLES

LIST OF ABBREVIATIONS

AUC	Area Under the ROC Curve
ASF	Alaska Satellite Facility
CDF	Cumulative distribution function
ENL	Equivalent number of looks
ESA	European Space Agency
PDF	Probability density function
ROI	Region of interest
ROC	Receiver Operating Characteristic
SAR	Synthetic Aperture Radar
SNAP	Sentinel Application Platform
UAVSAR	Uninhabited Aerial Vehicle Synthetic Aperture Radar

LIST OF SYMBOLS

$\mathbb{R}_+$	Positive real numbers
$\Gamma(\cdot)$	Gamma function
$\Gamma_{\mathrm{SAR}}(L, \mu)$	Gamma SAR distribution with parameters L and μ
$\mathcal{G}_I^0$	$\mathcal{G}_I^0$ distribution for intensity
$\psi^{(0)}(\cdot)$	Digamma function
$H(Z)$	Shannon entropy of random variable Z
$R_\lambda(Z)$	Rényi entropy of order λ
$T_\lambda(Z)$	Tsallis entropy of order λ
$\widehat{H}_{\mathsf{AO}}(\boldsymbol{Z})$	Nonparametric Shannon entropy estimator (Al-Omari)
$\widehat{R}_\lambda(\boldsymbol{Z})$	Nonparametric Rényi entropy estimator via sample spacings
$\widehat{T}_\lambda(\boldsymbol{Z})$	Nonparametric Tsallis entropy estimator via sample spacings
$\widetilde{H}_{\mathsf{AO}}(\boldsymbol{Z})$	Bootstrap-corrected Shannon entropy estimator
$\widetilde{R}_\lambda(\boldsymbol{Z})$	Bootstrap-corrected Rényi entropy estimator
$\widetilde{T}_\lambda(\boldsymbol{Z})$	Bootstrap-corrected Tsallis entropy estimator
$S_{\widetilde{H}_{\mathsf{AO}}}(\boldsymbol{Z}; L)$	Test statistic based on Shannon entropy
$S_{\widetilde{R}_\lambda}(\boldsymbol{Z}; L)$	Test statistic based on Rényi entropy
$S_{\widetilde{T}_\lambda}(\boldsymbol{Z}; L)$	Test statistic based on Tsallis entropy
$\widehat{\mu}$	Sample mean of $\boldsymbol{Z}$
$Z_{(i)}$	i-th order statistic in sample $\boldsymbol{Z}$
m	Spacing parameter (window size) used in entropy estimation
c_i	Boundary correction factor in spacing estimators

CONTENTS

1 INTRODUCTION

Synthetic Aperture Radar (SAR) technology has become essential in remote sensing, as it offers high-resolution imaging capabilities independently of sunlight and weather conditions, thus facilitating continuous and reliable Earth observation (MONDINI et al., 2021). SAR images are widely applied in environmental monitoring (AMITRANO et al., 2021), disaster assessment (GE; GOKON; MEGURO, 2020), agriculture (LIU et al., 2019), urban planning (ESCH et al., 2010; RATHA et al., 2020), and maritime surveillance (LOPEZ-LOPEZ et al., 2021; CAO et al., 2024), among other fields (MOREIRA et al., 2013). Despite these advantages, effective exploitation of SAR data requires a robust understanding of its unique statistical characteristics, particularly the presence of speckle noise, a granular interference pattern inherent to coherent imaging systems like SAR (ARGENTI et al., 2013).

Speckle arises from the constructive and destructive interference of backscattered signals within a resolution cell, manifesting as multiplicative, non-Gaussian noise that severely complicates image analysis (BARAHA; SAHOO, 2023). Hence, accurate processing and interpretation of SAR data depend critically on appropriate statistical models to describe speckle behavior.

Among the statistical frameworks available, the $\mathcal{G}_I^0$ distribution has been recognized for effectively characterizing SAR intensity data across various levels of scene heterogeneity. Its versatility comes from incorporating a texture parameter that accounts for the spatial variability of scatterers, thus generalizing the simpler Gamma distribution, which represents fully developed speckle typically found in homogeneous, textureless regions (FRERY et al., 1997; DE A. FERREIRA; NASCIMENTO, 2020). In practice, the Gamma model can be considered a limiting case of the $\mathcal{G}_I^0$ distribution as scene texture becomes homogeneous.

Parameter estimation for these statistical models, however, presents significant challenges, especially when using small-sized windows necessary to preserve spatial resolution in SAR images. Traditional parametric approaches, such as maximum likelihood estimation and moment-based methods, often become biased or unstable under these practical constraints (VASCONCELLOS; FRERY; SILVA, 2005; NASCIMENTO; CINTRA; FRERY, 2010). Moreover, likelihood ratio tests derived from these estimators may exhibit unreliable behavior when applied to small-window SAR data due to flat likelihood surfaces.

Entropy, introduced by Shannon (1948), quantifies the uncertainty associated with a random variable and has found extensive application across fields such as pattern recognition (AVVAL et

al., 2021), statistical physics (PRESSÉ et al., 2013), image processing (MOHAMMAD-DJAFARI, 2015), and particularly in SAR analysis (NASCIMENTO et al., 2014; NOBRE et al., 2016; NASCIMENTO; FRERY; CINTRA, 2019; CHAN; GAMBINI; FRERY, 2022). Beyond Shannon's original formulation, Rényi entropy generalizes the measure through an order parameter (RÉNYI, 1961), while Tsallis entropy offers an alternative non-additive generalization (TSALLIS, 1988). Recent studies highlight the role of entropy in SAR classification. Cassetti et al. (2022) evaluated entropy estimators in both supervised and unsupervised models. Gallet et al. (2024) proposed a Rényi divergence-based framework for explainable classification. Parikh et al. (2019) discussed challenges in deep learning for SAR, including limited availability of labeled data and the complexity of tuning hyperparameters. These works motivate lightweight, interpretable alternatives.

When the underlying distribution of data is unknown, entropy measures must be estimated non-parametrically. Spacing-based estimators, first proposed by Vasicek (1976) and further refined in subsequent studies (VAN ES, 1992; EBRAHIMI; PFLUGHOEFT; SOOFI, 1994; AL-OMARI, 2014), approximate entropy via spacings of order statistics. These estimators have desirable statistical properties, such as strong consistency and asymptotic normality under mild assumptions. Recent advancements have extended spacing-based methods to estimate Rényi entropy (AL-LABADI; CHU; XU, 2024). Importantly, spacing estimators do not rely on any specific model for the data and do not require choosing parameters, making them simple and flexible tools for entropy estimation.

1.1 MOTIVATION AND PROBLEM STATEMENT

Typically, SAR data exhibit heterogeneous clutter or fully developed speckle, depending on terrain characteristics and imaging conditions. Distinguishing between these two cases is critical for accurate interpretation and analysis.

While the $\mathcal{G}_I^0$ distribution effectively models heterogeneous SAR intensity data, practitioners face a significant challenge: choosing between simpler (Gamma-based) and more complex ($\mathcal{G}_I^0$-based) statistical models. Opting for the simpler Gamma model risks losing important texture information about scatterer variability, encapsulated within the $\mathcal{G}_I^0$ distribution's parameters (YUE et al., 2021). Conversely, directly applying the $\mathcal{G}_I^0$ distribution in homogeneous regions introduces substantial estimation difficulties, such as increased parameter estimation

bias and computational instability due to flat likelihood surfaces, particularly when analysis windows are small (FRERY; CRIBARI-NETO; SOUZA, 2004; NASCIMENTO; CINTRA; FRERY, 2010).

These estimation issues motivate the development of alternative methodologies that avoid explicit parametric estimation. In this context, non-parametric statistical tests based on entropy measures emerge as an appealing alternative. Such tests exploit entropy's sensitivity to deviations from homogeneity assumptions without relying on explicit parameter estimates.

This thesis proposes three novel entropy-based statistical tests (using Shannon, Rényi, and Tsallis entropies) designed specifically to distinguish heterogeneous clutter from fully developed speckle under the assumption that SAR intensity follows the Gamma SAR distribution in homogeneous regions. These tests assess whether observed entropy significantly differs from theoretical expectations under the homogeneity hypothesis, making them highly interpretable and practically applicable even when ground truth information is limited or unavailable.

To enhance accuracy, particularly within small-window analysis contexts common in practical SAR scenarios, we further propose a bootstrap-based bias-correction procedure for the entropy estimators. Overall, our approach provides robust, unsupervised statistical tools well-suited for operational scenarios, bridging a critical gap in existing methodologies.

1.2 OBJECTIVES

1.2.1 General Objective

To propose and evaluate entropy-based statistical tests for detecting heterogeneity in SAR imagery, using non-parametric estimation and bootstrap bias-correction to enhance accuracy in small-sample scenarios.

1.2.2 Specific Objectives

- To derive closed-form expressions for Rényi and Tsallis entropies under the Gamma SAR and $\mathcal{G}_I^0$ models, which serve as theoretical benchmarks for hypothesis testing.
- To identify and refine suitable non-parametric estimators of entropy for SAR data, incorporating bootstrap techniques to reduce bias and improve estimation accuracy.

- To formulate three entropy-based test statistics that compare the estimated entropy from observed data with its theoretical value under the homogeneity assumption.
- To evaluate the empirical size and power of the proposed tests via Monte Carlo simulations.
- To apply the proposed tests to both simulated and real SAR data using a sliding window scheme, and generate p-value maps for visual inspection and quantitative assessment.

1.3 CONTRIBUTIONS

The main contributions of this work are the following:

1. **Closed-form entropy derivations.** Analytical expressions for Rényi, and Tsallis entropies under the Gamma SAR and $\mathcal{G}_I^0$ models are derived, filling a gap in the literature and enabling hypothesis testing.
2. **Non-parametric estimator and bootstrap bias-correction.** A new spacing-based estimator is proposed for Tsallis entropy. A bootstrap bias-correction procedure is developed to improve the precision of all non-parametric estimators, substantially reducing bias and mean squared error in small-window analyses.
3. **Entropy-based test statistics.** Proposal of three entropy-based statistical tests for heterogeneity detection in SAR imagery, using Shannon, Rényi, and Tsallis entropy measures.

1.3.1 Related Publications

The following peer-reviewed articles and conference papers have been published as part of or related to this research:

- (2025): ALPALA, J.; NASCIMENTO, A. D. C.; FRERY, A. C. Quantifying Heterogeneity in SAR Imagery with the Rényi Entropy. *IEEE Geoscience and Remote Sensing Letters*, p. 1–1, 2025.
- (2024): FRERY, A. C.; ALPALA, J.; NASCIMENTO, A. D. C. Identifying Heterogeneity in SAR Data with New Test Statistics. *Remote Sensing*, v. 16, n. 11, p. 1973, 2024.

- (2024): ALPALA, J.; NASCIMENTO, A. D. C.; FRERY, A. C. Identifying departures from the fully developed speckle hypothesis in intensity SAR data with non-parametric estimation of the entropy. In: *2024 International Conference on Machine Intelligence for GeoAnalytics and Remote Sensing (MIGARS)*, 2024.

- (2023): ALPALA, R. J.; BORBA, A. A. De; FRERY, A. C. Quality Assessment measures for explainable fusion Of statistical evidences of edges in Polsar images: A First Approach. In: *IGARSS 2023 - IEEE International Geoscience and Remote Sensing Symposium*, 2023.

1.4 COMPUTATIONAL SUPPORT AND REPRODUCIBILITY

Simulations, tests, and data analyses presented in this thesis were implemented using the free, open-source programming language `R`[1] within `RStudio` (version 2025.09.1+401, `R` version 4.5.1). The manuscript was written in `Quarto`[2], a dynamic publishing system that integrates code, output, and narrative to ensure full reproducibility (BAUER; LANDESVATTER, 2023).

The numerical experiments were performed on a workstation equipped with an Intel® Core™Ultra 9 285 CPU (2.5 GHz, 24 cores), 128 GB RAM, and an NVIDIA® GeForce RTX 5090 GPU (31 GB VRAM), running Windows 11 Pro (version 24H2).

All code and data for this research, including the manuscript source, are available at https://github.com/rjaneth/Thesis-UFPE, supporting reproducibility. This work follows best practices recommended by Frery et al. (2020).

1.5 STRUCTURE OF THE THESIS

This thesis is organized into five chapters as follows:

- Chapter 2 presents the theoretical foundations of the work. It includes statistical modeling of SAR intensity data, entropy measures, and nonparametric estimation techniques based on order statistics.

[1] https://www.r-project.org/
[2] https://quarto.org/

- Chapter 3 describes the proposed methodology. It covers the selection and bias correction of entropy estimators, the construction of the test statistics, and the hypothesis testing framework based on Shannon, Rényi, and Tsallis entropy.
- Chapter 4 presents the results obtained from simulated and real SAR datasets. This includes both qualitative and quantitative analyses that demonstrate the effectiveness of the proposed methods.
- Chapter 5 summarizes the conclusions drawn from the study and outlines potential directions for future research.

2 THEORETICAL FOUNDATIONS

2.1 STATISTICAL MODELING OF INTENSITY SAR DATA

Statistical modeling plays a central role in the analysis of SAR imagery, where speckle is an inherent feature. For SAR intensity data, two main probability models are employed: the SAR-Gamma distribution (Γ_{SAR}), a reparameterization of the classical Gamma law suited to fully developed speckle, and the $\mathcal{G}_I^0$ distribution, which can describe varying levels of heterogeneity (FRERY et al., 1997).

We denote $Z \sim \Gamma_{\text{SAR}}(L, \mu)$ and $Z \sim \mathcal{G}_I^0(\alpha, \gamma, L)$ when the random variable Z follows the respective distributions, characterized by the following probability density functions (pdfs):

$$f_{\Gamma_{\text{SAR}}}\Big(z; \mu, L\Big) = \frac{L^L}{\Gamma(L)\,\mu^L} z^{L-1} \exp\left(-\frac{Lz}{\mu}\right) \mathbb{1}_{\mathbb{R}_+}(z) \tag{2.1}$$

and

$$f_{\mathcal{G}_I^0}\Big(z; \alpha, \gamma, L\Big) = \frac{L^L \Gamma(L-\alpha)}{\gamma^\alpha \Gamma(-\alpha)\Gamma(L)} \frac{z^{L-1}}{(\gamma + Lz)^{L-\alpha}} \mathbb{1}_{\mathbb{R}_+}(z), \tag{2.2}$$

where $\mu > 0$ is the mean intensity, $\gamma > 0$ is a scale parameter, $\alpha < 0$ controls the degree of texture (roughness), $L \geq 1$ is the number of looks (either nominal or estimated, thus not restricted to integer values), $\Gamma(\cdot)$ is the gamma function, and $\mathbb{1}_A(z)$ is the indicator function of the set A.

The rth order moments of the $\mathcal{G}_I^0$ model are

$$E\Big(Z^r\Big) = \left(\frac{\gamma}{L}\right)^r \frac{\Gamma(-\alpha - r)}{\Gamma(-\alpha)} \frac{\Gamma(L + r)}{\Gamma(L)}, \tag{2.3}$$

provided that $\alpha < -r$, and infinite otherwise. Therefore, assuming $\alpha < -1$, its expected value is

$$\mu = \left(\frac{\gamma}{L}\right) \frac{\Gamma(-\alpha - 1)}{\Gamma(-\alpha)} \frac{\Gamma(L + 1)}{\Gamma(L)} = -\frac{\gamma}{\alpha + 1}. \tag{2.4}$$

Although the $\mathcal{G}_I^0$ distribution is defined by the parameters α and γ, in the SAR literature (NASCIMENTO; CINTRA; FRERY, 2010) the texture α and the mean μ are usually used.

Reparameterizing (2.2) with μ, and denoting this model as $Z \sim \mathcal{G}_I^0(\alpha, \mu, L)$ we obtain:

$$f_{\mathcal{G}_I^0}\big(z; \alpha, \mu, L\big) = \frac{L^L\,\Gamma(L-\alpha)}{\Big[-\mu(\alpha+1)\Big]^{\alpha}\Gamma(-\alpha)\,\Gamma(L)}\frac{z^{L-1}}{\Big[-\mu(\alpha+1)+Lz\Big]^{L-\alpha}}\mathbb{1}_{\mathbb{R}_+}(z), \tag{2.5}$$

The Γ_{SAR} model is a particular case of the $\mathcal{G}_I^0$ distribution, as demonstrated in (FRERY et al., 1997). Specifically, for a given μ fixed,

$$f_{\mathcal{G}_I^0}\big(z; \alpha, \mu, L\big) \longrightarrow f_{\Gamma_{\mathsf{SAR}}}(z; \mu, L) \quad \text{when } \alpha \to -\infty.$$

In this work, we do not focus on parameter estimation using likelihood-based or moment-based methods. Instead, we adopt a hypothesis testing framework to detect heterogeneity in SAR imagery. The analytical expressions of entropy measures derived from the Γ_{SAR} and $\mathcal{G}_I^0$ models form the theoretical basis for constructing these statistical tests. In the following section, we introduce the entropy-based measures, specifically Shannon, Rényi, and Tsallis, on which our detection strategy is built.

2.2 ENTROPY MEASURES

Entropy stands as a foundational concept in information theory, originally formulated by Claude Shannon (1948). It provides a formal mechanism for quantifying the uncertainty or unpredictability of a random variable. More precisely, the entropy of a random variable can be interpreted as the average amount of information required to describe its outcomes based on its probability distribution. As such, entropy quantifies the expected information content of a random event, with higher values indicating more uncertainty or variability in the distribution. It plays a central role in a wide range of applications, including statistical physics (PACHTER; YANG; DILL, 2024), complex systems (BASHKIROV, 2006), machine learning (SEPÚLVEDA-FONTAINE; AMIGÓ, 2024), and remote sensing (JIAO et al., 2021).

This section focuses on three widely used entropy formulations that offer complementary perspectives on uncertainty: Shannon entropy H, Rényi entropy R_λ, and Tsallis entropy T_λ. In the context of continuous random variables, these measures take the form of *differential entropies*, which are defined using probability density functions. These differential entropies are not only theoretically grounded but also highly applicable to the statistical modeling of Synthetic Aperture Radar (SAR) data. Each entropy captures different aspects of distributional

structure and provides a flexible framework for heterogeneity analysis in SAR imagery.

Shannon entropy is the classical and most widely adopted measure, reflecting the average information content or uncertainty inherent in a random variable. It assumes statistical independence and extensivity, and serves as the baseline concept upon which generalizations are constructed.

Rényi entropy, introduced by Alfréd Rényi (1961), is a one-parameter generalization of Shannon's measure. By tuning the parameter $\lambda > 0$, the analyst can adjust the sensitivity of the entropy to the tails of the distribution. This property is particularly relevant in applications where rare events (e.g., bright scatterers, outliers) carry significant informational weight, such as in SAR-based texture discrimination or target detection.

Tsallis entropy was first introduced by Havrda and Charvát (1967) in the context of information theory. Later, Tsallis (1988) extended it by emphasizing its non-extensive features and placing it in a physical context. The generalized Tsallis entropy of order λ offers an alternative formulation motivated by non-extensive systems, such as those exhibiting long-range dependencies, memory effects, or multifractal behavior. Unlike Rényi entropy, it does not obey the additivity property under independence, making it particularly suitable for modeling complex spatial structures and textured regions in SAR images.

In the context of SAR imaging, homogeneous areas produce fully developed speckle and are effectively modeled by the $Z \sim \Gamma_{\mathsf{SAR}}(L, \mu)$ distribution. In contrast, textured or heterogeneous regions are better represented by the $Z \sim \mathcal{G}_I^0(\alpha, \mu, L)$ model, where the roughness parameter α controls the degree of heterogeneity. Across this section, we show that all three entropy measures applied to $\mathcal{G}_I^0$ can be decomposed as:

$$\boxed{\mathsf{Entropy}\left(\mathcal{G}_I^0\right) \;=\; \mathsf{Entropy}\left(\Gamma_{\mathrm{SAR}}\right) \;+\; \Delta_\alpha} \tag{2.6}$$

where Δ_α represents the *excess entropy* induced by the roughness parameter α. Notably, this excess vanishes in the homogeneous limit ($\alpha \to -\infty$), reducing (2.6) to the baseline case.

This decomposition plays a central role in the thesis. It forms the theoretical foundation for a statistical test to detect heterogeneity: if $\Delta_\alpha \neq 0$, then the observed region departs from the homogeneous model, signaling the presence of texture. Each entropy measure offers a different sensitivity profile to such deviations, and their comparative behavior provides valuable insights into the textural structure of SAR imagery.

This section details the closed-form expressions for H, R_λ, and T_λ under Γ_{SAR} and $\mathcal{G}_I^0$ models. Shannon entropy derivations are taken from literature and adapted to our parametrisation, whereas the Rényi and Tsallis expressions are original contributions derived as part of this research. At the end of the chapter, we summarize the common structure shared by all three measures and illustrate their convergence behavior.

2.2.1 Shannon Entropy

The parametric representation of Shannon entropy for a system described by a continuous random variable is:

$$H(Z) = -\mathbb{E}\Big[\ln f(z)\Big] = -\int_{\mathcal{B}} f(z)\ln f(z)\,\mathrm{d}z, \tag{2.7}$$

where $f(\cdot)$ is the pdf that characterizes the distribution of the real-valued random variable Z and $\mathcal{B} \subseteq \mathbb{R}$ denotes the support of $f(z)$.

Using the definition in (2.7), we derive closed-form expressions for the Shannon entropy of the Γ_{SAR} and $\mathcal{G}_I^0$ distributions under our parametrization.

Homogeneous case. For the Γ_{SAR} distribution defined in (2.1), we obtain:

$$H\Big(\Gamma_{\text{SAR}}(\mu, L)\Big) = L - \ln L + \ln\Gamma(L) + (1-L)\psi^{(0)}(L) + \ln\mu, \tag{2.8}$$

where $\psi^{(0)}(\cdot)$ is the digamma function; $H(\Gamma_{\text{SAR}})$ represents the baseline entropy of fully developed speckle.

Textured case. In the case of the $\mathcal{G}_I^0$ distribution (2.5), we adapt existing expressions reported by De A. Ferreira and Nascimento (2020) to our parametrization, using the relation $\mu = -\gamma/(\alpha+1)$. This yields:

$$H\Big(\mathcal{G}_I^0(\alpha,\mu,L)\Big) = H\Big(\Gamma_{\text{SAR}}(\mu,L)\Big) + \Big[(L-\alpha)\psi^{(0)}(L-\alpha) - (1-\alpha)\psi^{(0)}(-\alpha) + \ln(-1-\alpha) - \ln\Gamma(L-\alpha) + \ln\Gamma(-\alpha) - L\Big]. \tag{2.9}$$

Equation (2.9) can be interpreted as:

$$H(\mathcal{G}_I^0) = \underbrace{H\Big(\Gamma_{\text{SAR}}\Big)}_{\text{baseline entropy}} + \underbrace{\Delta_\alpha}_{\text{excess entropy caused by texture}},$$

where

$$\Delta_\alpha = (L-\alpha)\,\psi^{(0)}(L-\alpha) - (1-\alpha)\,\psi^{(0)}(-\alpha) + \ln(-1-\alpha) \\ - \ln\Gamma(L-\alpha) + \ln\Gamma(-\alpha) - L, \quad (2.10)$$

the extra term Δ_α captures how much entropy increases due to texture (heterogeneity), caused by the roughness parameter α. When $\alpha \to -\infty$ (fully developed speckle), the excess term tends to zero, and Equation (2.9) collapses to the homogeneous case in (2.8), i.e.,

$$\lim_{\alpha\to-\infty} H\Big(\mathcal{G}_I^0(\alpha,\mu,L)\Big) = H\Big(\Gamma_{\mathrm{SAR}}(\mu,L)\Big).$$

Appendix A provides a proof of this limiting behavior. In practice, detecting heterogeneity is equivalent to testing whether Δ_α is significantly different from zero.

2.2.2 Rényi Entropy

For a continuous random variable Z with pdf $f(z)$, the Rényi entropy of order $\lambda \in \mathbb{R}_+ \setminus \{1\}$ is defined as:

$$R_\lambda(Z) = \frac{1}{1-\lambda}\ln\Big[\mathbb{E}\Big(f^{\lambda-1}(Z)\Big)\Big] = \frac{1}{1-\lambda}\ln\int_{\mathcal{B}}[f(z)]^\lambda\,\mathrm{d}z, \quad (2.11)$$

where $\mathcal{B} \subseteq \mathbb{R}$ denotes the support of $f(z)$. As $\lambda \to 1$, $R_\lambda(Z)$ reduces to the Shannon entropy $H(Z)$.

Using (2.11), we now derive the closed-form expression for the Rényi entropy under the homogeneous (Γ_{SAR}) model.

Homogeneous case. Let $Z \sim \Gamma_{\mathrm{SAR}}(\mu, L)$ with pdf given in (2.1). We compute

$$I = \int_0^\infty \Big[f_{\Gamma_{\mathrm{SAR}}}(z;\mu,L)\Big]^\lambda\,\mathrm{d}z = \Big(\tfrac{L^L}{\Gamma(L)\,\mu^L}\Big)^\lambda \int_0^\infty z^{\lambda(L-1)}\exp\Big(-\tfrac{\lambda L}{\mu}\,z\Big)\,\mathrm{d}z.$$

Using the Gamma integral identity

$$\int_0^\infty x^{p-1}e^{-qx}\,\mathrm{d}x = \frac{\Gamma(p)}{q^p}, \quad p,q>0,$$

with

$$p = \lambda(L-1)+1, \quad q = \frac{\lambda L}{\mu},$$

we obtain

$$I = \Big(\tfrac{L^L}{\Gamma(L)\,\mu^L}\Big)^{\lambda} \frac{\Gamma\Big(\lambda(L-1)+1\Big)}{\Big(\tfrac{\lambda L}{\mu}\Big)^{\lambda(L-1)+1}}.$$

Taking logarithms and simplifying gives

$$\ln I = (1-\lambda)\Big(\ln\mu - \ln L\Big) - \lambda\,\ln\Gamma(L) + \ln\Gamma\Big(\lambda(L-1)+1\Big) - \Big(\lambda(L-1)+1\Big)\ln\lambda.$$

Substituting into (2.11) yields the closed-form

$$\boxed{R_\lambda(\Gamma_{\mathrm{SAR}}(\mu,L)) = \ln\mu - \ln L + \frac{1}{1-\lambda}\Big[-\lambda\,\ln\Gamma(L) + \ln\Gamma\big(\lambda(L-1)+1\big) - \big(\lambda(L-1)+1\big)\ln\lambda\Big].} \tag{2.12}$$

Textured case. Starting from the definition of Rényi entropy in (2.11) and the pdf of $Z \sim \mathcal{G}_I^0(\alpha,\gamma,L)$ given in (2.2), we define:

$$I = \int_0^\infty \Big[f_{\mathcal{G}_I^0}(z;\alpha,\gamma,L)\Big]^\lambda \,\mathrm{d}z = C^\lambda \int_0^\infty \frac{z^{\lambda(L-1)}}{(\gamma+Lz)^{\,\lambda(L-\alpha)}}\,\mathrm{d}z, \qquad C = \frac{L^L\Gamma(L-\alpha)}{\gamma^\alpha\Gamma(-\alpha)\Gamma(L)}.$$

The parameterisation satisfies $\gamma = -\mu(\alpha+1)$, so the final result will be expressed in terms of μ.

$$I \;=\; \int_0^\infty \Big[f_{\mathcal{G}_I^0}(z;\alpha,\gamma,L)\Big]^\lambda \,\mathrm{d}z \;=\; C^\lambda \int_0^\infty \frac{z^{\lambda(L-1)}}{(\gamma+Lz)^{\,\lambda(L-\alpha)}}\,\mathrm{d}z,$$

With the change of variable $t = Lz/\gamma$ ($\mathrm{d}z = \gamma\ \mathrm{d}t/L$) we obtain:

$$I = C^\lambda\,\frac{\gamma^{\,1+\lambda(\alpha-1)}}{L^{\,1+\lambda(L-1)}} \int_0^\infty \frac{t^{\lambda(L-1)}}{(1+t)^{\,\lambda(L-\alpha)}}\,\mathrm{d}t.$$

Using the Beta–function identity

$$\int_0^\infty \frac{t^{a-1}}{(1+t)^{a+b}}\,\mathrm{d}t = B(a,b), \quad a = \lambda(L-1)+1, \quad b = \lambda(-\alpha+1)-1,$$

it follows that

$$I = C^\lambda\,\frac{\gamma^{\,1+\lambda(\alpha-1)}}{L^{\,1+\lambda(L-1)}}\,B(a,b).$$

Next, we note that $\gamma^{\,1+\lambda(\alpha-1)} = \gamma^{\,1-\lambda+\lambda\alpha}$ and $L^{\,1+\lambda(L-1)} = L^{\,\lambda L+1-\lambda}$. Since

$$C^\lambda = \left(\frac{L^L}{\gamma^\alpha\,\Gamma(-\alpha)\,\Gamma(L)}\,\Gamma(L-\alpha)\right)^\lambda = L^{\lambda L}\,\gamma^{-\alpha\lambda}\Big(\tfrac{\Gamma(L-\alpha)}{\Gamma(-\alpha)\,\Gamma(L)}\Big)^\lambda,$$

we obtain

$$I = \gamma^{1-\lambda} L^{\lambda-1} \left(\frac{\Gamma(L-\alpha)}{\Gamma(-\alpha)\,\Gamma(L)} \right)^{\lambda} B(a,b).$$

By (2.11), the Rényi entropy, is given by:

$$R_\lambda(Z) = \frac{1}{1-\lambda} \ln I = \frac{1}{1-\lambda} \ln\Big[\gamma^{1-\lambda} L^{\lambda-1} \left(\frac{\Gamma(L-\alpha)}{\Gamma(-\alpha)\,\Gamma(L)} \right)^{\lambda} B(a,b) \Big].$$

Thus, for $Z \sim \mathcal{G}_I^0(\alpha, \gamma, L)$,

$$R_\lambda\Big(\mathcal{G}_I^0(\alpha,\gamma,L)\Big) = \ln\Big(\frac{\gamma}{L}\Big) + \frac{1}{1-\lambda}\Big[\lambda\Big(\ln\Gamma(L-\alpha) - \ln\Gamma(-\alpha) - \ln\Gamma(L)\Big) + \ln B(a,b)\Big].$$

Using the property

$$\ln B(a,b) = \ln\Gamma(a) + \ln\Gamma(b) - \ln\Gamma(a+b),$$

where $a + b = \lambda(L-\alpha)$, we have

$$R_\lambda\Big(\mathcal{G}_I^0(\alpha,\gamma,L)\Big) = \ln\Big(\frac{\gamma}{L}\Big) + \frac{1}{1-\lambda}\Big[\lambda\Big(\ln\Gamma(L-\alpha) - \ln\Gamma(-\alpha) - \ln\Gamma(L)\Big) + \ln\Gamma(a) + \ln\Gamma(b) - \ln\Gamma\Big(\lambda(L-\alpha)\Big)\Big]. \quad (2.13)$$

Finally, noting that $\gamma = -\mu(\alpha+1)$ from (2.3), and substituting this expression into (2.13), we obtain:

$$R_\lambda\Big(\mathcal{G}_I^0(\alpha,\mu,L)\Big) = \ln\mu - \ln L + \ln(-1-\alpha) + \frac{1}{1-\lambda}\Big[\lambda\Big(\ln\Gamma(L-\alpha) - \ln\Gamma(-\alpha) - \ln\Gamma(L)\Big) + \ln\Gamma\Big(\lambda(L-1)+1\Big) + \ln\Gamma\Big(\lambda(-\alpha+1)-1\Big) - \ln\Gamma\Big(\lambda(L-\alpha)\Big)\Big],$$

This expression extends the Rényi entropy of the $\Gamma_{\mathrm{SAR}}(\mu, L)$ model (2.12) by including additional terms that depend on the texture parameter α. Specifically:

$$\boxed{\begin{aligned} R_\lambda(\mathcal{G}_I^0(\alpha,\mu,L)) = R_\lambda(\Gamma_{\mathrm{SAR}}(\mu,L)) + \ln(-1-\alpha) \\ + \frac{1}{1-\lambda}[\lambda(\ln\Gamma(L-\alpha) - \ln\Gamma(-\alpha)) + \ln\Gamma(\lambda(-\alpha+1)-1) \\ - \ln\Gamma(\lambda(L-\alpha)) + (\lambda(L-1)+1)\ln\lambda]. \end{aligned}} \quad (2.14)$$

Equation (2.14) can be read as:

$$R_\lambda(\mathcal{G}_I^0) = \underbrace{R_\lambda\Big(\Gamma_{\mathrm{SAR}}\Big)}_{\text{baseline entropy}} + \underbrace{\Delta_\alpha^R}_{\text{excess entropy caused by texture}},$$

where

$$\Delta_{\alpha}^{R} = \ln(-1-\alpha) + \frac{1}{1-\lambda}\Big[\lambda\Big(\ln\Gamma(L-\alpha) - \ln\Gamma(-\alpha)\Big) + \ln\Gamma\Big(\lambda(-\alpha+1)-1\Big) - \ln\Gamma\Big(\lambda(L-\alpha)\Big) + \Big(\lambda(L-1)+1\Big)\ln\lambda\Big], \quad (2.15)$$

the excess term Δ_{α}^{R} depends on the heterogeneity parameter α, and $\Delta_{\alpha}^{\mathrm{R}} \to 0$ when $\alpha \to -\infty$, validating the decomposition, i.e.,

$$\lim_{\alpha\to-\infty} R_{\lambda}\Big(\mathcal{G}_{I}^{0}(\alpha,\mu,L)\Big) = R_{\lambda}\Big(\Gamma_{\mathrm{SAR}}(L,\mu)\Big).$$

Appendix A provides proof of this limiting behavior.

2.2.3 Tsallis Entropy

For a continuous random variable Z with pdf $f(z)$, the Tsallis entropy of order $\lambda \in \mathbb{R}_{+}\setminus\{1\}$ is defined as:

$$T_{\lambda}(Z) = \frac{1}{\lambda-1}\mathbb{E}\Big[1-(f(Z))^{\lambda-1}\Big] = \frac{1}{\lambda-1}\Big[1-\int_{\mathcal{B}}\Big(f(z)\Big)^{\lambda}\,\mathrm{d}z\Big], \quad (2.16)$$

where $\mathcal{B}\subseteq\mathbb{R}$ denotes the support of $f(z)$. In the limit $\lambda\to 1$, $T_{\lambda}(Z)\to H(Z)$, making Tsallis a one-parameter generalization of Shannon entropy.

Using (2.16), we derive closed-form expressions for the Tsallis entropy of the Γ_{SAR} and the $\mathcal{G}_{I}^{0}$ distributions.

Homogeneous case. Let $Z\sim\Gamma_{\mathrm{SAR}}(\mu,L)$ with pdf given by (2.1). Define the integral:

$$I = \int_{0}^{\infty}\left[f_{\Gamma_{\mathsf{SAR}}}(z;\mu,L)\right]^{\lambda}\,\mathrm{d}z.$$

Substituting the density function and simplifying constants, we get

$$I = \left(\frac{L^{L}}{\Gamma(L)\,\mu^{L}}\right)^{\lambda}\int_{0}^{\infty} z^{\lambda(L-1)}\exp\left(-\frac{\lambda L}{\mu}z\right)\,\mathrm{d}z.$$

Using the Gamma integral identity

$$\int_{0}^{\infty} x^{p-1}e^{-qx}\,\mathrm{d}x = \frac{\Gamma(p)}{q^{p}}, \quad p,q>0,$$

with $p = \lambda(L-1)+1$ and $q = \frac{\lambda L}{\mu}$. This leads to

$$I = \left(\frac{L^L}{\Gamma(L)\,\mu^L}\right)^{\lambda} \cdot \frac{\Gamma\Big(\lambda(L-1)+1\Big)}{\left(\frac{\lambda L}{\mu}\right)^{\lambda(L-1)+1}}.$$

After rearranging powers of L, μ and λ, we obtain

$$I = \frac{L^{\lambda-1}\,\mu^{1-\lambda}\,\Gamma\Big(\lambda(L-1)+1\Big)}{\lambda^{\lambda(L-1)+1}\,\left[\Gamma(L)\right]^{\lambda}}. \tag{2.17}$$

Substituting Equation (2.17) into the Tsallis entropy definition (2.16), we have:

$$T_\lambda\Big(\Gamma_{\mathsf{SAR}}(\mu,L)\Big) = \frac{1}{\lambda-1}\left[1 - \frac{L^{\lambda-1}\,\mu^{1-\lambda}\,\Gamma\Big(\lambda(L-1)+1\Big)}{\lambda^{\lambda(L-1)+1}\,\left[\Gamma(L)\right]^{\lambda}}\right]. \tag{2.18}$$

This expression can also be written in an equivalent form:

$$\boxed{\begin{aligned} T_\lambda(\Gamma_{\mathrm{SAR}}(\mu,L)) = \frac{1}{\lambda-1}\Big\{1 - \exp\Big[&(1-\lambda)\ln\mu + (\lambda-1)\ln L + \ln\Gamma(\lambda(L-1)+1) \\ &-\lambda\ln\Gamma(L) - (\lambda(L-1)+1)\ln\lambda\Big]\Big\}. \end{aligned}} \tag{2.19}$$

Textured case. Starting from the Tsallis definition in (2.16) and the pdf of $Z \sim \mathcal{G}_I^0(\alpha,\gamma,L)$ in (2.2), define:

$$I = \int_0^\infty \left[f_{\mathcal{G}_I^0}(z)\right]^{\lambda} \mathrm{d}z,$$

which, upon substitution of the density, becomes

$$I = \left[\frac{L^L\Gamma(L-\alpha)}{\gamma^\alpha\Gamma(-\alpha)\Gamma(L)}\right]^{\lambda} \int_0^\infty \frac{z^{\lambda(L-1)}}{(\gamma+Lz)^{\lambda(L-\alpha)}}\,\mathrm{d}z.$$

Introducing the change of variables $t = \frac{Lz}{\gamma}$ (so that $z = \frac{\gamma t}{L}$ and $\mathrm{d}z = \frac{\gamma}{L}\,\mathrm{d}t$), we obtain

$$\begin{aligned} I &= \left[\frac{L^L\Gamma(L-\alpha)}{\gamma^\alpha\Gamma(-\alpha)\Gamma(L)}\right]^{\lambda} \frac{\gamma}{L}\int_0^\infty \frac{\left(\frac{\gamma t}{L}\right)^{\lambda(L-1)}}{[\gamma(1+t)]^{\lambda(L-\alpha)}}\,\mathrm{d}t \\ &= \left[\frac{L^L\Gamma(L-\alpha)}{\gamma^\alpha\Gamma(-\alpha)\Gamma(L)}\right]^{\lambda} \frac{\gamma^{1+\lambda(\alpha-1)}}{L^{1+\lambda(L-1)}}\int_0^\infty t^{\lambda(L-1)}(1+t)^{-\lambda(L-\alpha)}\,\mathrm{d}t. \end{aligned} \tag{2.20}$$

This integral matches the Beta function identity

$$\int_0^\infty \frac{t^{a-1}}{(1+t)^{a+b}}\,\mathrm{d}z = B(a,b) = \frac{\Gamma(a)\Gamma(b)}{\Gamma(a+b)},$$

for parameters

$$a = \lambda(L-1)+1, \quad b = \lambda(-\alpha+1)-1.$$

Using this, we simplify (2.20) to

$$I = \left[\frac{\Gamma(L-\alpha)}{\Gamma(-\alpha)\Gamma(L)}\right]^\lambda \frac{\gamma^{1-\lambda}}{L^{1-\lambda}} \cdot \frac{\Gamma(a)\Gamma(b)}{\Gamma(a+b)}. \tag{2.21}$$

To express I in terms of the mean μ, we use the relation $\gamma = -\mu(\alpha+1)$ valid for $\alpha < -1$. Substituting into (2.21) gives

$$I = [-\mu(\alpha+1)]^{1-\lambda} L^{\lambda-1} \left[\frac{\Gamma(L-\alpha)}{\Gamma(-\alpha)\Gamma(L)}\right]^\lambda \frac{\Gamma(a)\Gamma(b)}{\Gamma(\lambda(L-\alpha))}.$$

Finally, substituting this expression into (2.16), we obtain:

$$T_\lambda\Big(\mathcal{G}_I^0(\alpha,\mu,L)\Big) = \frac{1}{\lambda-1}\left\{[-\mu(\alpha+1)]^{1-\lambda} L^{\lambda-1} \left[\frac{\Gamma(L-\alpha)}{\Gamma(-\alpha)\Gamma(L)}\right]^\lambda \frac{\Gamma(a)\Gamma(b)}{\Gamma(\lambda(L-\alpha))}\right\}.$$

This expression extends the Tsallis entropy of the $\Gamma_{\mathrm{SAR}}(\mu,L)$ model (2.19) by including additional terms that depend on the texture parameter α. It can be written in an exponential-logarithmic form as:

$$\begin{aligned} T_\lambda(\mathcal{G}_I^0(\mu,\alpha,L)) = T_\lambda(\Gamma_{\mathrm{SAR}}(\mu,L)) \; + \; \frac{1}{\lambda-1}\exp\Big[&(1-\lambda)\ln\mu + (\lambda-1)\ln L + \ln\Gamma(\lambda(L-1)+1) \\ &-\lambda\ln\Gamma(L)\Big]\Big\{1-\exp\Big[(1-\lambda)\ln(-\alpha-1) + \lambda\ln\Gamma(L-\alpha) - \lambda\ln\Gamma(-\alpha) \\ &+\ln\Gamma(\lambda(1-\alpha)-1) - \ln\Gamma(\lambda(L-\alpha))\Big]\Big\}. \end{aligned} \tag{2.22}$$

Equation (2.22) can be interpreted as:

$$T_\lambda(\mathcal{G}_I^0) = \underbrace{T_\lambda\Big(\Gamma_{\mathrm{SAR}}\Big)}_{\text{baseline entropy}} \quad + \quad \underbrace{\Delta_\alpha^T}_{\text{excess entropy caused by texture}},$$

where

$$\Delta_\alpha^T = \frac{1}{\lambda-1}\exp\Big[(1-\lambda)\ln\mu + (\lambda-1)\ln L + \ln\Gamma\Big(\lambda(L-1)+1\Big) - \lambda\ln\Gamma(L)\Big] \Big\{1 - \exp\Big[(1-\lambda)\ln(-\alpha-1) + \lambda\ln\Gamma(L-\alpha) - \lambda\ln\Gamma(-\alpha) + \ln\Gamma\Big(\lambda(1-\alpha)-1\Big) - \ln\Gamma\Big(\lambda(L-\alpha)\Big)\Big]\Big\}, \quad (2.23)$$

the excess term Δ_α^T depends on the heterogeneity parameter α, and $\Delta_\alpha^T \to 0$ when $\alpha \to -\infty$, validating the decomposition, i.e.,

$$\lim_{\alpha\to-\infty} T_\lambda\Big(\mathcal{G}_I^0(\alpha,\mu,L)\Big) = T_\lambda\Big(\Gamma_{\mathrm{SAR}}(L,\mu)\Big).$$

Appendix A provides proof of this limiting behavior.

Figure 1 provides a conceptual overview of the decomposition structure of the differential entropy for the heterogeneous model $\mathcal{G}_I^0$. This entropy is expressed as the sum of a baseline term corresponding to the homogeneous Γ_{SAR} distribution and an excess term Δ_α that reflects the contribution of texture. The decomposition applies to the three entropy measures considered in this study: Shannon (2.9), Rényi (2.14), and Tsallis (2.22). In all cases, the excess term depends on the roughness parameter α and vanishes as $\alpha \to -\infty$, thus recovering the homogeneous case.

Figure 1 – Conceptual diagram of entropy decomposition.

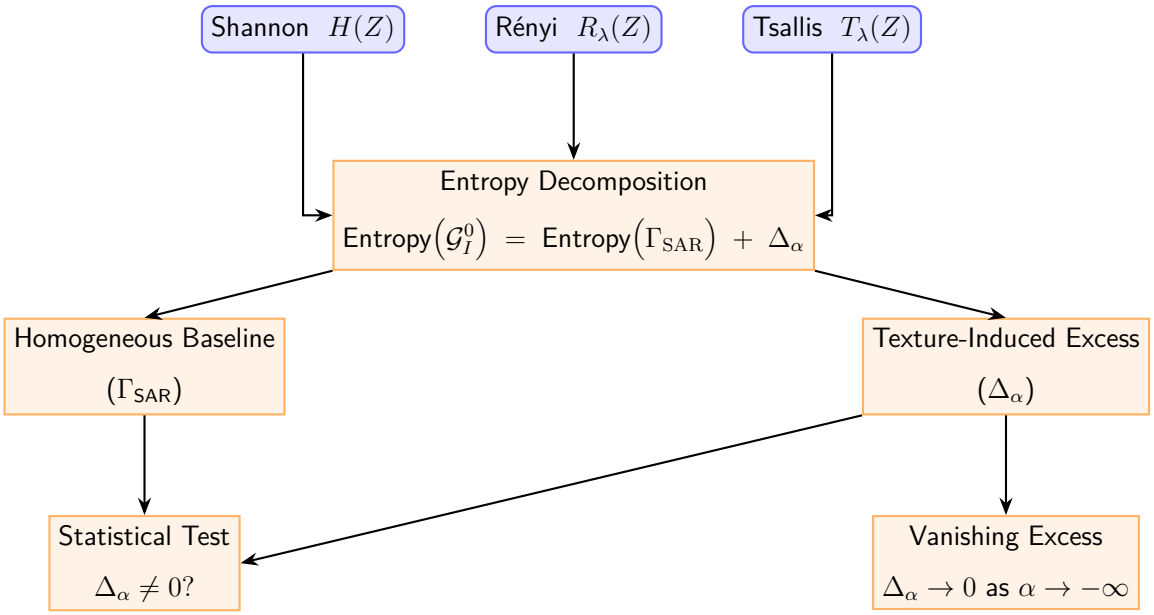

Source: The author (2025)

To conclude this section, we illustrate the convergence behavior of each entropy measure.

Figures 2–4 illustrate the Shannon (H), Rényi (R_λ), and Tsallis (T_λ) entropies for the $\mathcal{G}_I^0$ model under different texture levels (α) and numbers of looks (L). In every case the coloured dashed curves converge to the solid black baseline of the homogeneous Γ_{SAR} distribution as $\alpha \to -\infty$, confirming the limiting behavior.

For the Shannon entropy (Figure 2), when $L = 5$ the entropy curves for different α values are more concentrated. This is due to the higher speckle noise present in a low number of looks, which dominates the uncertainty and masks texture effects. When $L = 18$, speckle is reduced and the entropy better reflects texture variation, resulting in more separated curves.

In the case of Rényi entropy (Figure 3), for $\lambda = 0.6$ and $\lambda = 0.9$, the general shape and separation of the curves are similar. However, increasing L leads to a slight decrease in entropy values across all α, consistent with reduced speckle. The convergence pattern toward the Gamma baseline remains stable in both settings.

For Tsallis entropy (Figure 4), the separation between curves is most noticeable for $\lambda = 0.6$ and $L = 5$, where texture has more influence. When λ increases to 0.9 or when L is increased, the curves become more compact and approach the Gamma entropy faster, indicating lower sensitivity to texture variation and confirming that λ controls the influence of the tail behavior.

Figure 2 – Shannon entropy $H(\mathcal{G}_I^0)$ converges to $H(\Gamma_{\mathrm{SAR}})$ as α decreases.

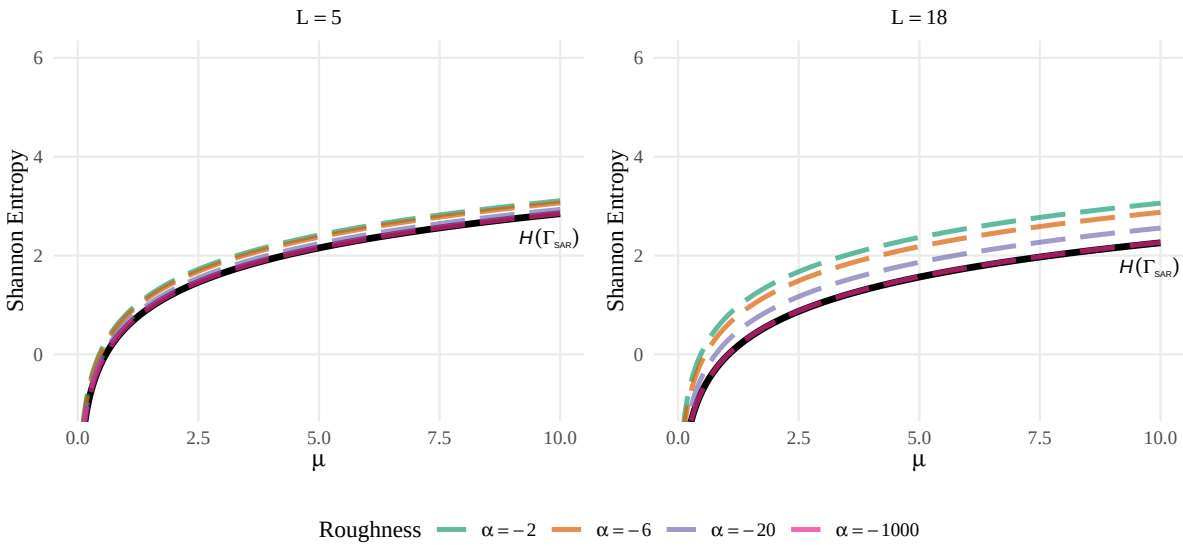

Source: The author (2025)

Figure 3 – Rényi entropy $R_\lambda(\mathcal{G}_I^0)$ converges to $R_\lambda(\Gamma_{\mathrm{SAR}})$ as α decreases.

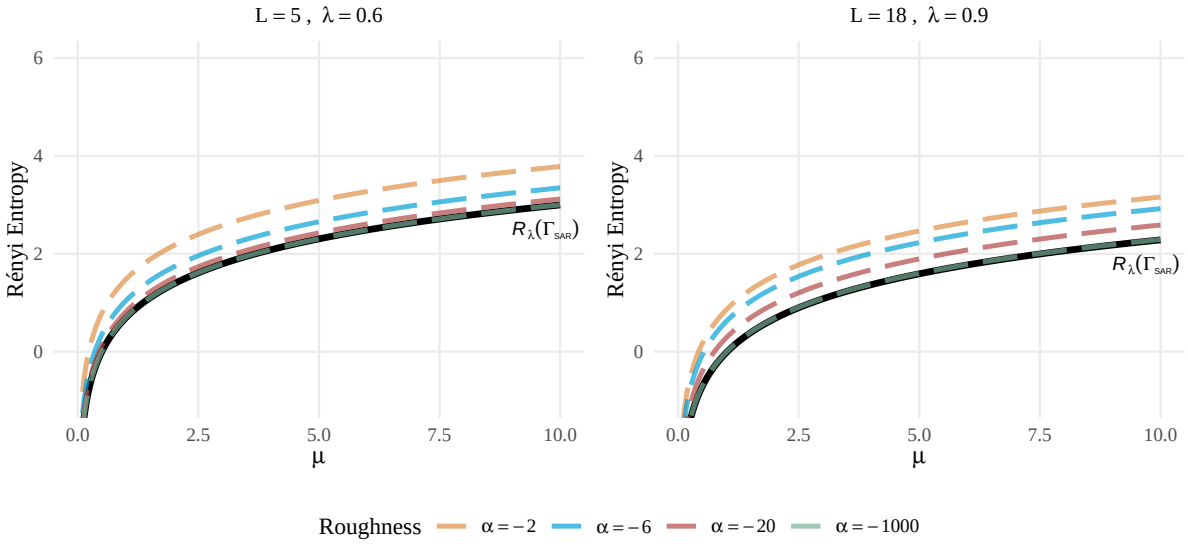

Source: The author (2025)

Figure 4 – Tsallis entropy $T_\lambda(\mathcal{G}_I^0)$ converges to $T_\lambda(\Gamma_{\mathrm{SAR}})$ as α decreases.

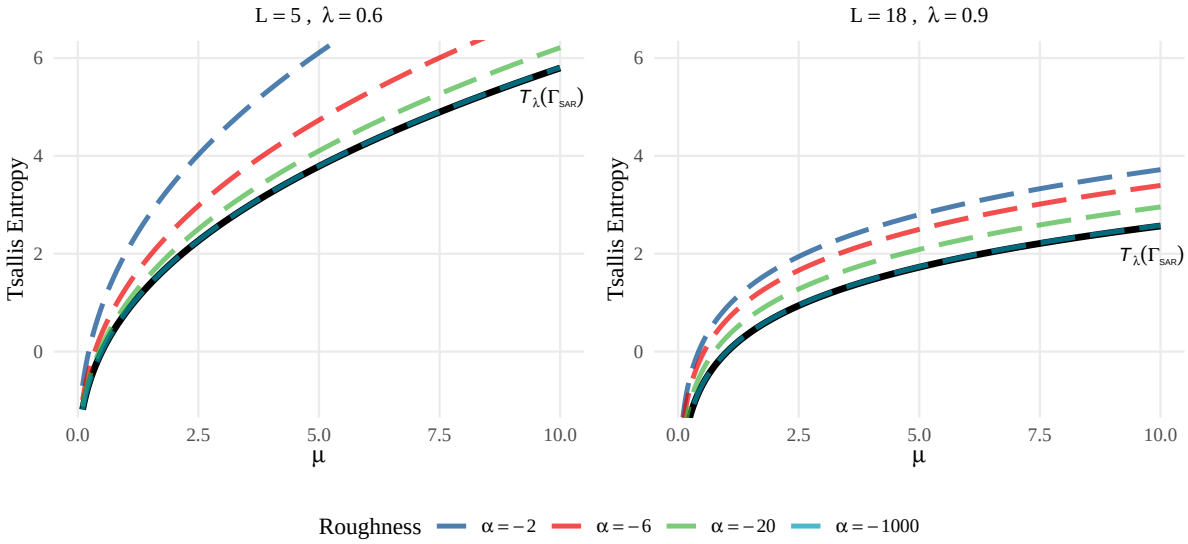

Source: The author (2025)

2.3 ORDER STATISTICS AND NONPARAMETRIC ESTIMATORS

Parametric estimation of entropy begins by assuming a family for $f(z)$ (e.g. exponential, Gaussian). The data are used to estimate the parameters of this family (for example, sample mean and variance for a normal). These parameter estimates are then substituted into the corresponding analytical expression for entropy $H(f)$.

While parametric methods can be very efficient if the assumption is correct, they suffer when the true distribution deviates from the chosen model. In such cases, parametric estimates of entropy can be heavily biased or misleading.

Nonparametric estimation, by contrast, tries to approximate $H(f)$ without assuming any specific form for the underlying distribution. A common approach is the plug-in method, where the density $\hat{f}(z)$ is first estimated from the data, using tools like histograms or kernel methods. This estimated density is then used in the entropy formula. However, estimating the density accurately can be difficult, especially when the data are limited or high-dimensional.

An alternative route, which we pursue here, is to avoid explicit density estimation and instead use properties of the sorted sample (order statistics) to estimate entropy. This spacing-based approach is appealing because it directly targets the entropy functional, often achieving consistency and good convergence rates without the intermediate step of full density estimation.

In the following, we introduce the concept of order statistics and sample spacings, and derive how the entropy integral can be transformed into a convenient form involving the quantile function. This will set the stage for constructing entropy estimators based on sample spacings.

2.3.1 Order Statistics and Sample Spacings

Let $\boldsymbol{Z} = (Z_1, Z_2, \ldots, Z_n)$ be an independent and identically distributed (i.i.d.) random sample of size n from drawn from a continuous distribution with cumulative distribution function (cdf) $F(z)$, let $Z_{(1)} \leq Z_{(2)} \leq \cdots \leq Z_{(n)}$ denote the ordered sample, known as the order statistics.

Sample spacings refer to the differences between ordered observations. More generally, an m-spacing is defined as the difference between two order statistics that are m positions apart in the sorted sample. For instance, a 1-spacing corresponds to the gap between consecutive order statistics: $Z_{(i+1)} - Z_{(i)}$. In general, an m-spacing can be written as $Z_{(i+m)} - Z_{(i)}$, for indices i such that $i + m \leq n$.

These spacings are inversely related to the underlying density: where the density is high, observations tend to cluster and spacings are small; where the density is low, spacings are typically larger. This relationship forms the basis for using spacings to estimate the density function or related functionals like entropy.

A key probabilistic property that supports this idea arises when considering the transformed

values $U_i = F(Z_{(i)})$, which follow the order statistics of a uniform distribution on $[0, 1]$. For $i = 1, \ldots, n-1$, the expected spacing in the transformed domain is:

$$\mathbb{E}[F(Z_{(i+1)}) - F(Z_{(i)})] = \frac{1}{n+1}.$$

This result suggests that, under the true cdf, the transformed spacings are uniformly spread in expectation. Consequently, a simple density estimate around the point $Z_{(i)}$ can be motivated by the approximation:

$$f(Z_{(i)}) \approx \frac{\text{mass}}{\text{length}} \approx \frac{1/(n+1)}{Z_{(i+1)} - Z_{(i)}},$$

where $1/(n+1)$ serves as an estimate of the probability mass between $Z_{(i)}$ and $Z_{(i+1)}$.

2.3.2 Nonparametric Estimators for Shannon Entropy

Let $F^{-1}(p)$ denote the quantile function (inverse cdf) of the distribution. We use $Q(p)$ as shorthand for $F^{-1}(p)$, so $Q : (0, 1) \to \mathbb{R}$ satisfies $Q(p) = z$ if and only if $F(z) = p$.

Since $F(z)$ is monotonic, $Q(p)$ is differentiable wherever $f(z)$ is positive, with derivative $Q'(p) = \frac{d}{\mathrm{d}p} F^{-1}(p)$. By the inverse function theorem, $Q'(p) = \frac{1}{f(Q(p))}$.

Starting from the definition of Shannon entropy in Equation (2.7), a change of variables $p = F(z)$ can be applied. When $z = Q(p)$, it follows that $\mathrm{d}z = Q'(p)\,\mathrm{d}p$. Substituting into the integral:

$$\begin{aligned} H(Z) &= -\int_0^1 f(Q(p)) \ln f(Q(p)) \cdot Q'(p)\,\mathrm{d}p \\ &= -\int_0^1 \ln f(Q(p))\,\mathrm{d}p. \end{aligned}$$

Now using $f(Q(p)) = 1/Q'(p)$, we have $\ln f(Q(p)) = -\ln Q'(p)$. Thus:

$$H(Z) = \int_0^1 \ln Q'(p)\,\mathrm{d}p = \int_0^1 \ln\left(\frac{d}{\mathrm{d}p} F^{-1}(p)\right) \mathrm{d}p. \tag{2.24}$$

This is the foundation of spacing estimators: entropy as the integral of the log quantile derivative.

In practice, we estimate $Q'(p)$ using order statistics. Consider:

$$Q'(p) \approx \frac{n+1}{2m}(Z_{(i+m)} - Z_{(i-m)}), \quad m \le i \le n - m. \tag{2.25}$$

By taking logarithms and averaging over i, Vasicek's estimator becomes:

$$\widehat{H}_{\mathsf{V}}(\boldsymbol{Z}) = \frac{1}{n}\sum_{i=1}^{n} \ln\left[\frac{n}{2m}(Z_{(i+m)} - Z_{(i-m)})\right]. \tag{2.26}$$

Vasicek (1976) showed that under regularity conditions ($m \to \infty$, $m/n \to 0$), $\widehat{H}_{\mathsf{V}} \to H(f)$ in probability.

Nonparametric estimators using order statistics and spacings, such as Vasicek's m-spacing estimator, provide a flexible alternative to model-based entropy estimation. By converting the entropy integral into a quantile-based form (see Appendix B), these estimators offer robust, consistent estimation of Shannon entropy without requiring explicit density estimation.

Subsequent extensions and refinements (not detailed here) further improve bias, variance, and performance at the boundaries, forming a robust toolkit for entropy estimation in continuous distributions.

We consider the following entropy estimators variants as discussed by Cassetti et al. (2022).

Van Es (1992) proposed a new estimator of entropy given by:

$$\widehat{H}_{\mathsf{VE}}(\boldsymbol{Z}) = \frac{1}{n-m}\sum_{i=1}^{n-m} \ln\left[\frac{n+1}{m}\left(Z_{(i+m)} - Z_{(i)}\right)\right] + \sum_{k=m}^{n}\frac{1}{k} + \ln\frac{m}{n+1}. \tag{2.27}$$

Under some conditions, Van Es proved asymptotic normality of this estimator.

Ebrahimi et al. (1994) adjusted the weights of Vasicek's estimator, in order to take into account the fact that the differences are truncated around the smallest and the largest data points. Specifically, $Z_{(i+m)} - Z_{(i-m)}$ is substituted with $Z_{(i+m)} - Z_{(1)}$ when $i \leq m$ and $Z_{(i+m)} - Z_{(i-m)}$ is replaced by $Z_{(n)} - Z_{(i-m)}$ when $i \geq n-m+1$. Their estimator is given by:

$$\widehat{H}_{\mathsf{E}}(\boldsymbol{Z}) = \frac{1}{n}\sum_{i=1}^{n} \ln\left[\frac{n}{c_i m}\left(Z_{(i+m)} - Z_{(i-m)}\right)\right], \tag{2.28}$$

where

$$c_i = \begin{cases} 1 + (i-1)/m & \text{if} \quad 1 \leq i \leq m, \\ 2 & \text{if} \quad m+1 \leq i \leq n-m, \\ 1 + (n-i)/m & \text{if} \quad n-m+1 \leq i \leq n. \end{cases}$$

Correa (1995) suggested another modification of Vasicek's estimator. In estimation the density f of F in the interval $\left(Z_{(i-m)}, Z_{(i+m)}\right)$ he used a local linear model based on $2m+1$

points: $F\left(Z_{(j)}\right) = a + bZ_{(j)} + \varepsilon, j = m - i, \ldots, m + i$. This yields a following estimator:

$$\widehat{H}_{\mathsf{C}}(\boldsymbol{Z}) = -\frac{1}{n}\sum_{i=1}^{n} \ln \frac{\sum_{j=i-m}^{i+m}(j-i)\left(Z_{(j)} - \overline{Z}_{(i)}\right)}{n\sum_{j=i-m}^{i+m}\left(Z_{(j)} - \overline{Z}_{(i)}\right)^2}, \tag{2.29}$$

where $\overline{Z}_{(i)} = (2m+1)^{-1}\sum_{j=i-m}^{i+m} Z_{(j)}$, $m < \frac{n}{2}$, $Z_{(i)} = Z_{(1)}$ for $i < 1$ and $Z_{(i)} = Z_{(n)}$ for $i > n$. Based on simulations, he showed that his estimator has a smaller mean square error than Vasicek's approach.

Noughabi and Arghami (2010) modify the coefficients of Ebrahimi et al. (1994) as:

$$\widehat{H}_{\mathsf{N}}(\boldsymbol{Z}) = \frac{1}{n}\sum_{i=1}^{n} \ln\left[\frac{n}{a_i m}\left(Z_{(i+m)} - Z_{(i-m)}\right)\right], \tag{2.30}$$

where

$$a_i = \begin{cases} 1 & \text{if} \quad 1 \le i \le m, \\ 2 & \text{if} \quad m+1 \le i \le n-m, \\ 1 & \text{if} \quad n-m+1 \le i \le n, \end{cases}$$

and $Z_{(i-m)} = Z_{(1)}$ for $i \le m$ and $Z_{(i+m)} = Z_{(n)}$ for $i \ge n - m$.

Al-Omari (2014) suggested the following estimator:

$$\widehat{H}_{\mathsf{AO}}(\boldsymbol{Z}) = \frac{1}{n}\sum_{i=1}^{n} \ln\left[\frac{n}{\omega_i m}\left(Z_{(i+m)} - Z_{(i-m)}\right)\right], \tag{2.31}$$

where

$$\omega_i = \begin{cases} 3/2 & \text{if} \quad 1 \le i \le m, \\ 2 & \text{if} \quad m+1 \le i \le n-m, \\ 3/2 & \text{if} \quad n-m+1 \le i \le n, \end{cases}$$

in which $Z_{(i-m)} = Z_{(1)}$ for $i \le m$, and $Z_{(i+m)} = Z_{(n)}$ for $i \ge n - m$.

These estimators are asymptotically consistent, i.e., they converge in probability to the true value when $m, n \to \infty$ and $m/n \to 0$.

2.3.3 A Nonparametric Estimator of Rényi Entropy

The Rényi entropy of order $\lambda > 0$, with $\lambda \neq 1$, is defined in Equation (2.11) as a generalization of Shannon entropy. It introduces an adjustable parameter λ that controls the

sensitivity of the entropy measure to the tails of the distribution.

To facilitate nonparametric estimation, the expression in Equation (2.11) can be reformulated using the quantile function $Q(p) = F^{-1}(p)$, with $p \in (0, 1)$. Applying the change of variable $z = Q(p)$ and noting that $f(Q(p)) = Q'(p)$ yields:

$$\begin{aligned}\int f^{\lambda}(z)\,\mathrm{d}z &= \int_0^1 [f(Q(p))]^{\lambda} \cdot Q'(p)\,\mathrm{d}p \\ &= \int_0^1 [Q'(p)]^{1-\lambda}\,\mathrm{d}p.\end{aligned}$$

Substituting this into the original expression gives the quantile-based representation:

$$R_{\lambda}(Z) = \frac{1}{1-\lambda} \ln\left(\int_0^1 [Q'(p)]^{1-\lambda}\,\mathrm{d}p\right). \tag{2.32}$$

A nonparametric estimator can be constructed by approximating the quantile derivative $Q'(p)$ using m-spacings, following the methodology proposed by Al-Labadi, Chu and Xu (2024). Given a sample $\boldsymbol{Z} = (Z_1, \ldots, Z_n)$ drawn i.i.d. from F, let $Z_{(1)} \leq \cdots \leq Z_{(n)}$ denote the order statistics. For a spacing parameter $m \in \{1, \ldots, \lfloor n/2 \rfloor\}$, define the boundary-corrected m-spacing as:

$$D_{i,m} = Z_{(i+m)} - Z_{(i-m)}, \qquad Z_{(i-m)} := Z_{(1)} \text{ if } i \leq m, \quad Z_{(i+m)} := Z_{(n)} \text{ if } i \geq n - m.$$

To mitigate boundary bias, the position-dependent correction factor introduced by Ebrahimi et al. (1994) is used:

$$c_i = \begin{cases} \dfrac{m+i-1}{m}, & 1 \leq i \leq m, \\ 2, & m+1 \leq i \leq n-m, \\ \dfrac{n+m-i}{m}, & n-m+1 \leq i \leq n. \end{cases}$$

The corresponding m-spacing density estimate at the ith order statistic is given by:

$$\widehat{f}_n(Z_{(i)}) = \frac{c_i\, m/n}{D_{i,m}}, \qquad i = 1, \ldots, n. \tag{2.33}$$

Substituting (2.33) into the quantile form (2.32) and approximating the integral by a Riemann sum yields the nonparametric plug-in estimator for Rényi entropy:

$$\widehat{R}_\lambda(\boldsymbol{Z}) = \frac{1}{1-\lambda} \ln \left[\frac{1}{n} \sum_{i=1}^{n} \left(\frac{c_i \, m/n}{Z_{(i+m)} - Z_{(i-m)}} \right)^{\lambda-1} \right]. \tag{2.34}$$

This estimator extends the m-spacing approach originally introduced for Shannon entropy to the broader Rényi family, enabling consistent nonparametric estimation without requiring direct estimation of the density function.

2.3.4 A Nonparametric Estimator of Tsallis Entropy

Following the approach of Vasicek (1976) and Ebrahimi et al. (1994) for Shannon entropy, and the methodology for Rényi entropy proposed by Al-Labadi, Chu and Xu (2024), we derive a nonparametric estimator for Tsallis entropy.

A detailed derivation of this estimator, including the quantile-based transformation and spacing approximation, is provided in Appendix B.

The definition of Tsallis entropy is given in Equation (2.16), this expression can be reformulated using the quantile function $Q(p) = F^{-1}(p)$, defined for $p \in (0,1)$. Since $f(Q(p)) = 1/Q'(p)$, the expectation in (2.16) becomes

$$\mathbb{E}\big[f^{\lambda-1}(Z)\big] = \int_0^1 \big(Q'(p)\big)^{1-\lambda} \, \mathrm{d}p,$$

leading to the alternative representation:

$$T_\lambda(Z) = \frac{1}{\lambda - 1} \left\{ 1 - \int_0^1 \big(Q'(p)\big)^{1-\lambda} \, \mathrm{d}p \right\}. \tag{2.35}$$

To estimate $T_\lambda(Z)$ nonparametrically, consider an i.i.d. sample $Z_1, \ldots, Z_n \sim F$, with associated order statistics $Z_{(1)} \leq \cdots \leq Z_{(n)}$. Let $m \in \{1, \ldots, \lfloor n/2 \rfloor\}$ be an integer spacing parameter. For each $i = 1, \ldots, n$, define the m-spacing

$$D_{i,m} \;=\; Z_{(i+m)} - Z_{(i-m)}, \quad Z_{(i-m)} := Z_{(1)} \text{ if } i \leq m, \quad Z_{(i+m)} := Z_{(n)} \text{ if } i \geq n - m.$$

Since the empirical distribution satisfies $F_n(Z_{(i\pm m)}) = \frac{i\pm m}{n}$, the length of the interval is $\frac{2m}{n}$, and Vasicek's plug-in estimator of the density is given by

$$\tilde{f}_{i,m} \;=\; \frac{2m}{n}\, D_{i,m}^{-1}.$$

To reduce boundary bias, Ebrahimi et al. (1994) proposed a position-dependent correction factor

$$c_i \;=\; \begin{cases} 1 + \dfrac{i-1}{m}, & 1 \le i \le m, \\ 2, & m+1 \le i \le n-m, \\ 1 + \dfrac{n-i}{m}, & n-m+1 \le i \le n, \end{cases}$$

resulting in the boundary-corrected m-spacing density estimator

$$\widehat{f}_n\big(Z_{(i)}\big) \;=\; \frac{c_i\, m/n}{D_{i,m}}, \qquad i = 1, \ldots, n. \tag{2.36}$$

Approximating the integral in (2.35) with a Riemann sum centered at $p_i \approx \frac{i}{n}$ and replacing $Q'(p)$ with the estimator in (2.36), we obtain the nonparametric plug-in estimator

$$\begin{aligned} \widehat{T}_\lambda(\boldsymbol{Z}) &= \frac{1}{\lambda - 1}\left\{1 - \frac{1}{n}\sum_{i=1}^{n}\left[\widehat{f}_n(Z_{(i)})\right]^{\lambda-1}\right\} \\ &= \frac{1}{\lambda - 1}\left\{1 - \frac{1}{n}\sum_{i=1}^{n}\left(\frac{c_i\, m/n}{Z_{(i+m)} - Z_{(i-m)}}\right)^{\lambda-1}\right\}. \end{aligned} \tag{2.37}$$

3 METHODOLOGY

3.1 SELECTION OF THE BEST SHANNON ENTROPY ESTIMATORS

Although several nonparametric estimators have been proposed for Shannon entropy, their performance depends on factors such as sample size and the underlying distribution. We evaluate the six estimators described in Section 2.3.2: the Vasicek (2.26), Van Es (2.27), Ebrahimi et al. (2.28), Correa (2.29), Noughabi–Arghami (2.30), and Al–Omari (2.31) estimators. Their performance is evaluated through a simulation study under fixed conditions. The selection is based on two standard criteria: bias and mean squared error (MSE).

The goal of this analysis is to identify the estimators with the best overall performance, which will then be used in the subsequent stages of the methodology, including bootstrap correction and hypothesis testing. This selection process is exclusive to Shannon entropy, as only a single estimator was considered for Rényi and Tsallis entropies.

Our experimental setup involves the analysis of bias and MSE for each estimator through a Monte Carlo study. For each sample size $n \in \{9, 25, 49, 81, 121\}$, we generate 1000 independent synthetic samples from $Z \sim \Gamma_{\mathsf{SAR}}(5, 1)$. The results are consistent across other values of μ and L. We adopt the heuristic spacing $m = [\sqrt{n} + 0.5]$, a choice commonly recommended in the literature (WIECZORKOWSKI; GRZEGORZEWSKI, 1999).

Figure 5 presents the bias and MSE for each of the non-parametric estimators of Shannon entropy. The results are summarized in Table 1.

As shown in the simulation results, the estimators $\widehat{H}_{\mathsf{C}}$, $\widehat{H}_{\mathsf{E}}$, and $\widehat{H}_{\mathsf{AO}}$ show low bias and achieve convergence for sample sizes larger than 81. These estimators exhibit good behavior in terms of bias and MSE across various parameter combinations.

In contrast, estimator $\widehat{H}_{\mathsf{N}}$ displays the lowest MSE across all scenarios. However, the bias remains unchanged and high for sample sizes larger than 25, indicating that the convergence is not very fast. Additionally, we observe that both $\widehat{H}_{\mathsf{V}}$ and $\widehat{H}_{\mathsf{VE}}$ estimators exhibit larger bias and slower convergence compared to their counterparts. Notably, the $\widehat{H}_{\mathsf{V}}$ estimator shows the highest MSE.

Although the estimators $\widehat{H}_{\mathsf{C}}$, $\widehat{H}_{\mathsf{E}}$, and $\widehat{H}_{\mathsf{AO}}$ demonstrate good performance in terms of bias and MSE for sufficiently large samples (e.g., $n \geq 81$), practical scenarios in SAR image processing often involve much smaller sample sizes. In particular, local texture analysis is

Figure 5 – Performance of Shannon entropy estimators under $\Gamma_{\mathrm{SAR}}(5, 1)$.

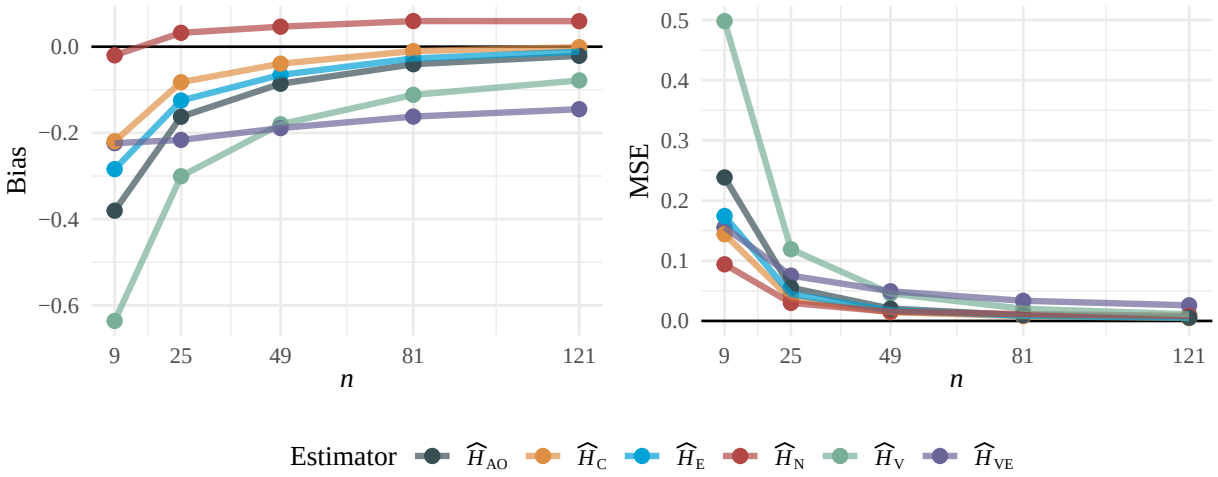

Source: The author (2025)

Table 1 – Bias and MSE of Shannon entropy estimators under $\Gamma_{\mathrm{SAR}}(5, 1)$

		Bias						MSE					
μ	n	$\widehat{H}_{\mathrm{V}}$	$\widehat{H}_{\mathrm{VE}}$	$\widehat{H}_{\mathrm{E}}$	$\widehat{H}_{\mathrm{C}}$	$\widehat{H}_{\mathrm{N}}$	$\widehat{H}_{\mathrm{AO}}$	$\widehat{H}_{\mathrm{V}}$	$\widehat{H}_{\mathrm{VE}}$	$\widehat{H}_{\mathrm{E}}$	$\widehat{H}_{\mathrm{C}}$	$\widehat{H}_{\mathrm{N}}$	$\widehat{H}_{\mathrm{AO}}$
1	9	−0.636	−0.224	**−0.284**	**−0.219**	−0.020	**−0.380**	0.498	0.156	**0.174**	**0.144**	0.094	**0.238**
	25	−0.300	−0.216	**−0.125**	**−0.082**	0.032	**−0.162**	0.119	0.075	**0.044**	**0.036**	0.030	**0.055**
	49	−0.180	−0.189	**−0.065**	**−0.039**	0.046	**−0.086**	0.046	0.049	**0.017**	**0.015**	0.015	**0.021**
	81	−0.112	−0.162	**−0.027**	**−0.010**	0.059	**−0.041**	0.020	0.034	**0.009**	**0.008**	0.011	**0.009**
	121	−0.078	−0.145	**−0.012**	**−0.001**	0.059	**−0.021**	0.011	0.026	**0.005**	**0.005**	0.008	**0.005**

Source: The author (2025)

typically performed on small windows, such as 7×7, which correspond to $n = 49$. Under these conditions, bias can become significant, and convergence is slower or incomplete.

To address this issue and improve estimation accuracy in small-sample regimes, we introduce a bootstrap-based correction methodology. The next subsection presents the bias-reduction procedure and the definition of the corrected entropy estimator.

3.2 BOOTSTRAP BIAS CORRECTION FOR ENTROPY ESTIMATORS

The nonparametric estimators of entropy considered in this work include the Shannon entropy $\widehat{H}(\boldsymbol{Z})$, the Rényi entropy $\widehat{R}_\lambda(\boldsymbol{Z})$, and the Tsallis entropy $\widehat{T}_\lambda(\boldsymbol{Z})$. We assume that these estimators are inherently biased; that is, their expected value does not coincide with the

true entropy, as shown in Equation (3.1):

$$\mathrm{Bias}(\widehat{\theta}) = \mathbb{E}[\widehat{\theta}] - \theta \neq 0, \tag{3.1}$$

where $\widehat{\theta}$ denotes any of the estimators listed above, and θ is the corresponding true entropy value.

To reduce this bias, we apply a bootstrap correction method. Let $\boldsymbol{Z} = (Z_1, Z_2, \ldots, Z_n)$ be a random sample of size n from an unknown distribution. Using bootstrap resampling, we generate B new samples $\boldsymbol{Z}^{(1)}, \boldsymbol{Z}^{(2)}, \ldots, \boldsymbol{Z}^{(B)}$ by sampling with replacement from $\boldsymbol{Z}$. For each bootstrap sample $\boldsymbol{Z}^{(b)}$, we compute the corresponding estimator $\widehat{\theta}(\boldsymbol{Z}^{(b)})$.

The bias is then estimated using Equation (3.2), which calculates the difference between the average of the bootstrap estimates and the original estimate:

$$\widehat{\mathrm{Bias}} = \frac{1}{B}\sum_{b=1}^{B} \widehat{\theta}(\boldsymbol{Z}^{(b)}) - \widehat{\theta}(\boldsymbol{Z}). \tag{3.2}$$

A bias-corrected estimator is then defined by subtracting the estimated bias from the original estimator, as expressed in Equation (3.3):

$$\widetilde{\theta} = \widehat{\theta} - \widehat{\mathrm{Bias}}. \tag{3.3}$$

Substituting the estimate from Equation (3.2) into Equation (3.3) yields the explicit formula for the corrected estimator:

$$\widetilde{\theta} = 2\widehat{\theta}(\boldsymbol{Z}) - \frac{1}{B}\sum_{b=1}^{B} \widehat{\theta}(\boldsymbol{Z}^{(b)}). \tag{3.4}$$

Thus, $\widetilde{\theta}$ is an approximately unbiased estimator of θ. The effectiveness of the correction depends on the number of bootstrap replicates B and the characteristics of the underlying distribution, but it systematically reduces bias, particularly when working with small sample sizes.

To distinguish the bootstrap-improved estimators from their original forms, we adopt the following notation: $\widetilde{H}_{\mathsf{V}}$, $\widetilde{H}_{\mathsf{VE}}$, $\widetilde{H}_{\mathsf{E}}$, $\widetilde{H}_{\mathsf{C}}$, $\widetilde{H}_{\mathsf{N}}$, and $\widetilde{H}_{\mathsf{AO}}$, respectively. For the other entropy types, we denote the bootstrap-corrected estimators as $\widetilde{R}_\lambda$ for Rényi entropy and $\widetilde{T}_\lambda$ for Tsallis entropy.

In order to assess the effectiveness of the bootstrap technique, we present comparisons of the bias and MSE between each original non-parametric Shannon entropy estimator and

its respective bootstrap-enhanced version, using samples from the $\Gamma_{\mathsf{SAR}}(5, 1)$, with $B = 100$ bootstrap replicates and varying n, as shown in Figures 6a–6f.

Figure 6 – Comparing Bias and MSE: original vs. bootstrap estimators, with, $\mu = 1$ and $L = 5$.

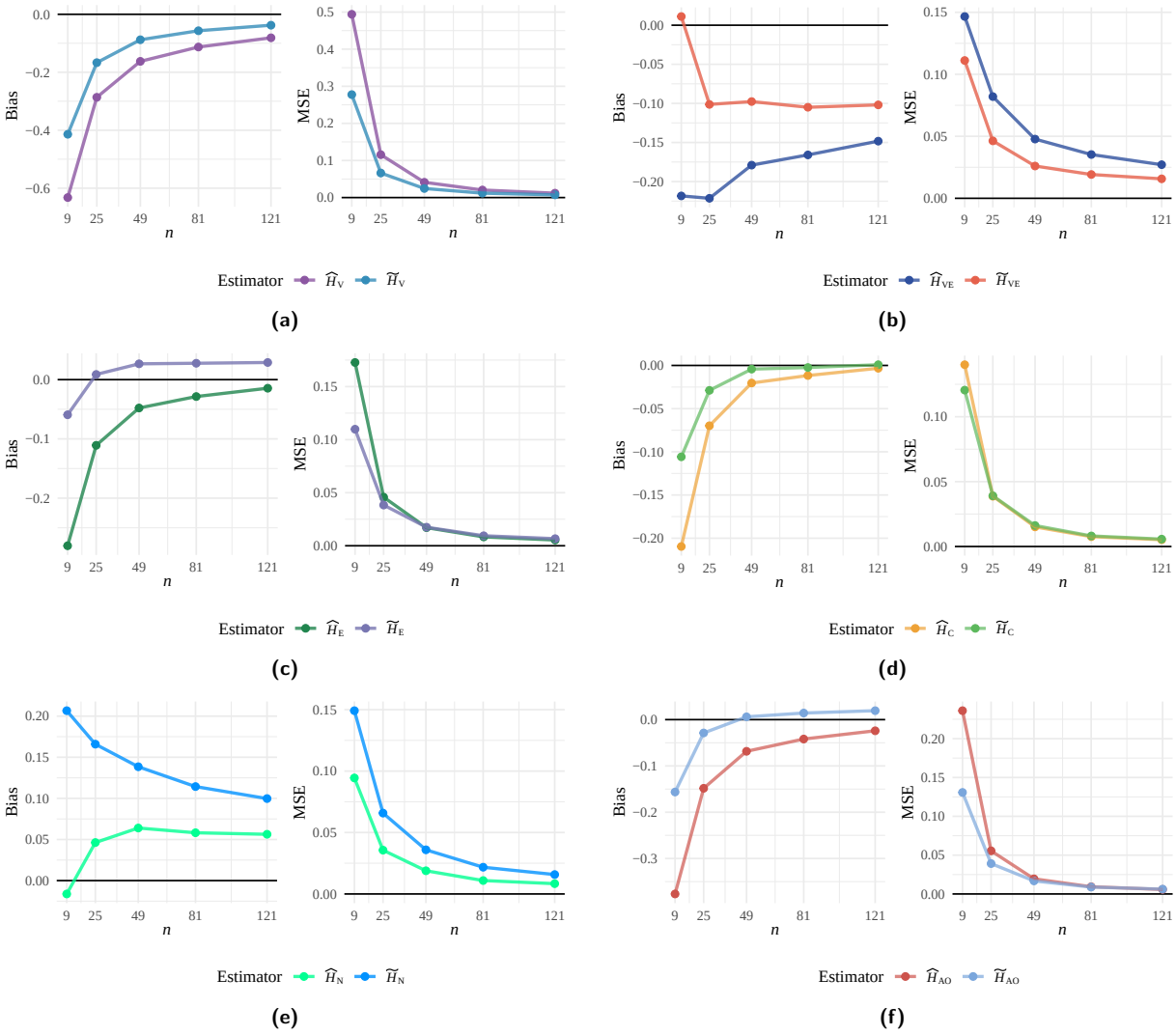

Source: The author (2025)

The estimators $\widetilde{H}_{\mathsf{V}}$ and $\widetilde{H}_{\mathsf{VE}}$ show consistent bias reduction, though convergence remains slow. For $\widetilde{H}_{\mathsf{E}}$, the correction improves bias only for small n, while its MSE steadily decreases. In contrast, the bootstrap technique did not improve the $\widetilde{H}_{\mathsf{N}}$ estimator. This might occur because the original estimator overestimates the entropy values, showing a positive bias. This tendency to overestimate persists with the use of bootstrap, contributing to an increase in bias and MSE. The most notable improvements are observed with $\widetilde{H}_{\mathsf{C}}$ and $\widetilde{H}_{\mathsf{AO}}$, which achieve both low bias and MSE even for small sample sizes, demonstrating faster convergence.

While the bias-corrected estimator $\widetilde{\theta}$ is theoretically motivated to reduce bias, its effectiveness is not guaranteed for all entropy estimators. In practice, the performance of the bootstrap correction varies depending on the characteristics of the original estimator and the sample size.

To finalize the selection of the non-parametric Shannon entropy estimator used in the following simulations, we consider the execution time of the bootstrap versions of $\widetilde{H}_{\mathsf{C}}$ and $\widetilde{H}_{\mathsf{AO}}$.

Table 2 shows the processing time of each estimator across different settings of L and n. The results indicate that $\widetilde{H}_{\mathsf{AO}}$ consistently achieves lower computational times compared to $\widetilde{H}_{\mathsf{C}}$. This makes it the more efficient option, particularly relevant for large datasets, such as SAR images discussed in Chapter 4. Consequently, $\widetilde{H}_{\mathsf{AO}}$ is selected as the representative non-parametric Shannon entropy estimator in the simulations presented in the following sections.

Table 2 – Processing time for bootstrap-improved estimators $\widetilde{H}_{\mathsf{C}}$ and $\widetilde{H}_{\mathsf{AO}}$

Estimator	$\boldsymbol{L}$	$\boldsymbol{n}$	**Time** (s)
$\widetilde{H}_{\mathsf{C}}$	5	25	4.94
		49	8.62
		81	14.77
		121	27.97
	18	25	10.72
		49	20.26
		81	32.98
		121	48.56
$\widetilde{H}_{\mathsf{AO}}$	5	25	**2.46**
		49	**2.73**
		81	**3.18**
		121	**3.83**
	18	25	**2.39**
		49	**2.75**
		81	**3.20**
		121	**3.74**

Source: The author (2025)

3.2.1 Optimal λ Selection

We aim to determine the optimal order λ for the nonparametric entropy estimators of Rényi ($\widetilde{R}_{\lambda}$) and Tsallis ($\widetilde{T}_{\lambda}$), using simulated samples of size $n = 49$ from $Z \sim \Gamma_{\mathsf{SAR}}(5, 1)$ distribution.

To assess estimator performance, we conducted a Monte Carlo simulation with $R = 1000$ replications. For each value of λ, independent samples were generated, and entropy was estimated for each sample using the bootstrap bias-corrected version with $B = 100$ resamples to reduce bias. The resulting estimates were compared to the theoretical entropy to compute the bias and MSE. This simulation-based procedure allows us to evaluate how the choice of λ affects estimation accuracy, and whether the bootstrap improves performance.

For the Rényi estimator (see Figure 7), $\lambda = 0.9$ minimizes the MSE while keeping the bias low, achieving a favorable bias-variance trade-off. Although $\lambda = 0.85$ yields slightly lower bias, it produces a higher MSE, supporting the choice of $\lambda = 0.9$ as optimal.

Similarly, for the Tsallis estimator (Figure 8), $\lambda = 0.85$ results in the lowest MSE with moderate bias, making it the most suitable choice.

The estimators remained numerically stable and converged smoothly to Shannon entropy as $\lambda \to 1$. Outside this range ($\lambda < 0.7$ or $\lambda > 1$), bias and MSE increased, indicating reduced numerical precision. These results confirm that the selected λ values ensure stable and reliable entropy estimates under typical SAR conditions.

Figure 7 – Bias and MSE as a function of λ, for the Rényi entropy estimator, with $n = 49$, $L = 5$.

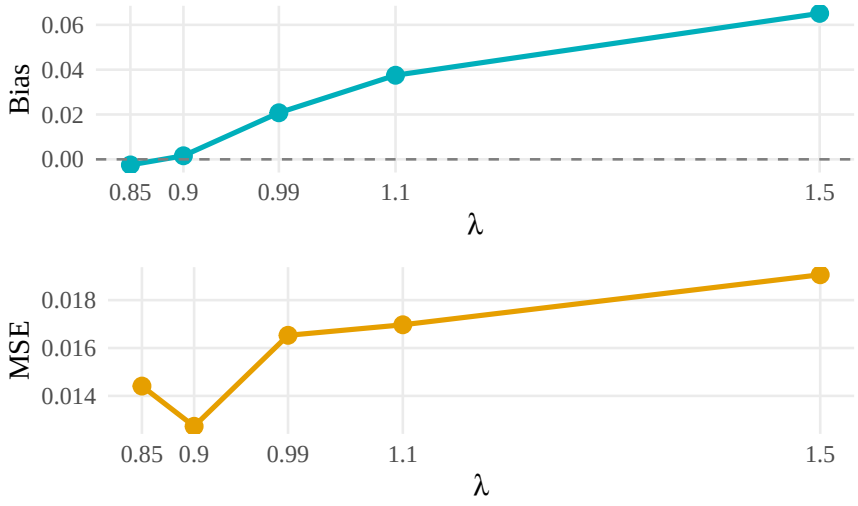

Source: The author (2025)

In the case of $L = 1$, the bootstrap procedure does not provide meaningful improvement and often leads to unstable estimates. Therefore, we omit bootstrap in this setting. Under these conditions, higher values of λ yield better results: $\lambda = 3$ is preferred for the Rényi estimator, and $\lambda = 1.2$ for the Tsallis estimator.

Figure 8 – Bias and MSE as a function of λ, for the Tsallis entropy estimator, with $n = 49$, $L = 5$.

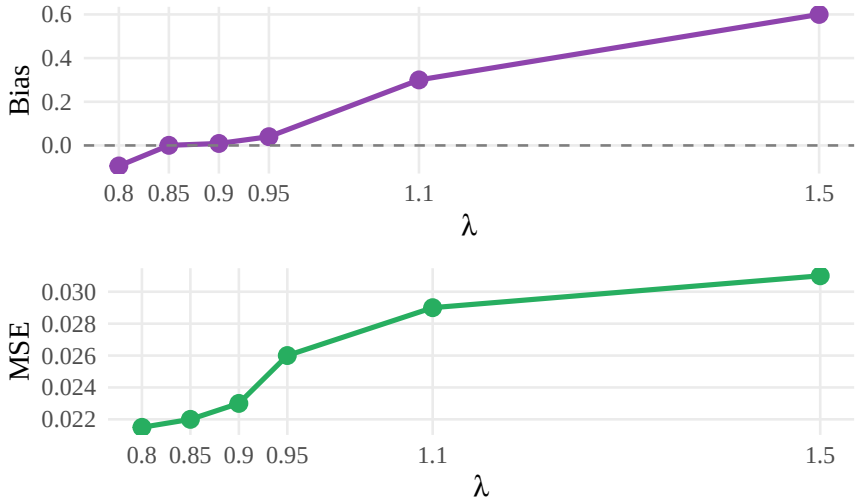

Source: The author (2025)

3.2.2 Bootstrap Bias Correction in Rényi and Tsallis Entropy Estimation

Building upon the previous Monte Carlo setup, we further assess the performance of the Rényi and Tsallis entropy estimators by analyzing their behavior across varying sample sizes $n \in \{9, 25, 49, 81, 121\}$. Using the optimal values of the order parameter ($\lambda = 0.9$ for Rényi and $\lambda = 0.85$ for Tsallis) already identified in the earlier analysis, we compute the bias and MSE for both the original and bootstrap-corrected versions of the estimators. As illustrated in Figures 9 and 10, the bootstrap estimators consistently show improved performance for small samples.

Figure 9 – Bias and MSE of the Rényi entropy estimators for Γ_{SAR}, with $L = 5$

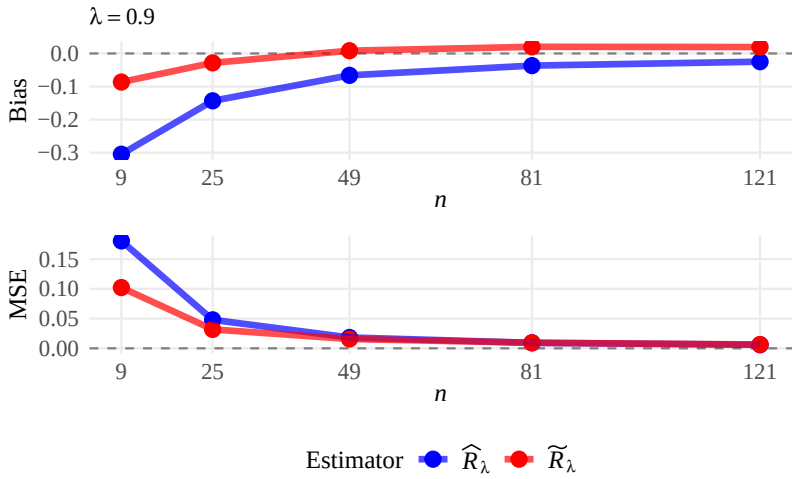

Source: The author (2025)

Figure 10 – Bias and MSE of the Tsallis entropy estimators for Γ_{SAR}, with $L = 5$

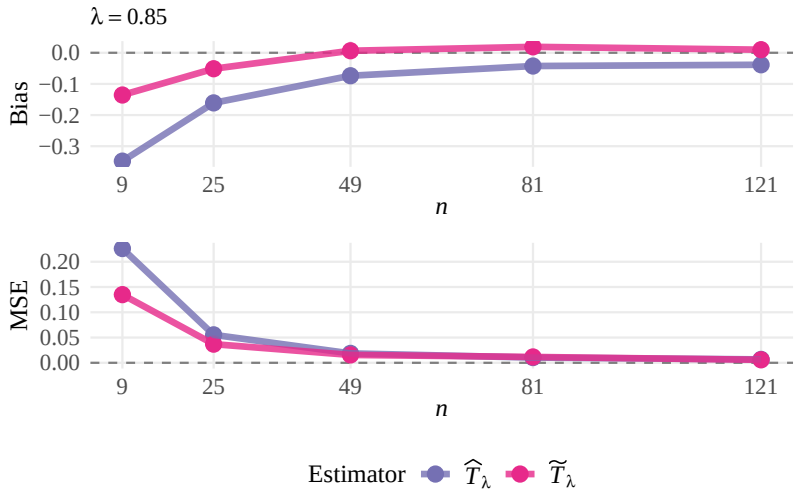

Source: The author (2025)

In particular, at $n = 49$, both estimators exhibit low bias and MSE, confirming their robustness in moderate sample regimes and supporting their use in practical applications.

From this point forward, all subsequent simulations and comparisons will be based on the improved bootstrap estimators: $\widetilde{H}_{\mathsf{AO}}$ for Shannon, $\widetilde{R}_\lambda$ for Rényi, and $\widetilde{T}_\lambda$ for Tsallis entropy.

3.3 HYPOTHESIS TESTING

We aim to determine whether a local region in a SAR intensity image is statistically homogeneous or heterogeneous. This is done by comparing a nonparametric entropy estimator $\widetilde{\theta}$ computed from the observed data to the theoretical entropy $\theta(\Gamma_{\mathsf{SAR}})$ expected under the assumption of fully developed speckle.

Formally, the hypothesis test is:

$$\begin{cases} \mathcal{H}_0 : \mathbb{E}[\widetilde{\theta}] = \theta(\Gamma_{\mathsf{SAR}}) & \text{(homogeneous region)}, \\ \mathcal{H}_1 : \mathbb{E}[\widetilde{\theta}] = \theta(\mathcal{G}_I^0) & \text{(heterogeneous region)}, \end{cases} \tag{3.5}$$

where θ denotes a generic entropy function (Shannon entropy H, Rényi entropy R_λ, or Tsallis entropy T_λ), and $\widetilde{\theta}$ is the corresponding nonparametric estimator ($\widetilde{H}_{\mathsf{AO}}$, $\widetilde{R}_\lambda$ and $\widetilde{T}_\lambda$).

This formulation allows us to construct specific test statistics for each entropy measure. The null hypothesis $\mathcal{H}_0$ assumes that the data follow the Gamma distribution (homogeneous texture), while the alternative $\mathcal{H}_1$ considers the presence of texture modeled by the $\mathcal{G}_I^0$ distribution.

As in the parametric setting it is not possible to define the null hypothesis as $\mathcal{H}_0\colon \alpha = -\infty$, classical inference techniques such as the likelihood ratio, score, gradient, or Wald tests cannot be applied. To address this, we construct non-parametric entropy-based test statistics as described below.

3.3.1 The Proposed Test Based on Shannon Entropy

Given a random sample $\boldsymbol{Z} = (Z_1, Z_2, \ldots, Z_n)$ from a distribution $\mathcal{D}$, we define a test statistic based on the difference between a non-parametric estimator of Shannon entropy, $\widetilde{H}_{\mathsf{AO}}(\boldsymbol{Z})$, and the analytical Shannon entropy of the Gamma SAR model (Γ_{SAR}) in (2.8), which depends on the known number of looks $L \geq 1$ and the sample mean $\widehat{\mu}$.

The test statistic is given by:

$$S_{\widetilde{H}_{\mathsf{AO}}}(\boldsymbol{Z}; L) = \widetilde{H}_{\mathsf{AO}} - \Big\{L - \ln L + \ln\Gamma(L) + (1-L)\psi^{(0)}(L) + \ln\widehat{\mu}\Big\}, \tag{3.6}$$

where $\widehat{\mu} = \frac{1}{n}\sum_{i=1}^{n} Z_i$ is the sample mean.

This statistic can be interpreted as:

$$S_{\widetilde{H}_{\mathsf{AO}}} = \underbrace{\widetilde{H}_{\mathsf{AO}}}_{\text{estimated}} - \underbrace{H(\Gamma_{\mathsf{SAR}})}_{\text{expected under } \mathcal{H}_0},$$

that is, the discrepancy between the estimated entropy and the theoretical value assuming homogeneity. Values close to zero indicate consistency with the fully developed speckle model, while large positive values suggest higher entropy and therefore, heterogeneity.

3.3.2 The Proposed Test Based on Rényi Entropy

To assess deviations from homogeneity in SAR data, we define a test statistic based on Rényi entropy. The statistic contrasts the non-parametric estimator $\widetilde{R}_{\lambda}(\boldsymbol{Z})$ with the theoretical Rényi entropy of the Γ_{SAR} model in (2.12), assuming that the number of looks $L \geq 1$ is known. The proposed statistic is defined as:

$$S_{\widetilde{R}_{\lambda}}(\boldsymbol{Z}; L) = \widetilde{R}_{\lambda} - \left\{\ln\widehat{\mu} - \ln L + \frac{1}{1-\lambda}\left[-\lambda\ln\Gamma(L) + \ln\Gamma\big(\lambda(L-1)+1\big) - \big(\lambda(L-1)+1\big)\ln\lambda\right]\right\}, \tag{3.7}$$

where $\widehat{\mu} = \frac{1}{n}\sum_{i=1}^{n} Z_i$ is the sample mean.

This test statistic measures the discrepancy between the empirical entropy and the value expected under the fully developed speckle assumption and can be interpreted as:

$$S_{\widetilde{R}_\lambda} = \underbrace{\widetilde{R}_\lambda}_{\text{estimated}} - \underbrace{R_\lambda(\Gamma_{\mathsf{SAR}})}_{\text{expected under } \mathcal{H}_0},$$

the difference between the estimated entropy and the expected value under homogeneity. Values of $S_{\widetilde{R}_\lambda}$ near zero suggest that the observed region is statistically homogeneous, while large deviations indicate the presence of texture or roughness.

3.3.3 The Proposed Test Based on Tsallis Entropy

To evaluate heterogeneity in SAR imagery, we define a test statistic using Tsallis entropy. This statistic contrasts the non-parametric estimator $\widetilde{T}_\lambda(\boldsymbol{Z})$ with the analytical Tsallis entropy under the Γ_{SAR} model, as derived in Equation (2.19). We assume the number of looks $L \geq 1$ is known and use the following formulation:

$$S_{\widetilde{T}_\lambda}(\boldsymbol{Z}; L) = \widetilde{T}_\lambda - \left\{ \frac{1}{\lambda - 1} \Big[1 - \exp\Big((1-\lambda)\ln\widehat{\mu} + (\lambda-1)\ln L + \ln\Gamma\Big(\lambda(L-1)+1\Big) - \lambda\ln\Gamma(L) - \Big(\lambda(L-1)+1\Big)\ln\lambda \Big) \Big] \right\}, \quad (3.8)$$

where $\widehat{\mu} = \frac{1}{n}\sum_{i=1}^{n} Z_i$ is the sample mean.

As in the previous cases, this test statistic measures the difference between the empirical entropy and its theoretical counterpart under the assumption of fully developed speckle:

$$S_{\widetilde{T}_\lambda} = \underbrace{\widetilde{T}_\lambda}_{\text{estimated}} - \underbrace{T_\lambda(\Gamma_{\mathsf{SAR}})}_{\text{expected under } \mathcal{H}_0}.$$

Values of $S_{\widetilde{T}_\lambda}$ close to zero indicate that the observed region aligns with the homogeneous model. In contrast, significantly positive values suggest the presence of structural variations or texture, signaling statistical heterogeneity in the scene.

An important advantage shared by all three proposed test statistics ((3.6), (3.7) and (3.8)) is that they avoid the need to estimate parameters from the alternative $\mathcal{G}_I^0$ distribution, such as the roughness parameter α. This leads to a simpler, more interpretable, and statistically grounded testing procedure.

Additionally, the tests are computationally efficient and suitable for practical applications,

including large-scale image processing. This robustness is especially evident in small sample sizes, where bootstrap correction improves the reliability of the entropy estimates and stabilizes the resulting p-values used for decision-making.

3.3.4 Empirical Behaviour of the Three Statistics

Figures 11-13 display the empirical distributions of the three entropy-based statistics:Shannon $S_{\widetilde{H}}(\mathbf{Z}; L)$, Rényi $S_{\widetilde{R}_\lambda}(\mathbf{Z}; L)$ (with $\lambda = 0.9$) and Tsallis $S_{\widetilde{T}_\lambda}(\mathbf{Z}; L)$ ($\lambda = 0.85$) obtained from 10^4 Monte Carlo replications of Γ_{SAR} data for window sizes $n \in \{49, 81, 121\}$ and looks $L \in \{5, 18\}$.

All three empirical densities are tightly concentrated around zero, confirming that under $\mathcal{H}_0$ the test statistic has mean approximately 0; at the same time, their moderately heavy tails reveal sensitivity to departures from homogeneity, which is desirable for detecting subtle texture.

Figure 11 – Empirical densities of $S_{\widetilde{H}_{AO}}(\boldsymbol{Z}; L)$ under $\mathcal{H}_0$.

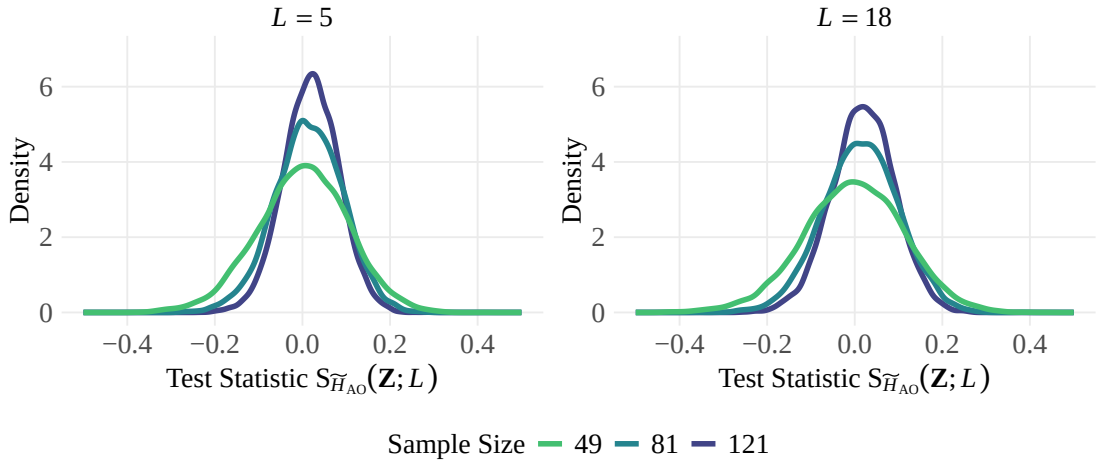

Source: The author (2025)

Figure 12 – Empirical densities of $S_{\widetilde{R}_\lambda}(\boldsymbol{Z}; L)$ under $\mathcal{H}_0$, with $\lambda = 0.9$.

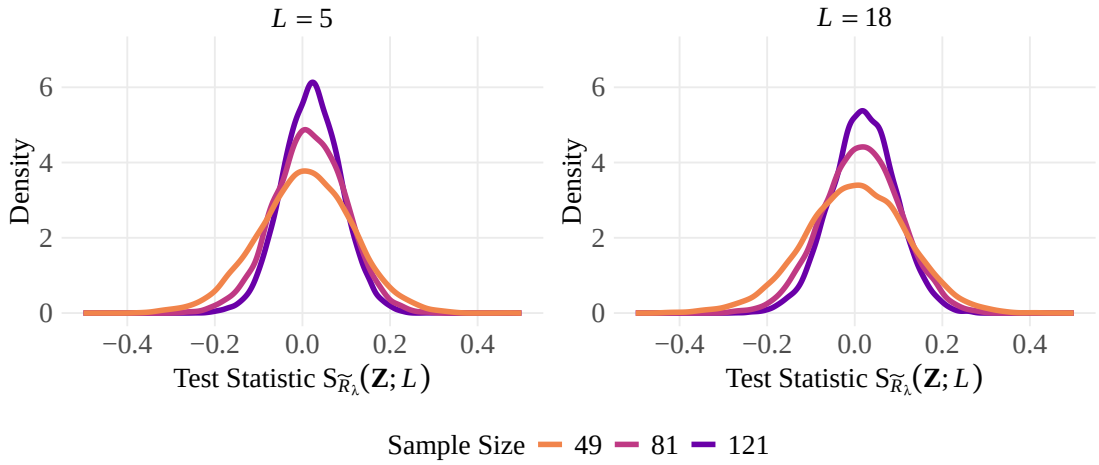

Source: The author (2025)

Figure 13 – Empirical densities of $S_{\widetilde{T}_\lambda}(\boldsymbol{Z}; L)$ under $\mathcal{H}_0$, with $\lambda = 0.85$.

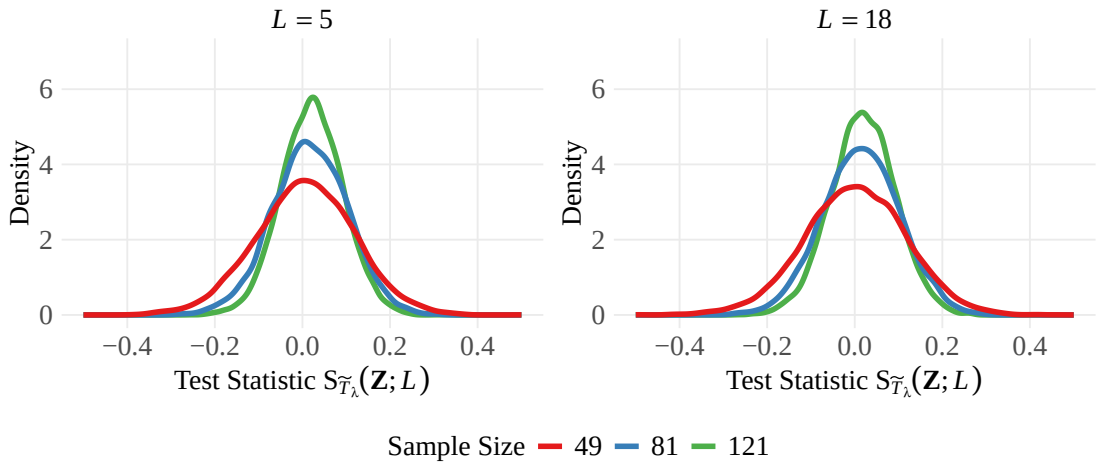

Source: The author (2025)

Under the asymptotic properties of the entropy estimators (VASICEK, 1976; VAN ES, 1992), for sufficiently large samples, $S_{\widetilde{\theta}}(\boldsymbol{Z}; L)$ follows an asymptotic normal distribution:

$$S_{\widetilde{\theta}}(\mathbf{Z}; L) \xrightarrow[n\to\infty]{\mathcal{D}} \mathcal{N}\left(\mu_S, \sigma_S^2\right),$$

where $\widetilde{\theta} \in \{\widetilde{H},\ \widetilde{R}_\lambda,\ \widetilde{T}_\lambda\}$ and $\xrightarrow{\mathcal{D}}$ denotes convergence in distribution.

Here, $\mu_S = \mathbb{E}[S_{\widetilde{\theta}}(\boldsymbol{Z}; L)]$ and $\sigma_S^2 = \mathrm{Var}[S_{\widetilde{\theta}}(\boldsymbol{Z}; L)]$ are the theoretical mean and variance of the test statistic under $\mathcal{H}_0$. This asymptotic normality can be explained by noting that the entropy estimator (and hence $S_{\widetilde{\theta}}$) can be expressed as a sum or average of numerous

observations; therefore, by the Central Limit Theorem and the delta method, its sampling distribution approaches a Gaussian form for large n.

In practice, we estimate $\widehat{\mu}_S$ and $\widehat{\sigma}_S$ via Monte Carlo under $\mathcal{H}_0$.

$$\varepsilon = \frac{S_{\widetilde{\theta}}(\boldsymbol{Z}; L) - \widehat{\mu}_S}{\widehat{\sigma}_S},$$

which is asymptotically standard normal distributed for large n. Consequently, two-sided p-values are obtained as $2\Phi(-|\varepsilon|)$, where $\Phi(\cdot)$ is the cumulative distribution function of the standard normal distribution.

Because all three test statistics share the same asymptotic distribution, the practical procedure is identical. First, the test statistic $S_{\widetilde{\theta}}(\boldsymbol{Z}; L)$ is computed for the observed data. Then, it is standardized using the estimated mean and standard deviation $(\widehat{\mu}_S, \widehat{\sigma}_S)$. Finally, the p-value is computed as $2\Phi(-|\varepsilon|)$. As shown in Figure 14.

Figure 14 – Workflow of the entropy-based hypothesis test: calculate test statistic, standardize, derive p-value, and make a decision by threshold 0.05.

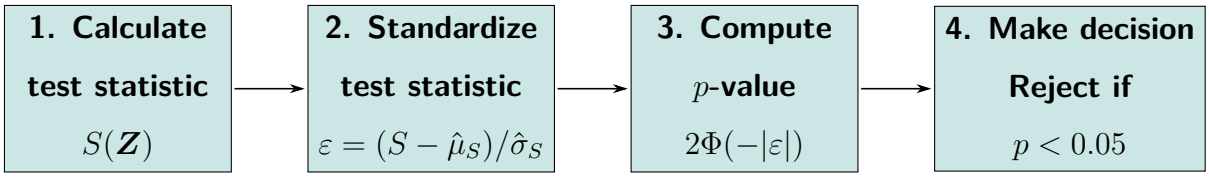

Source: The author (2025)

Importantly, no parameters from the alternative $\mathcal{G}_I^0$ model are needed, which simplifies implementation and avoids complex estimation procedures.

3.3.5 Size and Power Analysis of the Proposed Tests

The statistical validity and effectiveness of the proposed tests based on Shannon, Rényi, and Tsallis entropies were assessed through the analysis of two key properties: *size* and *power*. These properties provide insight into the probability of making incorrect decisions during hypothesis testing.

The size of a statistical test, also known as the Type I error rate, refers to the probability of incorrectly rejecting the null hypothesis $\mathcal{H}_0$ when it is in fact true. In hypothesis testing, practitioners typically specify a nominal significance level, commonly set at $1\,\%$, $5\,\%$, and $10\,\%$.

These values define the acceptable probability of committing a Type I error. A well-calibrated test should exhibit empirical Type I error rates that closely match the nominal levels across different sample sizes and conditions.

To evaluate this, we performed a Monte Carlo simulation with 1000 replications for each combination of sample size and number of looks L, under the null hypothesis $\mathcal{H}_0$, where the data follow a Γ_{SAR} distribution with mean $\mu = 1$. For each replication, the corresponding test statistic was computed using a bootstrap-based entropy estimator with $B = 100$ resamples. In the case of the Rényi and Tsallis entropy-based tests, we used order parameters $\lambda = 0.9$ and $\lambda = 0.85$, respectively. The empirical size was then estimated as the proportion of replications in which the null hypothesis was incorrectly rejected.

The observed Type I error rates for the three entropy-based tests were consistently close to the nominal levels (0.01, 0.05, 0.10), thereby confirming the validity and proper calibration of the procedures. These results are summarized in Tables 3–5, and are visualized in the top panel of Figure 15.

The power of a statistical test is defined as the probability of correctly rejecting the null hypothesis when it is false, that is, when the data are generated under the alternative hypothesis $\mathcal{H}_1$. It is mathematically given by $1 - \beta$, where β represents the Type II error rate (the probability of failing to reject a false null hypothesis). In other words, high power indicates low probability of committing a Type II error, and reflects the test's sensitivity to deviations from $\mathcal{H}_0$.

To assess this property, we simulated data under the alternative hypothesis $\mathcal{H}_1$, assuming the $\mathcal{G}_I^0$ distribution with $\mu = 1$ and $\alpha = -2$. For each combination of sample size and number of looks L, we performed 1000 Monte Carlo replications. In each replication, the corresponding test statistic was computed using a bootstrap-based entropy estimator with $B = 100$ resamples. For the Rényi and Tsallis entropy-based tests, we used order parameters $\lambda = 0.9$ and $\lambda = 0.85$, respectively. Power was estimated as the proportion of replications in which the null hypothesis $\mathcal{H}_0$ was correctly rejected.

As expected, power increased with both the sample size and the number of looks. This trend was consistent across all three entropic measures, demonstrating the effectiveness of the tests in identifying departures from the null hypothesis under heterogeneous conditions. The results are shown in Tables 3–5, with graphical representations provided in the lower panel of Figure 15.

Table 3 – Size and Power of the $S_{\widetilde{H}}(\boldsymbol{Z})$ test statistic (Shannon)

		Size			Power		
$\boldsymbol{L}$	$\boldsymbol{n}$	$1\,\%$	$5\,\%$	$10\,\%$	$1\,\%$	$5\,\%$	$10\,\%$
5	25	0.015	0.056	0.107	0.796	0.924	0.932
	49	0.010	0.051	0.106	0.832	0.963	0.963
	81	0.012	0.058	0.101	0.823	0.964	0.978
	121	0.015	0.062	0.119	0.824	0.955	0.974
8	25	0.013	0.058	0.114	0.981	0.990	0.996
	49	0.008	0.054	0.108	0.994	0.995	0.998
	81	0.013	0.048	0.096	0.991	0.997	0.994
	121	0.015	0.068	0.120	0.991	0.992	0.996
18	25	0.018	0.049	0.121	1.000	0.999	1.000
	49	0.014	0.045	0.098	0.999	0.999	1.000
	81	0.010	0.042	0.103	0.998	1.000	0.999
	121	0.014	0.062	0.107	0.999	0.997	1.000

Source: The author (2025)

Table 4 – Size and Power of the $S_{\widetilde{R}_\lambda}(\boldsymbol{Z})$ test statistic (Rényi)

		Size			Power		
$\boldsymbol{L}$	$\boldsymbol{n}$	$1\,\%$	$5\,\%$	$10\,\%$	$1\,\%$	$5\,\%$	$10\,\%$
5	25	0.014	0.050	0.100	0.978	0.994	0.993
	49	0.011	0.048	0.109	0.994	1.000	0.999
	81	0.012	0.057	0.103	0.998	0.998	0.999
	121	0.013	0.061	0.116	0.999	0.999	0.997
8	25	0.010	0.051	0.105	0.996	0.999	1.000
	49	0.008	0.056	0.109	1.000	0.999	1.000
	81	0.012	0.052	0.097	0.999	0.999	0.999
	121	0.016	0.070	0.116	0.998	1.000	0.999
18	25	0.016	0.051	0.111	1.000	1.000	1.000
	49	0.014	0.047	0.098	1.000	1.000	1.000
	81	0.013	0.048	0.106	1.000	1.000	1.000
	121	0.012	0.066	0.110	1.000	1.000	1.000

Source: The author (2025)

Table 5 – Size and Power of the $S_{\widetilde{T_\lambda}}(\boldsymbol{Z})$ test statistic (Tsallis)

		Size			Power		
$\boldsymbol{L}$	$\boldsymbol{n}$	$1\,\%$	$5\,\%$	$10\,\%$	$1\,\%$	$5\,\%$	$10\,\%$
5	25	0.014	0.051	0.103	0.958	0.991	0.990
	49	0.011	0.048	0.107	0.990	1.000	0.999
	81	0.012	0.057	0.101	0.997	0.998	0.999
	121	0.014	0.060	0.116	0.999	0.999	0.997
8	25	0.010	0.049	0.108	0.992	1.000	1.000
	49	0.008	0.055	0.108	1.000	0.999	1.000
	81	0.012	0.052	0.097	0.998	1.000	0.999
	121	0.016	0.072	0.116	0.998	1.000	0.999
18	25	0.015	0.052	0.111	1.000	1.000	1.000
	49	0.013	0.046	0.099	1.000	1.000	1.000
	81	0.013	0.047	0.105	1.000	1.000	1.000
	121	0.012	0.065	0.109	1.000	1.000	1.000

Source: The author (2025)

Figure 15 – Comparative performance of test statistics based on Shannon, Rényi and Tsallis entropies. Size and Power for different sample sizes and L values.

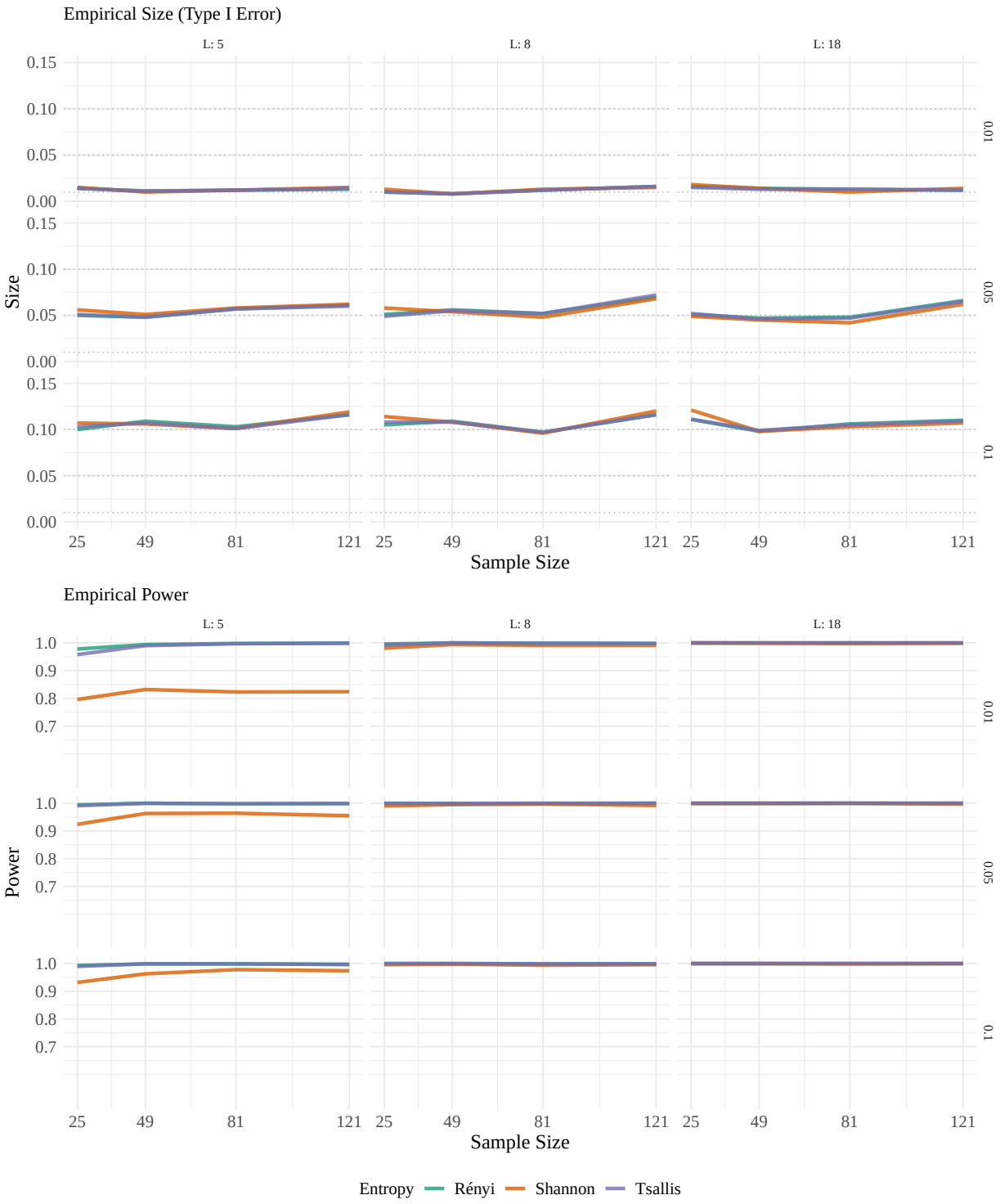

Source: The author (2025)

3.4 FIXED AND ADAPTIVE WINDOWS

This section outlines the two local windowing strategies that will be used in the next chapter to evaluate the proposed entropy-based tests on both simulated and real SAR intensity data.

3.4.1 Fixed Sliding Windows

The first strategy uses a fixed sliding window of size 7×7 pixels. For each window, the test statistics $S_{\widetilde{H}_{\mathsf{AO}}}$, $S_{\widetilde{R}_\lambda}$, and $S_{\widetilde{T}_\lambda}$ will be computed, and the associated p-values derived. The p-value measures evidence against the null hypothesis of homogeneity (fully developed speckle under the Γ_{SAR} model). High values (e.g., $p > 0.05$) will be interpreted as no significant deviation from homogeneity, whereas low p-values (e.g., $p < 0.05$) will be taken as *evidence of heterogeneity*. These p-values will later be visualized as maps to enable spatial assessment.

3.4.2 Adaptive Windows

The second strategy, used only with the Tsallis-entropy test $S_{\widetilde{T}_\lambda}$, builds on the adaptive windowing algorithm by Park et al. (1999). The analysis window size is adjusted according to the local homogeneity of the scene. For each pixel (i, j), let w_{ij} be the window centered at (i, j) with radius N_{ij}, defined as

$w_{ij} = \{(i', j') \,/\, i - N_{ij} \leq i' \leq i + N_{ij} \,\wedge\, j - N_{ij} \leq j' \leq j + N_{ij}\}$.

The border of this window is given by

$b_{ij} = \{(i', j') \in w_{ij} \,/\, i' = i - N_{ij} \,\vee\, i' = i + N_{ij} \,\vee\, j' = j - N_{ij} \,\vee\, j' = j + N_{ij}\}$.

The coefficient of variation is computed over the border of the current window as $C_{ij} = \frac{\sigma_{ij}}{\mu_{ij}}$, where the mean μ_{ij} and the standard deviation σ_{ij} are calculated using only the border pixels b_{ij} of w_{ij}.

For SAR intensity images (fully developed speckle with L looks), the coefficient of variation in homogeneous areas satisfies

$$C_{ij} \approx \sigma_n := \frac{1}{\sqrt{L}}.$$

The homogeneity criterion is defined by comparing C_{ij} with an adaptive threshold U_{ij}:

$$U_{ij} = \eta \left(1 + \sqrt{\frac{1 + 2\sigma_n^2}{8\,(W_{ij} - 1)}}\right) \sigma_n,$$

where $W_{ij} = 2N_{ij} + 1$ is the current window side length, and η is a tuning parameter controlling the degree of smoothing. Values close to $\eta = 1$ provide limited speckle suppression, while larger values increase smoothing and yield stronger noise reduction.

The window radius N_{ij} is updated dynamically and locally as follows:

$$N_{i,j}^{\text{updated}} = \begin{cases} \min\{N_{ij} + 1,\, N_{\max}\}, & \text{if } C_{ij} \leq U_{ij}, \\ \max\{N_{ij} - 1,\, N_{\min}\}, & \text{if } C_{ij} > U_{ij}, \end{cases}$$

where $N_{\max}$ and $N_{\min}$ denote the maximum and minimum allowed window radius, respectively. Since $W_{ij} = 2N_{ij} + 1$, these bounds on the radius induce the corresponding minimum and maximum window sides $W_{\min} = 2N_{\min} + 1$ and $W_{\max} = 2N_{\max} + 1$. Hence, windows *grow* in homogeneous regions (stabilizing estimates) and *shrink* in heterogeneous areas (preserving edges and avoiding class mixing).

Once the window radius N_{ij} has been determined for pixel (i, j), the corresponding full window is extracted and the proposed test in (3.8) is applied to obtain the local test statistic. This produces two outputs: (i) a map of test statistics over the image, and (ii) a window-size map W_{ij} that records the locally selected window side (larger in homogeneous regions, smaller in heterogeneous ones). For inference, each value of the test statistic is standardized using the empirical mean and standard deviation of the image, and two-sided p-values are then computed.

In the experiments presented in the next chapter, the Tsallis-based test statistic $S_{\widetilde{T}\lambda}$ will be applied to both simulated and real SAR images using adaptive windows with side lengths ranging from 5×5 ($W_{\min} = 5$) to 11×11 ($W_{\max} = 11$), with the smoothing parameter set to $\eta = 3$. For comparison, a fixed 7×7 window configuration will also be evaluated.

4 RESULTS

4.1 ANALYSIS WITH SIMULATED DATA

Figure 16a presents the structural design of the synthetic phantom with dimensions of 500×500 pixels, proposed by Gomez et al. (2017) as a tool to assess the performance of speckle-reduction filters. This layout serves as a base template to generate the simulated images shown in Figures 16b–16c. Each region is filled with data simulated from the $\mathcal{G}_I^0$ distribution (2.5), using different combinations of the roughness parameter α and the mean μ, as indicated by the labels in each quadrant of the image. Light regions correspond to textured observations (heterogeneous), while darker regions represent textureless areas (homogeneous).

Figure 16 – Synthetic dataset.

(a) Phantom.

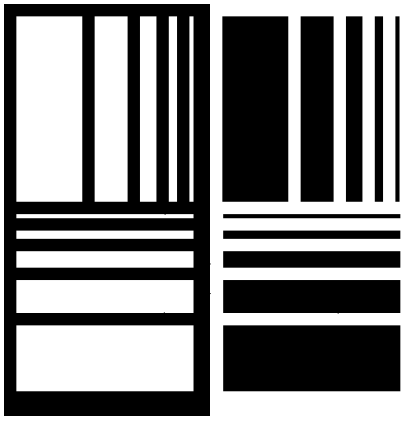

(b) Simulated image, varying α and μ, with $L = 5$.

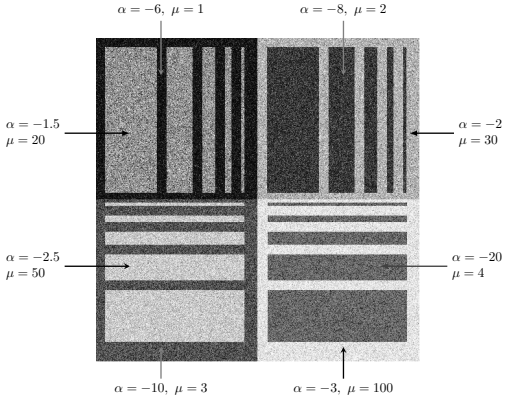

(c) Simulated image, varying α and μ, with $L = 9$.

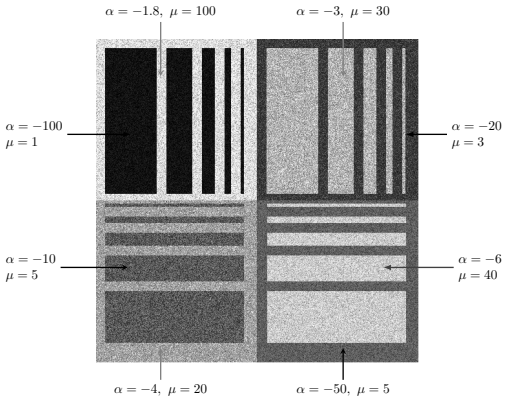

Source: The author (2025)

The first simulated image uses $L = 5$, and the second uses $L = 9$, to evaluate how the test statistics behave as the number of looks increases and speckle noise is reduced.

The α parameter of the $\mathcal{G}_I^0$ distribution is essential for interpreting texture characteristics. Values near zero greater than -3 suggest extremely textured targets, such as urban zones (FRERY; GAMBINI, 2019). As the value decreases, it indicates regions with moderate texture (in the $[-6, -3]$ region), related to forest zones, while values below -6 correspond to textureless regions, such as pasture, agricultural fields, and water bodies (NETO; RODRIGUES, 2023).

We evaluated the three test statistics $S_{\widetilde{H}_{\mathsf{AO}}}$, $S_{\widetilde{R}_\lambda}$, and $S_{\widetilde{T}_\lambda}$ on simulated images using fixed sliding windows of size 7×7 and, for Tsallis only, the adaptive windowing strategy with side lengths from 5×5 ($W_{\min} = 5$) to 11×11 ($W_{\max} = 11$) and smoothing parameter $\eta = 3$. Figures 17 and 18 present, respectively for $L = 5$ and $L = 9$, the p-value maps (top row) and the corresponding binary decision maps (bottom row).

The p-value maps (Figures 17a–17d and 18a–18d) are shown with a continuous color scale: dark red ($p \approx 0$) indicates strong evidence of heterogeneity, while dark blue ($p \approx 1$) corresponds to homogeneous areas. Intermediate colors follow a smooth progression orange ($p \approx 0.2$–0.4) for transitional textures and yellow–green to cyan ($p \approx 0.4$–0.8) for increasingly near-homogeneous regions.

The binary maps (Figures 17e–17h and 18e–18h) simplify these results using a threshold of 0.05. Pixels with p-values below this threshold are shown in black, indicating statistically significant deviations and, therefore, heterogeneity. In contrast, pixels with $p \geq 0.05$ are displayed in white, showing no evidence to reject the null hypothesis of homogeneity.

When the number of looks increases to $L = 9$ (Figure 18), the maps become cleaner due to reduced speckle. All tests successfully detect areas with different texture levels, although some differences remain. The Rényi-based statistic $S_{\widetilde{R}_\lambda}$ is more sensitive to texture variations, highlighting fine patterns of heterogeneity, while the Tsallis-based $S_{\widetilde{T}_\lambda}$ produces cleaner results in uniform areas by reducing false detections. This behavior reflects their formulations: Rényi entropy emphasizes variability, whereas Tsallis entropy is more robust to noise, helping to preserve homogeneous regions.

The adaptive Tsallis version further improves visual quality, larger windows in homogeneous areas yield smoother estimates, and smaller windows in heterogeneous regions enhance detail preservation.

Figure 17 – Results on simulated data ($L = 5$) using $S_{\widetilde{H}_{\mathrm{AO}}}$, $S_{\widetilde{R}_\lambda}$, and $S_{\widetilde{T}_\lambda}$. (a-c) p-value maps with a fixed 7×7 window. (d) p-value map with adaptive windows ($W_{\min} = 5$, $W_{\max} = 11$) for $\eta = 3.0$. (e-h) Binary decision maps at 0.05 significance level.

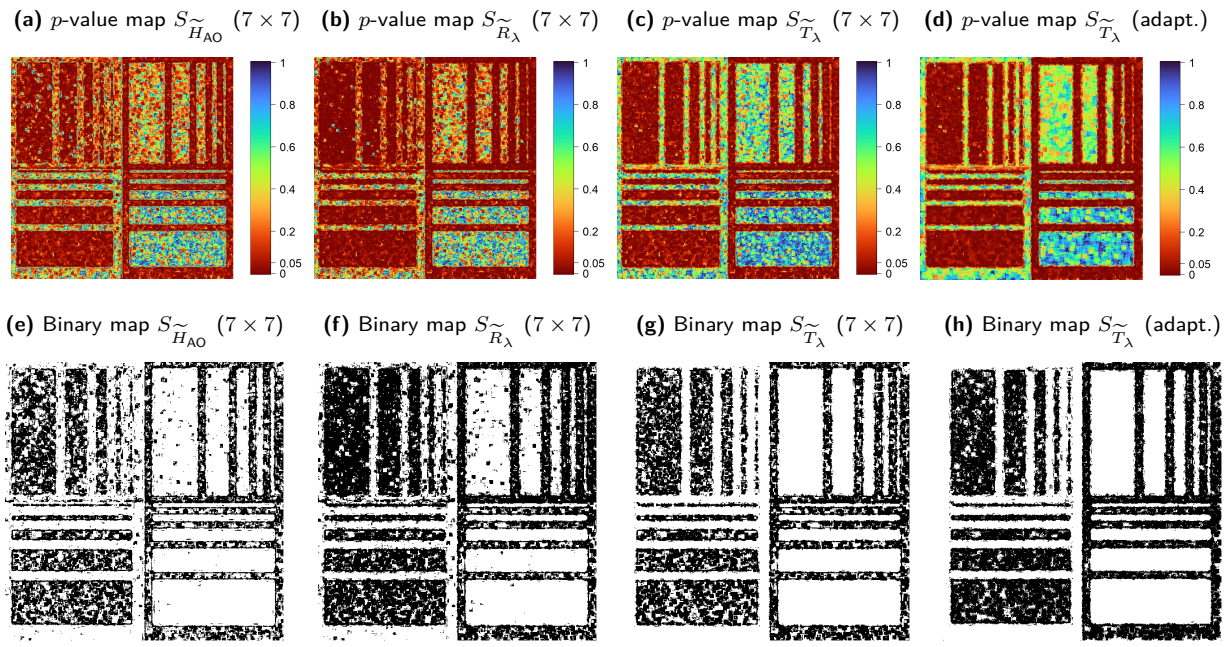

Source: The author (2025)

Figure 18 – Results on simulated data ($L = 9$) using $S_{\widetilde{H}_{\mathrm{AO}}}$, $S_{\widetilde{R}_\lambda}$, and $S_{\widetilde{T}_\lambda}$. (a-c) p-value maps with a fixed 7×7 window. (d) p-value map with adaptive windows ($W_{\min} = 5$, $W_{\max} = 11$) for $\eta = 3.0$. (e-h) Binary decision maps at 0.05 significance level.

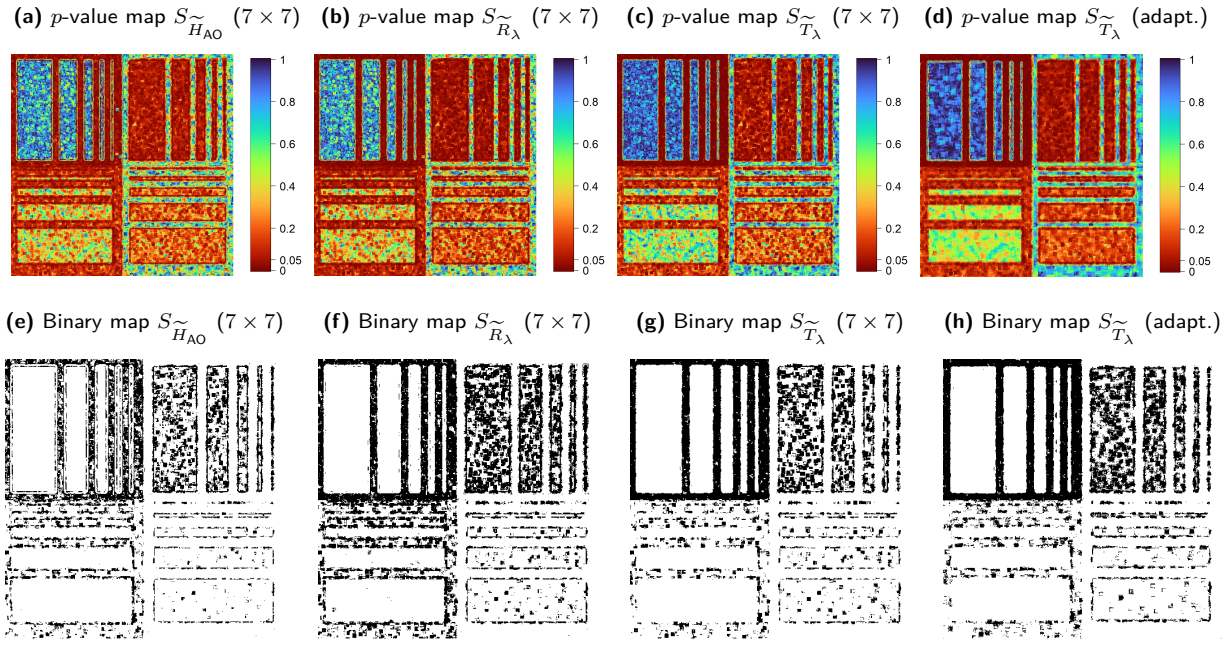

Source: The author (2025)

4.2 APPLICATIONS TO SAR DATA

4.2.1 SAR Dataset and Preprocessing

We evaluated the proposed test statistics using a set of five SAR images acquired from different radar missions. These images cover diverse locations: the surroundings of London (United Kingdom), the outskirts of Munich, the city of New Orleans (USA), Dublin Port (Ireland), and the coast of Jalisco (Mexico), as shown in Figures 19a–23a. The selected scenes include a variety of land types, such as urban areas, mountainous regions, agricultural zones, and water bodies. This diversity allows us to assess the performance of the proposed statistical tests under different texture conditions.

To facilitate interpretation, we also included the corresponding optical images (Figures 19b–23b) obtained from Sentinel-2 Level-2A products. These optical scenes were acquired on dates close to those of the SAR acquisitions to ensure visual consistency. The optical data were downloaded from the Copernicus Data Space platform[1].

The SAR images come from TanDEM-X (X-band), UAVSAR (L-band), and Sentinel-1B (C-band). The two UAVSAR images were obtained from the Alaska Satellite Facility (ASF)[2], which provides airborne and satellite SAR data. The X-band images were downloaded from ESA's Third Party Missions (ESA TPM)[3], and the C-band image from Copernicus Data Space. All images use single polarization (HH or VV), and their acquisition settings differ in resolution, scene size, and number of looks. Table 6 lists the main characteristics of each SAR image.

Table 6 – Parameters of selected SAR images

Site	Mission	Band	Polarization	Size (pixels)	L	Resolution [m]	Acquisition Date
London	TanDEM-X	X	HH	2000×2000	1	$0.99/0.99$	12-11-2021
Munich	UAVSAR	L	HH	1024×1024	12	$4.9/7.2$	16-04-2015
New Orleans	UAVSAR	L	HH	1400×1400	12	$4.9/7.2$	13-03-2016
Dublin	TanDEM-X	X	HH	1100×1100	16	$1.35/1.35$	03-09-2017
Coast of Jalisco	Sentinel-1B	C	VV	512×512	18	$40/40$	29-08-2021

Source: The author (2025)

[1] https://dataspace.copernicus.eu/
[2] https://search.asf.alaska.edu/
[3] https://tpm-ds.eo.esa.int/collections/

For each SAR image, the number of looks L was obtained from the product of azimuth and range looks provided in the metadata of SNAP. We validated this nominal value with the equivalent number of looks (ENL) from manually selected homogeneous areas using the classical formula ENL $= 1/\widehat{\mathrm{CV}}^2$, based on the sample coefficient of variation. The results were consistent with the metadata. We also verified that moderate deviations in L did not significantly impact the outcome of the test, confirming the robustness of the proposed method.

The SAR images were preprocessed using the SNAP (Sentinel Application Platform) toolbox. The standard steps included terrain correction and multilooking (when necessary) to produce intensity images. UAVSAR scenes were also reprojected to align them with standard geographic coordinates. Finally, the resulting images were exported in ENVI format and used as input for statistical analysis in `R`, where the proposed tests were applied.

4.2.2 Qualitative Inspection

We applied the three bootstrap statistics, $S_{\widetilde{H}_{\mathsf{AO}}}$, $S_{\widetilde{R}_\lambda}$, and $S_{\widetilde{T}_\lambda}$, to the five SAR intensity images in Figures 19a–23a. The fixed approach uses local sliding windows of size 7×7. The adaptive approach (used with Tsallis) varies the window side from 5×5 ($W_{\min} = 5$) to 11×11 ($W_{\max} = 11$), with smoothing parameter $\eta = 3$, and $B = 100$ bootstrap replications per window. Each figure is organized in three rows: (i) SAR scene and a matching Sentinel-2 optical image, (ii) p-value maps for the three tests, and (iii) binary maps at the 5% level (black $=$ heterogeneous, white $=$ homogeneous).

Across all scenes, the three tests detect the main textured elements (urban blocks, port facilities, roads, crop boundaries, mountains, and river banks). In the p-value maps, dark red ($p \approx 0$) concentrates on heterogeneous areas such as urban blocks, harbor structures, and field edges, while blue ($p \approx 1$) dominates open water and other uniform surfaces. Intermediate colors mark transitional textures.

The adaptive Tsallis results are visually better than the fixed windows: in homogeneous regions, the maps look smoother and more stable, while in heterogeneous regions the edges are sharper and fine details are preserved. The binary maps make this clear: the adaptive strategy keeps thin structures (roads, levees, dock lines) that are partly lost with the fixed window.

The number of looks also matters. With fewer looks (stronger speckle), the adaptive scheme improves urban and boundary detection compared with the fixed window. As L

increases, speckle decreases and all methods improve, yet the adaptive maps still show cleaner homogeneous areas and crisper boundaries in textured zones.

Comparing statistics, the Rényi-based $S_{\widetilde{R}_\lambda}$ is more sensitive to texture changes and often highlights fine-scale heterogeneity. The Tsallis-based $S_{\widetilde{T}_\lambda}$ is more conservative in uniform areas, reducing false alarms and producing cleaner homogeneous regions. The adaptive Tsallis variant combines these benefits with data-driven window sizes, which explains its overall better visual quality across the five scenes.

Figure 19 – Detection of heterogeneous areas in a SAR image over London, UK: comparison of test statistics $S_{\widetilde{H}_{\mathsf{AO}}}$, $S_{\widetilde{R}_\lambda}$, and $S_{\widetilde{T}_\lambda}$. Top: (a-b) input images (SAR and optical). Middle: (c-e) p-value maps with a fixed 7×7 window. (f) p-value map with adaptive windows ($W_{\min} = 5$, $W_{\max} = 11$) for $\eta = 3.0$. Bottom: (g-j) Binary decision maps at 0.05 significance level.

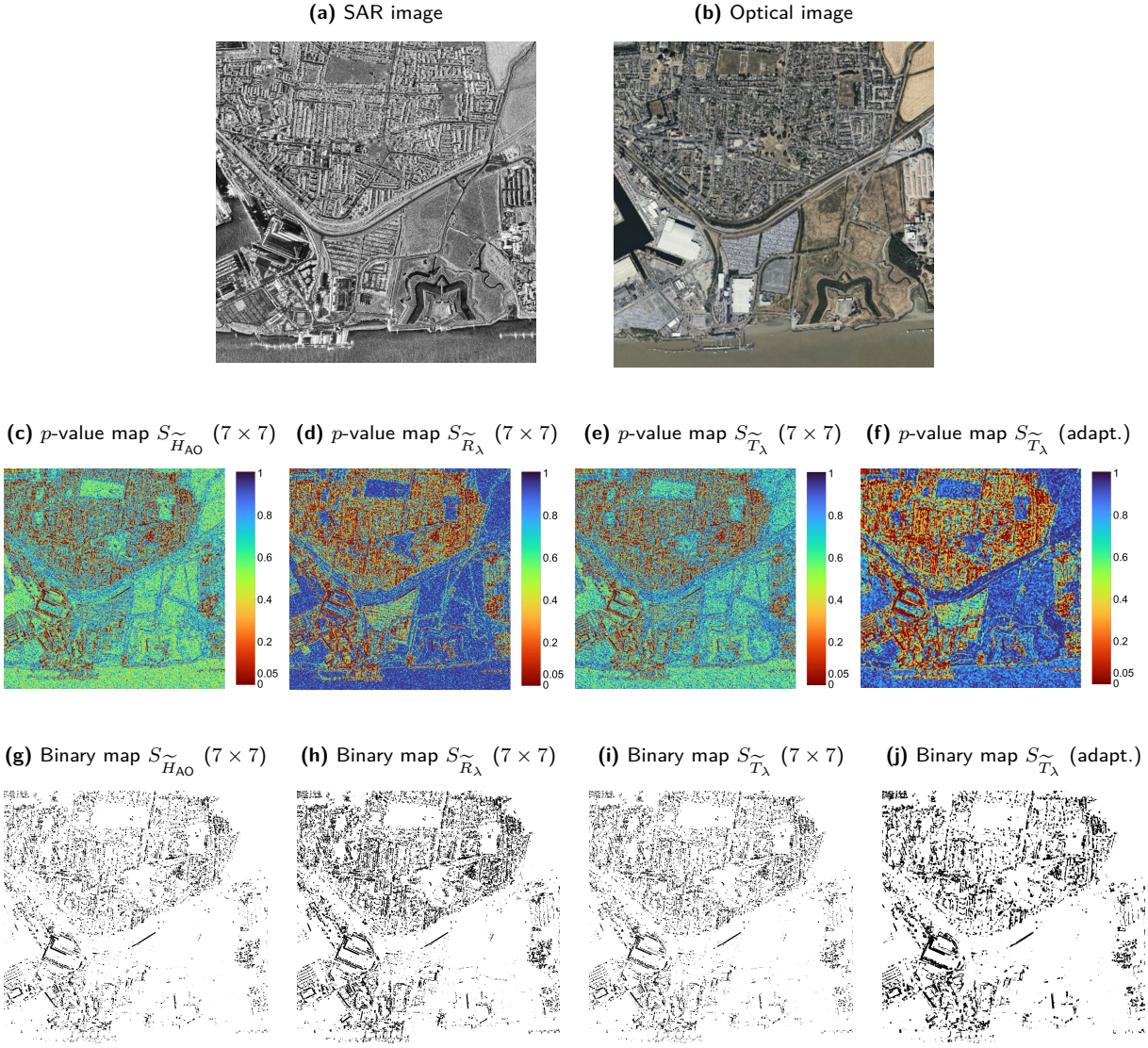

Source: The author (2025)

Figure 20 – Detection of heterogeneous areas in a SAR image over the outskirts of Munich, Germany: comparison of test statistics $S_{\widetilde{H}_{\mathsf{AO}}}$, $S_{\widetilde{R}_\lambda}$, and $S_{\widetilde{T}_\lambda}$. Top: (a-b) input images (SAR and optical). Middle: (c-e) p-value maps with a fixed 7×7 window. (f) p-value map with adaptive windows ($W_{\min} = 5$, $W_{\max} = 11$) for $\eta = 3.0$. Bottom: (g-j) Binary decision maps at 0.05 significance level.

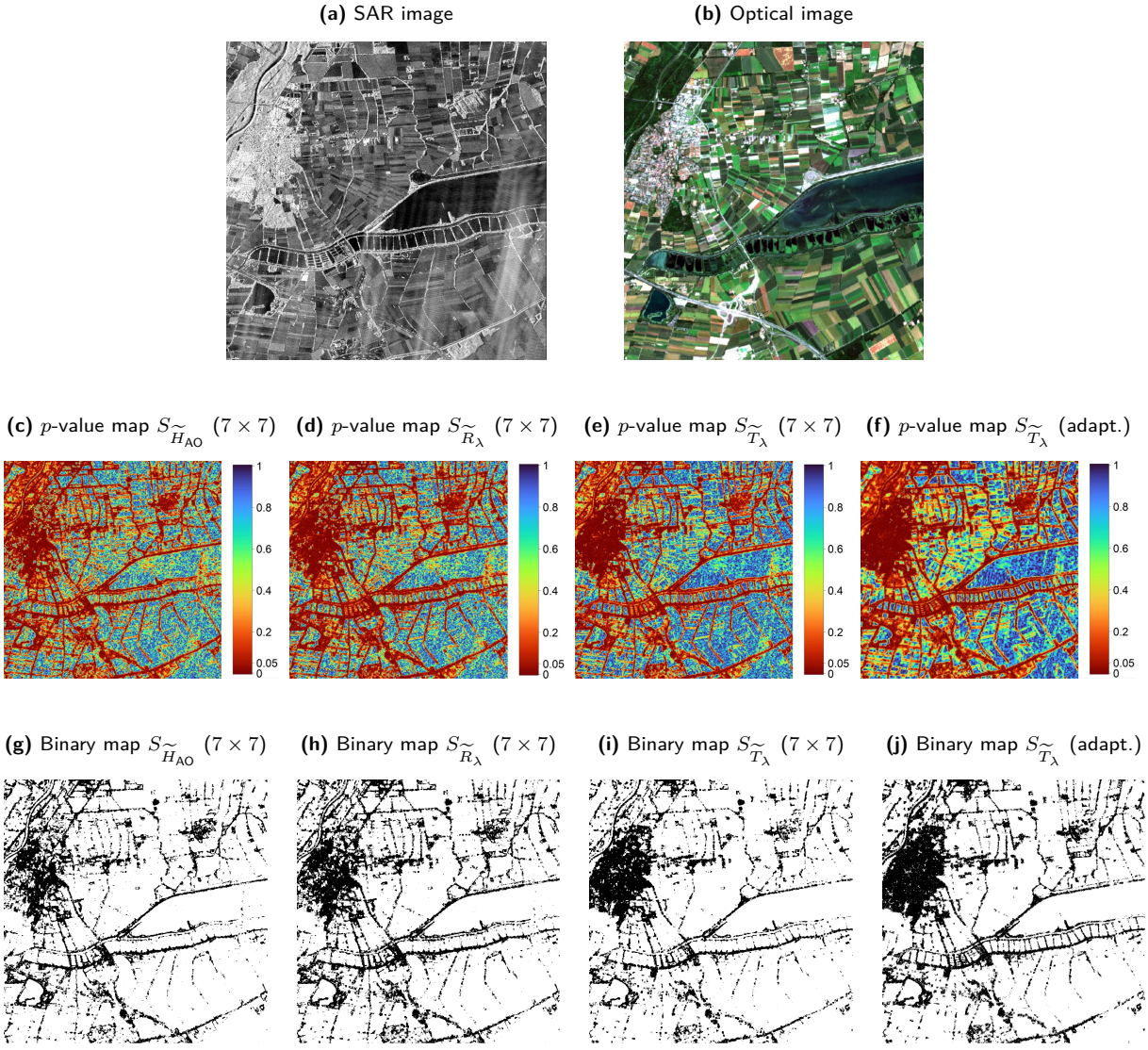

Source: The author (2025)

Figure 21 – Detection of heterogeneous areas in a SAR image over New Orleans city, USA: comparison of test statistics $S_{\widetilde{H}_{\mathsf{AO}}}$, $S_{\widetilde{R}_\lambda}$, and $S_{\widetilde{T}_\lambda}$. Top: (a-b) input images (SAR and optical). Middle: (c-e) p-value maps with a fixed 7×7 window. (f) p-value map with adaptive windows ($W_{\min} = 5$, $W_{\max} = 11$) for $\eta = 3.0$. Bottom: (g-j) Binary decision maps at 0.05 significance level.

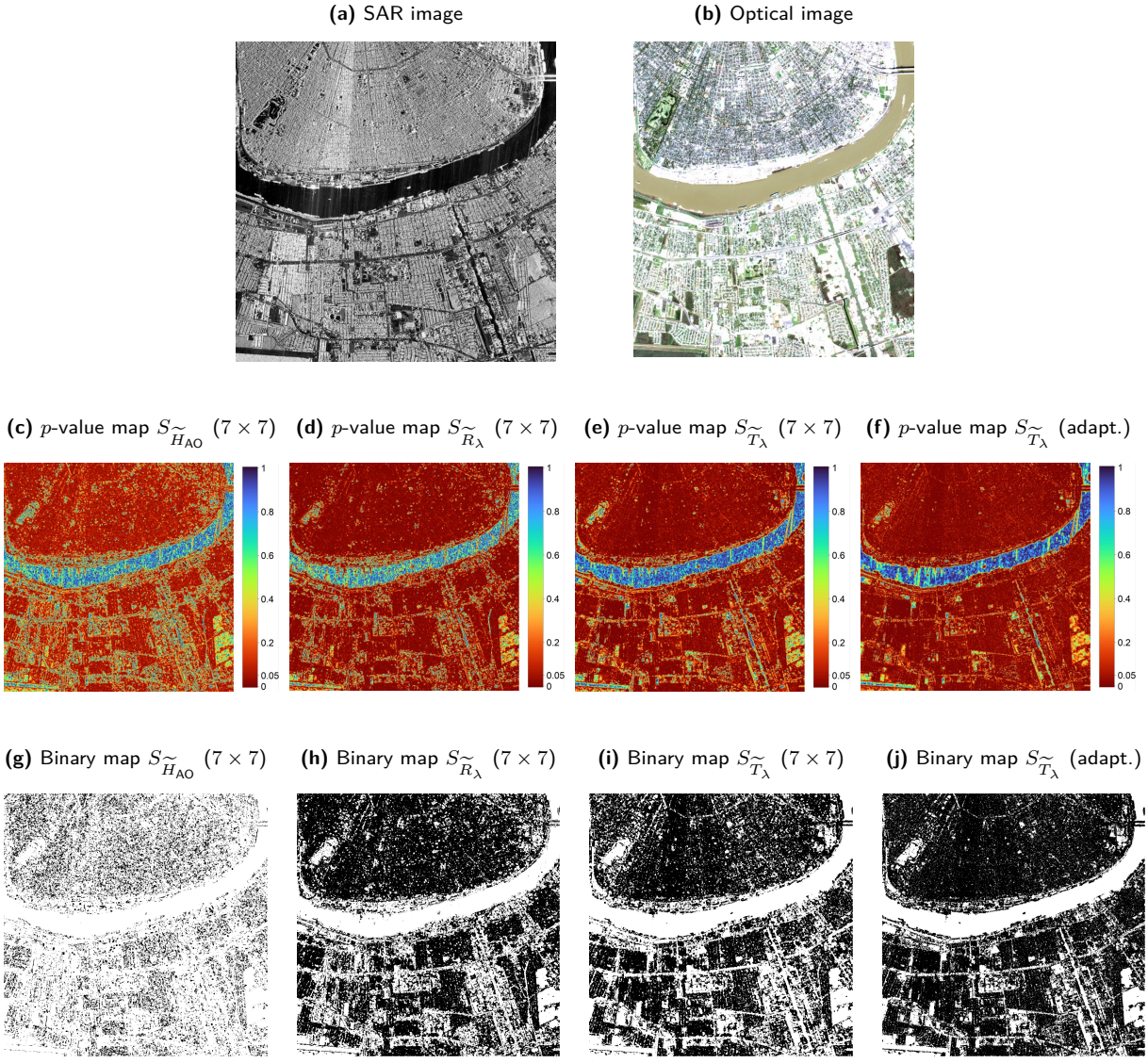

Source: The author (2025)

Figure 22 – Detection of heterogeneous areas in a SAR image over Dublin Port, Ireland: comparison of test statistics $S_{\widetilde{H}_{\mathsf{AO}}}$, $S_{\widetilde{R}_\lambda}$, and $S_{\widetilde{T}_\lambda}$. Top: (a-b) input images (SAR and optical). Middle: (c-e) p-value maps with a fixed 7×7 window. (f) p-value map with adaptive windows ($W_{\min} = 5$, $W_{\max} = 11$) for $\eta = 3.0$. Bottom: (g-j) Binary decision maps at 0.05 significance level.

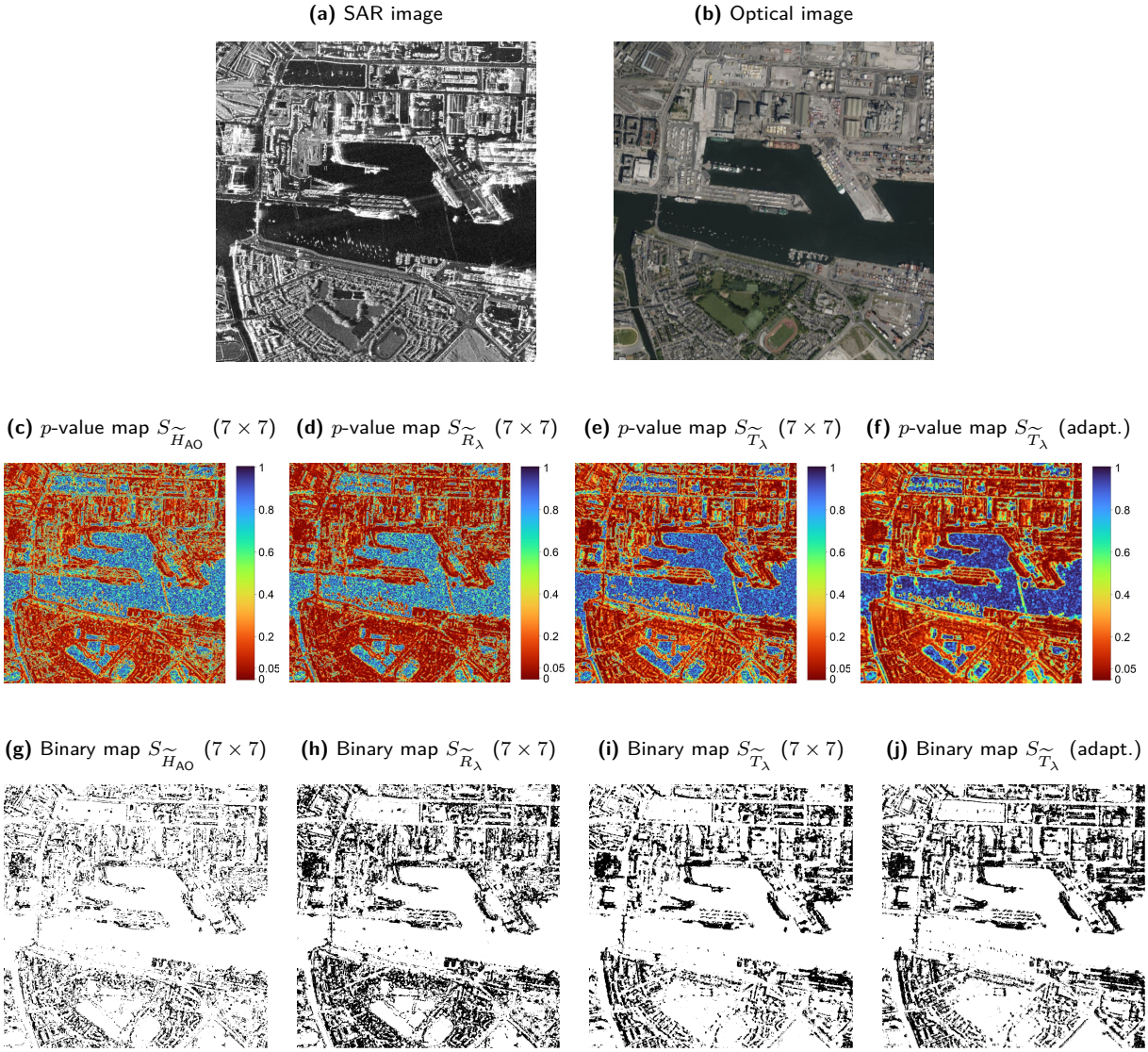

Source: The author (2025)

Figure 23 – Detection of heterogeneous areas in a SAR image over the Coast of Jalisco, Mexico: comparison of test statistics $S_{\widetilde{H}_{\mathsf{AO}}}$, $S_{\widetilde{R}_\lambda}$, and $S_{\widetilde{T}_\lambda}$. Top: (a-b) input images (SAR and optical). Middle: (c-e) p-value maps with a fixed 7×7 window. (f) p-value map with adaptive windows ($W_{\min} = 5$, $W_{\max} = 11$) for $\eta = 3.0$. Bottom: (g-j) Binary decision maps at 0.05 significance level.

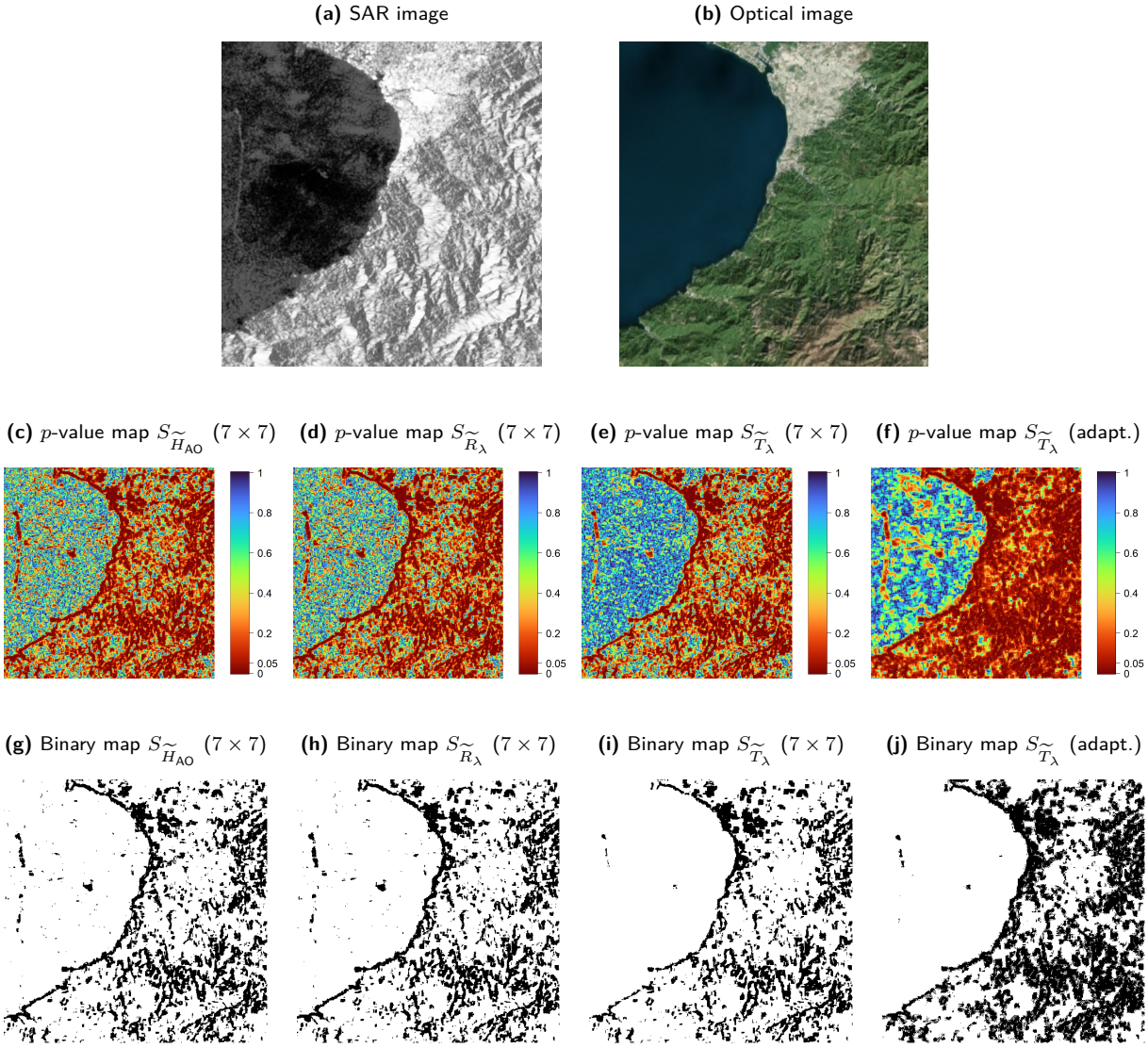

Source: The author (2025)

In addition to the visual analysis presented above, we measured execution times to assess the computational cost of the proposed methods. Table 7 reports the processing times for the three entropy-based tests (Shannon, Rényi, and Tsallis) with fixed 7×7 windows and, for comparison, the adaptive Tsallis variant with window sizes from 5×5 ($W_{\min} = 5$) to 11×11 ($W_{\max} = 11$). Times are reported in minutes and seconds (mm:ss) with $B = 100$ bootstrap replications per window.

Overall, Shannon is the fastest across scenes, which is consistent with its simpler analytical

form. Rényi and Tsallis are slightly slower due to the evaluation of additional terms. As expected, the adaptive Tsallis approach takes the longest because it evaluates multiple window sizes per pixel.

Table 7 – Execution times for the heterogeneity detection using fixed 7×7 and adaptive windows ($W_{\min} = 5$, $W_{\max} = 11$), with $B = 100$ bootstrap replications per scenario. Times are given in minutes and seconds (mm:ss). Rényi entropy uses $\lambda = 0.9$ and Tsallis entropy uses $\lambda = 0.85$

Scene	Shannon	Rényi	Tsallis	Adaptive Tsallis
Image Simulated 1	01:12	01:17	01:25	01:50
Image Simulated 2	01:16	01:27	01:38	02:05
London	12:10	13:28	14:10	16:22
Munich	07:02	8:54	10:02	11:49
New Orleans	10:20	13:39	14:39	15:48
Dublin	8:39	9:44	10:48	12:51
Coast of Jalisco	01:59	02:39	02:54	03:20

Source: The author (2025)

All experiments were executed on the workstation described in Section 1.4, using 8–16 CPU cores. This setup allowed the entropy-based heterogeneity detection tests to process medium-sized SAR scenes within a few minutes, as reported in Table 7.

The total runtime also depends on the number of bootstrap replications (B), since each replication recomputes the test statistic to approximate its sampling distribution under the null hypothesis.

In our simulations, we used $B = 100$, which provides stable and reliable estimates with moderate computational cost. Stable results can already be achieved with $B \geq 50$, whereas larger values of B yield smoother p-value distributions at the expense of longer processing times.

The window size also plays an important role in the heterogeneity detection process. This is particularly evident in the case of the Adaptive Tsallis test, where alternative sliding windows ranging from 5×5 to 11×11 were explored for both simulated and real SAR datasets. Although the observed differences were subtle, the adaptive approach exhibited the expected behavior: larger windows in homogeneous areas produced smoother and more stable estimates, whereas

smaller windows in heterogeneous regions effectively preserved structural details and texture transitions.

For the single-look case ($L = 1$), the adaptive Tsallis test using larger windows yielded more consistent detections, enhancing sensitivity to textural variations without generating excessive false alarms. This confirms that adaptive windowing improves the balance between detection accuracy and spatial smoothness, especially under strong speckle conditions.

Regarding the decision threshold, a significance level of $\alpha = 0.05$ was adopted for the binary classification of the p-value maps. Additional experiments with alternative levels showed the expected trade-offs: a stricter threshold ($\alpha = 0.01$) reduces false alarms but may overlook weak texture variations, while a more relaxed threshold ($\alpha = 0.10$) increases sensitivity to subtle heterogeneity at the expense of a higher false-positive rate, particularly in highly speckled regions. Therefore, $\alpha = 0.05$ represents a balanced and robust choice for most SAR imaging scenarios.

4.2.3 Quantitative Evaluation

Eight polygonal regions of interest (ROIs) were manually selected for each of the three SAR scenes used in the quantitative study—London, Munich, and Dublin (Figures 24a–24c). ROIs labeled in red correspond to heterogeneous areas (class 1) and those in blue to homogeneous areas (class 0). The polygons were rasterized to the image grid to form a partial ground truth. We thresholded the p-value maps at $\alpha = 0.05$, labeling each pixel as heterogeneous (1) or homogeneous (0), and compared the resulting decisions with the ground truth to compute the F1-score (F_1), the Kappa coefficient (κ), and the overall accuracy (OA). Results are summarized in Table 8.

Figure 24 – Selected ROIs for the quantitative evaluation. Red polygons indicate heterogeneous areas (class 1), and blue polygons indicate homogeneous areas (class 0).

(a) London SAR image with selected ROIs.

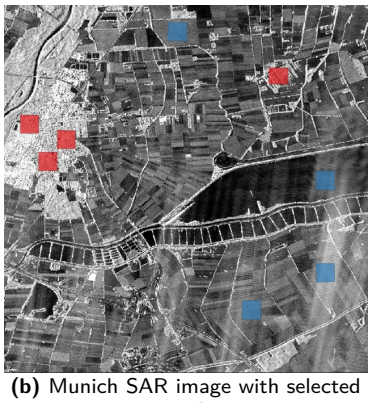

(b) Munich SAR image with selected ROIs.

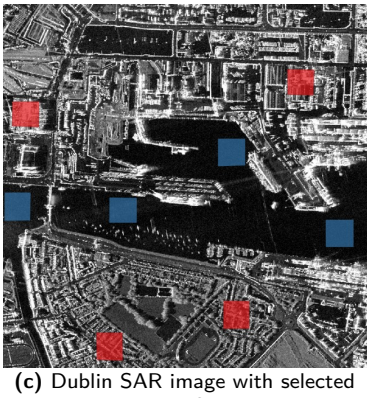

(c) Dublin SAR image with selected ROIs.

Source: The author (2025)

Table 8 – Quantitative measures of heterogeneity detection

Scene	Test	F_1	κ	OA
London	$S_{\widetilde{H}_{\mathrm{AO}}}$	0.617	0.542	0.854
	$S_{\widetilde{R}_\lambda}$	0.695	0.626	0.877
	$S_{\widetilde{T}_\lambda}$	0.603	0.528	0.850
	$S_{\widetilde{T}_\lambda}$ adapt.	**0.757**	**0.697**	**0.897**
Munich	$S_{\widetilde{H}_{\mathrm{AO}}}$	0.883	0.794	0.897
	$S_{\widetilde{R}_\lambda}$	0.924	0.861	0.931
	$S_{\widetilde{T}_\lambda}$	0.930	0.871	0.936
	$S_{\widetilde{T}_\lambda}$ adapt.	**0.935**	**0.880**	**0.940**
Dublin	$S_{\widetilde{H}_{\mathrm{AO}}}$	0.645	0.464	0.858
	$S_{\widetilde{R}_\lambda}$	0.865	0.753	0.875
	$S_{\widetilde{T}_\lambda}$	0.879	0.776	0.887
	$S_{\widetilde{T}_\lambda}$ adapt.	**0.901**	**0.844**	**0.926**

Source: The author (2025)

When comparing the three entropy-based tests, distinct patterns emerge depending on the scene characteristics.

In London, the adaptive Tsallis test achieves the highest scores across metrics ($F_1 = 0.757$, $\kappa = 0.697$, OA $= 0.897$), followed by the Rényi-based statistic ($F_1 = 0.695$, $\kappa = 0.626$, OA $=$ 0.877). Both outperform Shannon ($F_1 = 0.617$, $\kappa = 0.542$, OA $= 0.854$) and fixed-window

Tsallis ($F_1 = 0.603$, $\kappa = 0.528$, OA = 0.850). These results suggest that adaptive windowing is helpful under stronger speckle by smoothing homogeneous areas while preserving edges.

In Munich, all methods perform well, but the adaptive Tsallis variant is slightly superior ($F_1 = 0.935$, $\kappa = 0.880$, OA = 0.940), with fixed Tsallis close behind ($F_1 = 0.930$, $\kappa = 0.871$, OA = 0.936) and Rényi competitive ($F_1 = 0.924$, $\kappa = 0.861$, OA = 0.931). Shannon shows lower but still strong values ($F_1 = 0.883$, $\kappa = 0.794$, OA = 0.897).

In Dublin, the adaptive approach yields the largest gains: adaptive Tsallis leads with $F_1 = 0.901$, $\kappa = 0.844$, and OA = 0.926, followed by fixed Tsallis ($F_1 = 0.879$, $\kappa = 0.776$, OA = 0.887) and Rényi ($F_1 = 0.865$, $\kappa = 0.753$, OA = 0.875). Shannon again records the lowest figures ($F_1 = 0.645$, $\kappa = 0.464$, OA = 0.858).

Overall, the adaptive Tsallis test provides the most accurate classification across the three scenes, with consistent improvements in F_1, κ, and OA. Rényi remains a strong fixed-window alternative, while Shannon is the least effective under the tested conditions. These findings align with the qualitative inspection: adaptive windowing improves the balance between detail preservation in heterogeneous regions and stability in homogeneous areas.

4.3 INTERACTIVE SHINY APP FOR HETEROGENEITY DETECTION

Shiny is an R package (version 1.9.1) developed by RStudio (now Posit) that makes it possible to build interactive web applications directly from R code, without requiring knowledge of HTML, CSS or JavaScript. Users can manipulate inputs (e.g. sliders, file uploads, dropdowns) and see results update instantly in the browser.

To facilitate reproducibility and allow exploration of the heterogeneity-detection pipeline on both simulated and real SAR images, we have developed a Shiny web application.

The app supports three data-loading modes:

- **Simulated image examples**: Choose one of two simulated images (e.g. $L = 5$ or $L = 9$).
- **ENVI sample images**: Select one of three small SAR samples in ENVI format (e.g. Dublin $L = 16$, London $L = 1$, or New Orleans $L = 12$).
- **Upload ENVI**: Upload any custom `.img`/`.hdr` pair to process your own data.

Once the image is loaded, the user can select one of three entropy estimators (Shannon, Rényi, or Tsallis), set the order λ (for Rényi and Tsallis), specify the number of looks L, enable or disable bootstrap resampling (and choose the number of replicates), and fix the sliding-window size $n \times n$. By clicking **Run Detection**, the app performs the sliding-window test and displays the resulting p-value heat-map in color.

Figure 25 – Shiny application interface. The left panel shows the data-loading and parameter controls; the right panel displays the colorized p-value map and elapsed runtime.

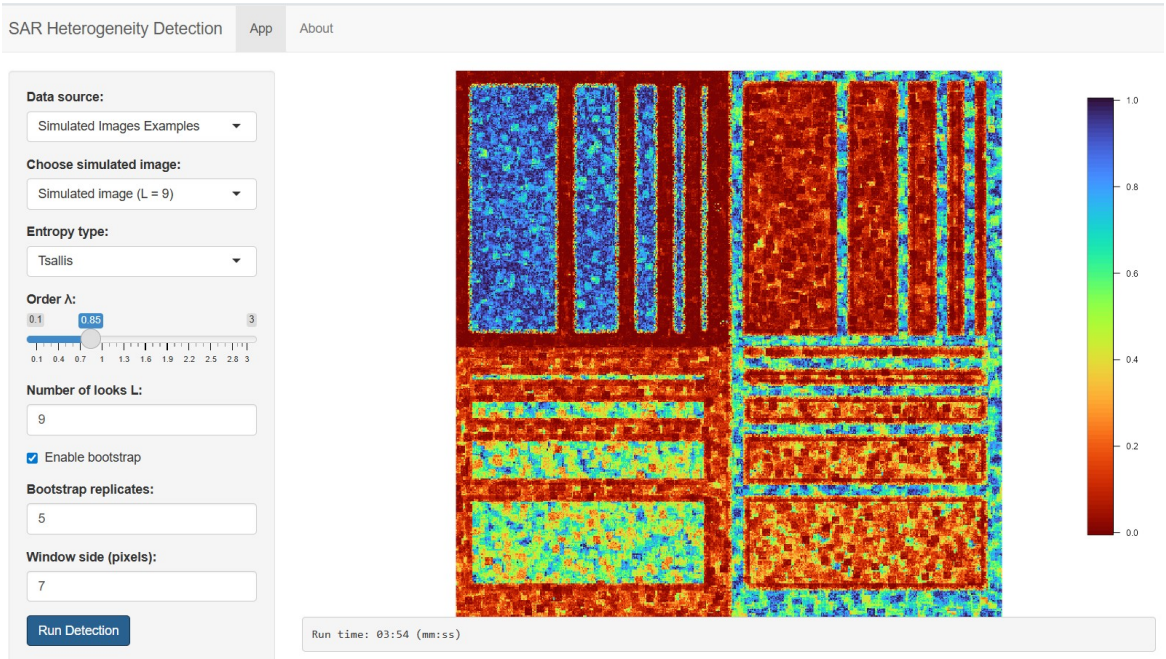

Source: The author (2025)

This interactive tool complements the results presented in Sections 4.1 and 4.2 by enabling real-time parameter tuning and direct comparison across estimators.

The application is publicly accessible at: https://janeth-alpala.shinyapps.io/heterogeneity_detection_app/

5 CONCLUSIONS

This thesis presented a statistical framework for detecting heterogeneity in SAR images, offering both theoretical and practical insights into a fundamental question: How can one effectively distinguish heterogeneous clutter from fully developed speckle, assuming SAR intensity is modeled by the Gamma SAR (Γ_{SAR}) distribution?

To address this, we proposed three novel hypothesis tests based on entropy measures: Shannon, Rényi, and Tsallis entropies. A key theoretical contribution was the derivation of closed-form analytical expressions for the Rényi and Tsallis entropies under both the Γ_{SAR} and $\mathcal{G}_I^0$ distributions, which were previously unavailable in the literature. Using these expressions, we developed bootstrap-based statistical tests corresponding to each entropy measure.

A comprehensive Monte Carlo simulation study was conducted to evaluate the performance of the proposed tests, assessing both their size (Type I error rate) and power (probability of correctly rejecting the null hypothesis under the alternative). The results demonstrated that the methods maintained reliable control over false alarms while significantly improving detection performance as the sample size and number of looks increased.

These theoretical findings were further validated with experiments on both simulated and real SAR data acquired by various radar missions (TanDEM-X, PAZ, ICEYE, UAVSAR, Sentinel-1B), covering a range of resolutions, polarizations, and look numbers. Visual analysis using p-value heatmaps and binary decision maps revealed notable distinctions among the entropy-based tests. In particular, the Rényi-based test exhibited the highest sensitivity in detecting subtle textural variations, effectively identifying heterogeneity even under high-speckle conditions. The Tsallis-based test provided complementary advantages by reliably identifying homogeneous regions, thereby minimizing false alarms (i.e., incorrectly classifying homogeneous areas as heterogeneous). In contrast, the Shannon-based test displayed intermediate performance and lower robustness at low numbers of looks.

Quantitative evaluations using ground truth regions of interest (ROIs) and standard classification metrics further confirmed the superior overall performance of both Rényi and Tsallis-based tests across all tested scenes.

Compared to conventional classification methods, the proposed entropy-based statistical tests offer practical advantages: they provide interpretable, analytical significance measures and require no training data or manual labeling, facilitating rapid analysis suitable for environments

with limited data availability. Typical computations are efficient, generally taking only a few minutes depending on the image size and number of bootstrap replications. Since the three tests share a common computational structure, their execution times are comparable, making the proposed methods particularly attractive for quick screening and exploratory analysis.

Future directions

Future research directions identified from this thesis include integrating the improved bootstrap-based Rényi and Tsallis estimators into broader SAR classification frameworks, both supervised and unsupervised, to expand their applicability beyond heterogeneity detection. This integration could enable the development of multi-level texture classification schemes (e.g., low, moderate, high heterogeneity) that go beyond binary discrimination and provide a more detailed understanding of the scene, without requiring labeled training data.

Additionally, extending the proposed methodology to polarimetric SAR (PolSAR) data represents a promising avenue. One approach could involve analyzing the intensity channels independently and fusing the resulting entropy information using multivariate models. Alternatively, a fully polarimetric analysis could be pursued by testing deviations from the scaled complex Wishart distribution. In this context, exploring the asymptotic behavior of the generalized variance (i.e., the determinant of the covariance matrix) under the complex Wishart model may offer valuable theoretical insights for detecting structural changes in polarimetric data.

REFERENCES

AL-LABADI, L.; CHU, Z.; XU, Y. Advancements in Rényi Entropy and Divergence Estimation for Model Assessment. *Computational Statistics*, 2024.

AL-OMARI, A. I. Estimation of Entropy Using Random Sampling. *Journal of Computational and Applied Mathematics*, v. 261, p. 95–102, 2014.

ALPALA, J.; NASCIMENTO, A. D. C.; FRERY, A. C. Identifying departures from the fully developed speckle hypothesis in intensity SAR data with non-parametric estimation of the entropy. In: 2024 International Conference on Machine Intelligence for GeoAnalytics and Remote Sensing (MIGARS), IEEE, 2024.

ALPALA, J.; NASCIMENTO, A. D. C.; FRERY, A. C. Quantifying Heterogeneity in SAR Imagery with the Rényi Entropy. *IEEE Geoscience and Remote Sensing Letters*, p. 1–1, 2025.

ALPALA, R. J.; BORBA, A. A. De; FRERY, A. C. Quality assessment measures for explainable fusion of statistical evidences of edges in polsar images: A first approach. In: IGARSS 2023 - IEEE international geoscience and remote sensing symposium, IEEE, 2023.

AMITRANO, D. et al. Earth Environmental Monitoring Using Multi-Temporal Synthetic Aperture Radar: A Critical Review of Selected Applications. *Remote Sensing*, v. 13, n. 4, p. 604, 2021.

ARGENTI, F. et al. A Tutorial on Speckle Reduction in Synthetic Aperture Radar Images. *IEEE Geoscience and Remote Sensing Magazine*, v. 1, n. 3, p. 6–35, 2013.

AVVAL, T. G. et al. The Often-Overlooked Power of Summary Statistics in Exploratory Data Analysis: Comparison of Pattern Recognition Entropy (PRE) to Other Summary Statistics and Introduction of Divided Spectrum-PRE (DS-PRE). *Journal of Chemical Information and Modeling*, v. 61, n. 9, p. 4173–4189, 2021.

BARAHA, S.; SAHOO, A. K. Synthetic Aperture Radar Image and Its Despeckling Using Variational Methods: A Review of Recent Trends. *Signal Processing*, v. 212, p. 109156, 2023.

BASHKIROV, A. G. Renyi Entropy as a Statistical Entropy for Complex Systems. *Theoretical and Mathematical Physics*, v. 149, n. 2, p. 1559–1573, 2006.

BAUER, P. C.; LANDESVATTER, C. *Writing a reproducible paper with RStudio and quarto*, 2023.

CAO, S. et al. Ship Detection in Synthetic Aperture Radar Images Under Complex Geographical Environments, Based on Deep Learning and Morphological Networks. *Sensors*, v. 24, n. 13, p. 4290, 2024.

CASSETTI, J. et al. Entropy Estimators in SAR Image Classification. *Entropy*, v. 24, n. 4, p. 509, 2022.

CHAN, D.; GAMBINI, J.; FRERY, A. C. Entropy-Based Non-Local Means Filter for Single-Look SAR Speckle Reduction. *Remote Sensing*, v. 14, n. 3, p. 509, 2022.

CORREA, J. C. A New Estimator of Entropy. *Communications in Statistics-Theory and Methods*, v. 24, n. 10, p. 2439–2449, 1995.

DE A. FERREIRA, J.; NASCIMENTO, A. D. C. Shannon Entropy for the $\mathcal{G}_I^0$ Model: A New Segmentation Approach. *IEEE Journal of Selected Topics in Applied Earth Observations and Remote Sensing*, v. 13, p. 2547–2553, 2020.

EBRAHIMI, N.; PFLUGHOEFT, K.; SOOFI, E. S. Two Measures of Sample Entropy. *Statistics & Probability Letters*, v. 20, n. 3, p. 225–234, 1994.

ESCH, T. et al. Delineation of Urban Footprints from TerraSAR-X Data by Analyzing Speckle Characteristics and Intensity Information. *IEEE Transactions on Geoscience and Remote Sensing*, v. 48, n. 2, p. 905–916, 2010.

FRERY, A. C. et al. A Model for Extremely Heterogeneous Clutter. *IEEE Transactions on Geoscience and Remote Sensing*, v. 35, n. 3, p. 648–659, 1997.

FRERY, A. C.; ALPALA, J.; NASCIMENTO, A. D. C. Identifying Heterogeneity in SAR Data with New Test Statistics. *Remote Sensing*, v. 16, n. 11, p. 1973, 2024.

FRERY, A. C.; CRIBARI-NETO, F.; SOUZA, M. O. Analysis of Minute Features in Speckled Imagery with Maximum Likelihood Estimation. *EURASIP Journal on Advances in Signal Processing*, v. 2004, n. 16, p. 2476–2491, 2004.

FRERY, A. C.; GAMBINI, J. Comparing Samples from the $\mathcal{G}^0$ Distribution Using a Geodesic Distance. *TEST*, v. 29, n. 2, p. 359–378, 2019.

FRERY, A. C.; GOMEZ, L.; MEDEIROS, A. C. A Badging System for Reproducibility and Replicability in Remote Sensing Research. *IEEE Journal of Selected Topics in Applied Earth Observations and Remote Sensing*, v. 13, p. 4988–4995, 2020.

GALLET, M.; MIAN, A.; ATTO, A. Renyi divergences learning for explainable classification of SAR image pairs. In: 2024 IEEE International Conference on Acoustics, Speech and Signal Processing (ICASSP), IEEE, 2024.

GE, P.; GOKON, H.; MEGURO, K. A Review on Synthetic Aperture Radar-Based Building Damage Assessment in Disasters. *Remote Sensing of Environment*, v. 240, p. 111693, 2020.

GOMEZ, L. et al. Fully PolSAR Image Classification Using Machine Learning Techniques and Reaction-Diffusion Systems. *Neurocomputing*, v. 255, p. 52–60, 2017.

HAVRDA, J.; CHARVÁT, F. Quantification Method of Classification Processes. Concept of Structural a-Entropy. *Kybernetika*, v. 03, n. 1, p. (30)–35, 1967.

JIAO, Z. et al. Water Benefit-Based Ecological Index for Urban Ecological Environment Quality Assessments. *IEEE Journal of Selected Topics in Applied Earth Observations and Remote Sensing*, v. 14, p. 7557–7569, 2021.

LIU, C. et al. Research Advances of SAR Remote Sensing for Agriculture Applications: A Review. *Journal of Integrative Agriculture*, v. 18, n. 3, p. 506–525, 2019.

LOPEZ-LOPEZ, L. et al. On the Detection and Long-Term Path Visualisation of a-68 Iceberg. *Remote Sensing*, v. 13, 2021.

MOHAMMAD-DJAFARI, A. Entropy, Information Theory, Information Geometry and Bayesian Inference in Data, Signal and Image Processing and Inverse Problems. *Entropy*, v. 17, n. 6, p. 3989–4027, 2015.

MONDINI, A. C. et al. Landslide Failures Detection and Mapping Using Synthetic Aperture Radar: Past, Present and Future. *Earth-Science Reviews*, v. 216, p. 103574, 2021.

MOREIRA, A. et al. A Tutorial on Synthetic Aperture Radar. *IEEE Geoscience and Remote Sensing Magazine*, v. 1, n. 1, p. 6–43, 2013.

NASCIMENTO, A. D. C. et al. Comparing Edge Detection Methods Based on Stochastic Entropies and Distances for PolSAR Imagery. *IEEE Journal of Selected Topics in Applied Earth Observations and Remote Sensing*, v. 7, n. 2, p. 648–663, 2014.

NASCIMENTO, A. D. C.; CINTRA, R. J.; FRERY, A. C. Hypothesis Testing in Speckled Data with Stochastic Distances. *IEEE Transactions on Geoscience and Remote Sensing*, v. 48, n. 1, p. 373–385, 2010.

NASCIMENTO, A. D. C.; FRERY, A. C.; CINTRA, R. J. Detecting Changes in Fully Polarimetric SAR Imagery with Statistical Information Theory. *IEEE Transactions on Geoscience and Remote Sensing*, v. 57, n. 3, p. 1380–1392, 2019.

NETO, J. F. S. R.; RODRIGUES, F. A. A. Improving Log-Cumulant-Based Estimation of Heterogeneity Information in SAR Imagery. *IEEE Geoscience and Remote Sensing Letters*, v. 20, p. 1–5, 2023.

NOBRE, R. H. et al. SAR Image Segmentation with Rényi's Entropy. *IEEE Signal Processing Letters*, v. 23, n. 11, p. 1551–1555, 2016.

NOUGHABI, A.; ARGHAMI, N. A New Estimator of Entropy. *Journal of the Iranian Statistical Society*, v. 9, n. 1, p. 53–64, 2010.

PACHTER, J. A.; YANG, Y.-J.; DILL, K. A. Entropy, Irreversibility and Inference at the Foundations of Statistical Physics. *Nature Reviews Physics*, v. 6, n. 6, p. 382–393, 2024.

PARIKH, H.; PATEL, S.; PATEL, V. Classification of SAR and PolSAR Images Using Deep Learning: A Review. *International Journal of Image and Data Fusion*, v. 11, n. 1, p. 1–32, 2019.

PARK, J.-M.; SONG, W. J.; PEARLMAN, W. A. Speckle Filtering of SAR Images Based on Adaptive Windowing. *IEE Proceedings – Vision, Image, and Signal Processing*, v. 146, n. 4, p. 191, 1999.

PRESSÉ, S. et al. Principles of Maximum Entropy and Maximum Caliber in Statistical Physics. *Reviews of Modern Physics*, v. 85, n. 3, p. 1115–1141, 2013.

RATHA, D. et al. Novel Techniques for Built-up Area Extraction from Polarimetric SAR Images. *IEEE Geoscience and Remote Sensing Letters*, v. 17, n. 1, p. 177–181, 2020.

RÉNYI, A. On measures of entropy and information. In: Proceedings of the fourth Berkeley Symposium on Mathematical Statistics and Probability, University of California Press, 1961.

SEPÚLVEDA-FONTAINE, S. A.; AMIGÓ, J. M. Applications of Entropy in Data Analysis and Machine Learning: A Review. *Entropy*, v. 26, n. 12, p. 1126, 2024.

SHANNON, C. E. A Mathematical Theory of Communication. *The Bell System Technical Journal*, v. 27, n. 3, p. 379–423, 1948.

TSALLIS, C. Possible Generalization of Boltzmann-Gibbs Statistics. *Journal of Statistical Physics*, v. 52, n. 1–2, p. 479–487, 1988.

VAN ES, B. Estimating Functionals Related to a Density by a Class of Statistics Based on Spacings. *Scandinavian Journal of Statistics*, v. 19, p. 61–72, 1992.

VASCONCELLOS, K. L. P.; FRERY, A. C.; SILVA, L. B. Improving Estimation in Speckled Imagery. *Computational Statistics*, v. 20, n. 3, p. 503–519, 2005.

VASICEK, O. A Test for Normality Based on Sample Entropy. *Journal of the Royal Statistical Society Series B: Statistical Methodology*, v. 38, n. 1, p. 54–59, 1976.

WIECZORKOWSKI, R.; GRZEGORZEWSKI, P. Entropy Estimators-Improvements and Comparisons. *Communications in Statistics-Simulation and Computation*, v. 28, n. 2, p. 541–567, 1999.

YUE, D.-X. et al. Synthetic Aperture Radar Image Statistical Modeling: Part One-Single-Pixel Statistical Models. *IEEE Geoscience and Remote Sensing Magazine*, v. 9, n. 1, p. 82–114, 2021.

APPENDIX A – LIMIT BEHAVIOR OF ENTROPY FUNCTIONS

LIMIT BEHAVIOR OF $H\left(\mathcal{G}_I^0\right)$ AS $\alpha \to -\infty$

To verify that $H\left(\mathcal{G}_I^0(\alpha,\mu,L)\right)$ converges to $H\left(\Gamma_{\mathsf{SAR}}(\mu,L)\right)$ as $\alpha \to -\infty$, we show that the additional terms in $H\left(\mathcal{G}_I^0\right)$ cancel in the limit.

The Shannon entropy for the $\mathcal{G}_I^0$ distribution is given by:

$$H\left(\mathcal{G}_I^0(\alpha,\mu,L)\right) = H(\Gamma_{\mathsf{SAR}}) + \Big[(L-\alpha)\psi^{(0)}(L-\alpha) - (1-\alpha)\psi^{(0)}(-\alpha) + \ln(-1-\alpha) - \ln\Gamma(L-\alpha) + \ln\Gamma(-\alpha) - L\Big]. \quad (5.1)$$

We aim to show that

$$\lim_{\alpha\to-\infty} H\left(\mathcal{G}_I^0(\alpha,\mu,L)\right) = H\left(\Gamma_{\mathsf{SAR}}(\mu,L)\right).$$

The additional terms in $H\left(\mathcal{G}_I^0\right)$ compared to $H\left(\Gamma_{\mathsf{SAR}}\right)$ are:

$$\lim_{\alpha\to-\infty} \Big[(L-\alpha)\psi^{(0)}(L-\alpha) - (1-\alpha)\psi^{(0)}(-\alpha) + \ln(-1-\alpha) - \ln\Gamma(L-\alpha) + \ln\Gamma(-\alpha)\Big] - L. \quad (5.2)$$

For $L = 1$, this becomes:

$$\lim_{\alpha\to-\infty} \Bigg[\underbrace{-\ln\Gamma(1-\alpha) + \ln(-1-\alpha) + \ln\Gamma(-\alpha)}_{A} + \underbrace{(1-\alpha)\psi^{(0)}(1-\alpha) - (1-\alpha)\psi^{(0)}(-\alpha)}_{B}\Bigg] - 1. \quad (5.3)$$

Simplifying A and B:

$$A = \ln\frac{(-1-\alpha)\Gamma(-\alpha)}{\Gamma(1-\alpha)} = \ln\frac{(-1-\alpha)\Gamma(-\alpha)}{-\alpha\Gamma(-\alpha)} = \ln\frac{-1-\alpha}{-\alpha} = \ln\left(1+\frac{1}{\alpha}\right).$$

$$
\begin{aligned}
B &= (1-\alpha)\left[\psi^{(0)}(1-\alpha) - \psi^{(0)}(-\alpha)\right] \\
&= (1-\alpha)\left[\psi^{(0)}\underbrace{(1-\alpha-1) + \frac{1}{1-\alpha-1}}_{\text{Because } \psi^{(0)}(x+1)=\psi^{(0)}(x)+\frac{1}{x}} - \psi^{(0)}(-\alpha)\right] \\
&= (1-\alpha)\left[\psi^{(0)}(-\alpha) - \frac{1}{\alpha} - \psi^{(0)}(-\alpha)\right] = -\frac{1}{\alpha} + 1.
\end{aligned}
$$

Replacing A and B into (5.3) and taking the limit, we obtain:

$$
\underbrace{\lim_{\alpha\to-\infty} \ln\left(1+\frac{1}{\alpha}\right)}_{\text{approaches } 0} - \underbrace{\lim_{\alpha\to-\infty} \frac{1}{\alpha}}_{\text{approaches } 0} + \lim_{\alpha\to-\infty} 1 - 1 = 0.
$$

For the general case $L > 1$, we use Stirling's approximation for large z:

$$
\Gamma(z) \sim \sqrt{2\pi z}\left(\frac{z}{e}\right)^z,
$$

and

$$
\psi^{(0)}(z) \sim \ln(z) - \frac{1}{2z}.
$$

Therefore, the terms of Equation (5.2) approximate to:

$$
\begin{aligned}
-\ln\Gamma(L-\alpha) &\sim -\frac{1}{2}\ln\left(2\pi(L-\alpha)\right) - (L-\alpha)\ln(L-\alpha) + (L-\alpha), \\
(L-\alpha)\psi^{(0)}(L-\alpha) &\sim (L-\alpha)\ln(L-\alpha) - \frac{1}{2}, \\
-(1-\alpha)\psi^{(0)}(-\alpha) &\sim -(1-\alpha)\ln(-\alpha) - \frac{1-\alpha}{2\alpha}, \\
\ln\Gamma(-\alpha) &\sim \frac{1}{2}\ln(-2\pi\alpha) - \alpha\ln(-\alpha) + \alpha.
\end{aligned}
$$

Then, replacing these in (5.2), we get:

$$
\begin{aligned}
\lim_{\alpha\to-\infty}\Bigg[&-\frac{1}{2}\ln\left(2\pi(L-\alpha)\right) - L\ln(L-\alpha) + \alpha\ln(L-\alpha) + L - \alpha \\
&+ L\ln(L-\alpha) - \alpha\ln(L-\alpha) - \frac{1}{2} - \ln(-\alpha) + \alpha\ln(-\alpha) - \frac{1-\alpha}{2\alpha} \\
&+ \ln(-1-\alpha) + \frac{1}{2}\ln(-2\pi\alpha) - \alpha\ln(-\alpha) + \alpha\Bigg] - L.
\end{aligned}
$$

We then simplify:

$$\lim_{\alpha\to-\infty}\left[-\frac{1}{2}\ln(2\pi(L-\alpha))+L-\frac{1}{2}-\ln(-\alpha)-\frac{1-\alpha}{2\alpha}+\ln(-(1+\alpha))+\frac{1}{2}\ln(-2\pi\alpha)\right]-L.$$

Group terms:

$$\lim_{\alpha\to-\infty}\left[\frac{1}{2}\ln\frac{-\alpha}{L-\alpha}+L-\frac{1}{2}+\frac{\alpha-1}{2\alpha}+\ln\frac{1+\alpha}{\alpha}\right]-L=\frac{1}{2}\ln 1+L-\frac{1}{2}+\frac{1}{2}+\ln 1-L=0.$$

Therefore,

$$\lim_{\alpha\to-\infty}H\Big(\mathcal{G}_I^0(\alpha,\mu,L)\Big)=H\Big(\Gamma_{\mathsf{SAR}}(\mu,L)\Big).$$

which concludes the proof.

LIMIT BEHAVIOR OF $R_\lambda(\mathcal{G}_I^0)$ AS $\alpha\to-\infty$

We want to show that

$$\lim_{\alpha\to-\infty}R_\lambda\Big(\mathcal{G}_I^0\Big)(\alpha,\mu,L)=R_\lambda\Big(\Gamma_{\mathrm{SAR}}\Big)(\mu,L).$$

We can express (2.14) as follows:

$$\begin{aligned}R_\lambda\Big(\mathcal{G}_I^0\Big)(\mu,\alpha,L)=R_\lambda\Big(\Gamma_{\mathrm{SAR}}\Big)(\mu,L)\ &+\ \ln\Big(-1-\alpha\Big)\\&+\frac{1}{1-\lambda}\ln\left[\frac{\Gamma(L-\alpha)^\lambda\,\Gamma\Big(\lambda(-\alpha+1)-1\Big)\,\lambda^{\lambda(L-1)+1}}{\Gamma(-\alpha)^\lambda\,\Gamma\Big(\lambda(L-\alpha)\Big)}\right].\end{aligned}$$

Set

$$\Delta_\alpha=R_\lambda\Big(\mathcal{G}_I^0\Big)(\mu,\alpha,L)-R_\lambda\Big(\Gamma_{\mathrm{SAR}}\Big)(\mu,L).$$

Then

$$\Delta_\alpha=\ln(-1-\alpha)+\frac{1}{1-\lambda}\ln\left[\frac{\Gamma(L-\alpha)^\lambda\,\Gamma\Big(\lambda(-\alpha+1)-1\Big)\,\lambda^{\lambda(L-1)+1}}{\Gamma(-\alpha)^\lambda\,\Gamma\Big(\lambda(L-\alpha)\Big)}\right]. \tag{5.4}$$

As $\alpha \to -\infty$, we have $-1-\alpha \approx |\alpha|$, so

$$\ln(-1-\alpha) \sim \ln|\alpha|.$$

Note that for large $|\alpha|$, we can the asymptotic relation $\Gamma(x+a)/\Gamma(x+b) \sim x^{a-b}$. Specifically:

$$\Gamma(L-\alpha)/\Gamma(-\alpha) \;\sim\; |\alpha|^L, \quad \Gamma\Big(\lambda(-\alpha+1)-1\Big)/\Gamma\Big(\lambda(L-\alpha)\Big) \;\sim\; \Big(\lambda|\alpha|\Big)^{(\lambda-1)-\lambda L}.$$

Thus, inside the logarithm in (5.4),

$$\frac{\Gamma(L-\alpha)^\lambda\,\Gamma\Big(\lambda(-\alpha+1)-1\Big)}{\Gamma(-\alpha)^\lambda\,\Gamma\Big(\lambda(L-\alpha)\Big)} \;\sim\; |\alpha|^{\lambda L} \times |\alpha|^{(\lambda-1)-\lambda L} = |\alpha|^{\,\lambda-1}.$$

Since $\lambda^{\lambda(L-1)+1}$ does not depend on α, multiplying by this constant factor does not alter the asymptotic behavior in α. Therefore,

$$\frac{1}{1-\lambda}\,\ln\Big[\dots\Big] \;\sim\; \frac{1}{1-\lambda}\,\ln\Big(|\alpha|^{\,\lambda-1}\Big) = \frac{\lambda-1}{1-\lambda}\,\ln|\alpha| = -\ln|\alpha|.$$

Hence

$$\Delta_\alpha \;\sim\; \ln|\alpha| - \ln|\alpha| = 0 \quad \text{as}\, \alpha \to -\infty.$$

This shows $\Delta(\alpha) \to 0$, and consequently

$$\lim_{\alpha\to-\infty} R_\lambda\Big(\mathcal{G}_I^0\Big)(\mu,\alpha,L) = R_\lambda\Big(\Gamma_{\mathrm{SAR}}\Big)(\mu,L).$$

LIMIT BEHAVIOR OF $T_\lambda(\mathcal{G}_I^0)$ AS $\alpha \to -\infty$

We want to show that

$$\lim_{\alpha\to-\infty} T_\lambda\Big(\mathcal{G}_I^0\Big)(\alpha,\mu,L) = T_\lambda\Big(\Gamma_{\mathrm{SAR}}\Big)(\mu,L).$$

Write the Tsallis entropy of $\mathcal{G}_I^0$ in the compact form

$$T_\lambda\Big(\mathcal{G}_I^0(\mu,\alpha,L)\Big) = T_\lambda\Big(\Gamma_{\mathrm{SAR}}(\mu,L)\Big) + \Delta_\alpha^T, \qquad \Delta_\alpha^T = \frac{C}{\lambda-1}\Big(1-e^{\Phi_\alpha}\Big),$$

with the constant (independent of α)

$$C = \exp\Big[(1-\lambda)\ln\mu + (\lambda-1)\ln L + \ln\Gamma\Big(\lambda(L-1)+1\Big) - \lambda\ln\Gamma(L)\Big]$$

and

$$\Phi_\alpha = (1-\lambda)\ln(-\alpha-1) + \lambda\ln\frac{\Gamma(L-\alpha)}{\Gamma(-\alpha)} + \ln\frac{\Gamma\Big(\lambda(1-\alpha)-1\Big)}{\Gamma\Big(\lambda(L-\alpha)\Big)}.$$

If $\Phi_\alpha \to 0$ as $\alpha \to -\infty$, then $\exp[\Phi_\alpha] \to 1$ and, therefore, $\Delta_\alpha^T \to 0$. Hence the goal reduces to showing $\Phi_\alpha \to 0$.

For large $|x|$ and fixed c, $\dfrac{\Gamma(x+c)}{\Gamma(x)} \sim x^c$.

Set $A := -\alpha$ (> 0); then $\alpha \to -\infty$ means $A \to \infty$. Applying the rule we have

$$\frac{\Gamma(L+A)}{\Gamma(A)} \sim A^L, \qquad \frac{\Gamma(\lambda A+\lambda-1)}{\Gamma(\lambda A+\lambda L)} \sim (\lambda A)^{(\lambda-1)-\lambda L}.$$

Using $\ln x^c = c\ln x$ and $\ln(\lambda A) = \ln\lambda + \ln A$,

$$\Phi_\alpha \sim (1-\lambda)\ln A + \lambda L\ln A + \Big[\lambda(1-L)-1\Big]\Big(\ln\lambda + \ln A\Big).$$

The coefficient of $\ln A$ is

$$(1-\lambda) + \lambda L + \lambda(1-L) - 1 \;=\; 0.$$

so every logarithm in A disappears.

The remaining constant is $\Big[\lambda - 1 - \lambda L\Big]\ln\lambda$. But $\lambda - 1 - \lambda L = -\Big[\lambda(L-1)+1\Big]$, and the opposite factor $\lambda(L-1)+1$ already appears with the opposite sign inside C; therefore this constant term vanishes as well. Consequently $\Phi_\alpha \to 0$ and thus $\Delta_\alpha^T \longrightarrow 0$.

APPENDIX B – DERIVATIONS OF SPACING ESTIMATORS

This appendix mirrors the derivation given for Vasicek's estimator of Shannon entropy, and the Tsallis estimator.

FROM QUANTILE FUNCTION TO VASICEK ESTIMATOR

The differential entropy of a continuous random variable Z with density $f(z)$ is given by:

$$H(Z) = -\int_{-\infty}^{\infty} f(z) \ln f(z) \, \mathrm{d}z.$$

We now perform a change of variables using the cdf of $F(z)$ and its inverse, the quantile function $Q(p) = F^{-1}(p)$.

- Let $p = F(z)$ so that $z = Q(p)$.
- Then, using the change of variables:

$$\mathrm{d}z = Q'(p) \, \mathrm{d}p, \quad \text{and} \quad f(z) = F'(z) = \frac{1}{Q'(p)}.$$

Substituting into the integral:

$$\begin{aligned} H(Z) &= -\int_{-\infty}^{\infty} f(z) \ln f(z) \, \mathrm{d}z \\ &= -\int_{0}^{1} f(Q(p)) \ln f(Q(p)) \cdot Q'(p) \, \mathrm{d}p \\ &= -\int_{0}^{1} \ln f(Q(p)) \, \mathrm{d}p. \end{aligned}$$

Now, since $f(Q(p)) = \frac{1}{Q'(p)}$, we get:

$$\ln f(Q(p)) = -\ln Q'(p),$$

thus,

$$H(Z) = \int_{0}^{1} \ln Q'(p) \, \mathrm{d}p.$$

Entropy can be expressed without needing the explicit density $f(z)$. It is sufficient to integrate the logarithm of the derivative of the quantile function over $p \in (0, 1)$.

In practice, the quantile function Q is unknown, but we have access to a sample $\{Z_1, \ldots, Z_n\}$, whose ordered values are:

$$Z_{(1)} \leq Z_{(2)} \leq \cdots \leq Z_{(n)}.$$

Each order statistic $Z_{(i)}$ serves as an empirical quantile:

$$Z_{(i)} \approx Q\left(\frac{i}{n+1}\right).$$

To approximate $Q'(p)$ at $p_i \approx \frac{i}{n+1}$, we use a symmetric finite difference:

$$\begin{aligned} Q'(p_i) &\approx \frac{Q(p_{i+m}) - Q(p_{i-m})}{p_{i+m} - p_{i-m}} \\ &= \frac{Z_{(i+m)} - Z_{(i-m)}}{\frac{i+m}{n+1} - \frac{i-m}{n+1}} \\ &= \frac{n+1}{2m}(Z_{(i+m)} - Z_{(i-m)}). \end{aligned}$$

This is a symmetric window of width $2m$, valid for $m < i < n - m$.

The integral over $p \in [0, 1]$ is approximated by a Riemann sum:

$$\int_0^1 \ln Q'(p)\,\mathrm{d}p \approx \frac{1}{n}\sum_{i=1}^{n} \ln Q'(p_i).$$

Substituting the approximation of $Q'(p_i)$:

$$\widehat{H}_{\mathsf{V}}(\boldsymbol{Z}) = \frac{1}{n}\sum_{i=1}^{n} \ln\left[\frac{n+1}{2m}\left(Z_{(i+m)} - Z_{(i-m)}\right)\right].$$

This is the Vasicek estimator of Shannon entropy.

TSALLIS ENTROPY AND THE QUANTILE FUNCTION

For a continuous random variable Z with pdf f and cdf F, the Tsallis entropy is defined by:

$$T_\lambda(Z) \;=\; \frac{1}{\lambda - 1}\Big(1 - \mathbb{E}\big[f^{\,\lambda-1}(Z)\big]\Big) \;=\; \frac{1}{\lambda - 1}\Big(1 - \int_{\mathbb{R}} f^{\lambda}(z)\,\mathrm{d}z\Big). \tag{5.5}$$

To express T_λ in terms of the quantile function $Q(p) = F^{-1}(p)$ for $p \in (0,1)$, note that $F\big(Q(p)\big) = p$. Differentiating with respect to p yields:

$$f\big(Q(p)\big)\, Q'(p) = 1 \quad \Longrightarrow \quad Q'(p) = \frac{1}{f\big(Q(p)\big)}. \tag{5.6}$$

Using the change of variables $z = Q(p)$ ($\mathrm{d}z = Q'(p)\,\mathrm{d}p$) in the integral of (5.5) and applying (5.6),

$$\mathbb{E}\big[f^{\,\lambda-1}(Z)\big] \;=\; \int_0^1 \big[f(Q(p))\big]^{\lambda-1}\,\mathrm{d}p \;=\; \int_0^1 \big[Q'(p)\big]^{1-\lambda}\,\mathrm{d}p.$$

Hence the entropy can be written solely in terms of the quantile derivative:

$$T_\lambda(Z) \;=\; \frac{1}{\lambda-1}\Big\{1 - \int_0^1 \big[Q'(p)\big]^{1-\lambda}\,\mathrm{d}p\Big\}. \tag{5.7}$$

Equation (5.7) dispenses with the pdf itself; once we can estimate $Q'(p)$, we obtain an estimator of T_λ.

Draw an i.i.d. sample $Z_1, \ldots, Z_n \sim F$ and sort it, $Z_{(1)} \le \cdots \le Z_{(n)}$. Fix an integer window $m \in \{1, \ldots, \lfloor n/2 \rfloor\}$. For every index $i = 1, \ldots, n$ define the (centred) m–spacing:

$$D_{i,m} \;=\; Z_{(i+m)} - Z_{(i-m)},$$

with the conventions $Z_{(i-m)} := Z_{(1)}$ when $i \le m$ and $Z_{(i+m)} := Z_{(n)}$ when $i \ge n-m$.

Because $Z_{(i)} \approx Q\big(i/n\big)$, the points $Z_{(i-m)}$ and $Z_{(i+m)}$ correspond roughly to the probabilities $(i-m)/n$ and $(i+m)/n$, so that, $\Delta p = 2m/n$. A centred finite–difference therefore gives the quantile-slope estimator:

$$\widehat{Q'}\big(p_i\big) \;=\; \frac{Z_{(i+m)} - Z_{(i-m)}}{\dfrac{2m}{n}} = \frac{n}{2m}\, D_{i,m}, \qquad p_i := \frac{i}{n}. \tag{5.8}$$

To reduce edge bias Ebrahimi et al. (1994) suggest position-dependent correction factors

$$c_i = \begin{cases} 1 + \dfrac{i-1}{m}, & 1 \le i \le m, \\ 2, & m+1 \le i \le n-m, \\ 1 + \dfrac{n-i}{m}, & n-m+1 \le i \le n. \end{cases}$$

The resulting boundary-corrected m-spacing density estimator is

$$\widehat{f}_n\big(Z_{(i)}\big) \;=\; \frac{c_i\, m/n}{D_{i,m}}, \qquad i = 1, \ldots, n.$$

By construction $\widehat{f}_n\big(Z_{(i)}\big) \approx f\big(Z_{(i)}\big)$, while its reciprocal gives an improved estimate of $Q'(p_i)$:

$$\widehat{Q'}\big(p_i\big) \;=\; \frac{1}{\widehat{f}_n\big(Z_{(i)}\big)} \;=\; \frac{D_{i,m}}{c_i\, m/n}. \tag{5.9}$$

Approximating the integral in (5.7) by the Riemann sum over the grid $p_i = i/n$ and inserting $\widehat{Q'}\big(p_i\big)$ of (5.9) yields the non-parametric Tsallis entropy estimator:

$$\widehat{T}_\lambda(\boldsymbol{Z}) \;=\; \frac{1}{\lambda - 1}\left\{1 - \frac{1}{n}\sum_{i=1}^{n}\Big[\widehat{Q'}\big(p_i\big)\Big]^{1-\lambda}\right\} \;=\; \frac{1}{\lambda - 1}\left\{1 - \frac{1}{n}\sum_{i=1}^{n}\Big(\frac{c_i\, m/n}{D_{i,m}}\Big)^{\lambda-1}\right\}. \tag{5.10}$$